ANALYSIS OF ENHANCED MIXING BY NATURAL AND FORCED CONVECTION WITH APPLICATION TO CHEMICAL REACTOR DESIGN

Clara Tatiana González Hidalgo

Dipòsit Legal: T.1422-2013

Clara Tatiana González Hidalgo

ANALYSIS OF ENHANCED MIXING BY NATURAL AND FORCED CONVECTION WITH APPLICATION TO CHEMICAL REACTOR DESIGN

DOCTORAL THESIS

supervised by Dr. Joan Herrero

cosupervised by Dr. Dolors Puigjaner

Departament d' Enginyeria Química

UNIVERSITAT ROVIRA I VIRGILI

Tarragona

2013

Joan Herrero, professor titular del Departament d' Enginyeria Química i Dolors Puigjaner, professora titular del Departament d' Enginyeria Informàtica i Matemàtiques, de la Universitat Rovira i Virgili,

CERTIFIQUEN:

Que el present treball titulat: "Analysis of Enhanced Mixing by Natural and Forced Convection with Application to Chemical Reactor Design", que presenta Clara Tatiana González Hidalgo per a l'obtenció del títol de Doctor, ha estat realitzat sota la nostra direcció en el Departament d'Enginyeria Química d'aquesta Universitat.

Tarragona, 25 de juny de 2013

Joan Herrero Dolors Puigjaner

UNIVERSITAT ROVIRA I VIRGILI
ANALYSIS OF ENHANCED MIXING BY NATURAL AND FORCED CONVECTION WITH APPLICATION TO CHEMICAL REACTOR DESIGN
Clara Tatiana González Hidalgo
Dipòsit Legal: T.1422-2013

Dedicada a Gus
mi compañero
de lucha y de vida.

UNIVERSITAT ROVIRA I VIRGILI
ANALYSIS OF ENHANCED MIXING BY NATURAL AND FORCED CONVECTION WITH APPLICATION TO CHEMICAL REACTOR DESIGN
Clara Tatiana González Hidalgo
Dipòsit Legal: T.1422-2013

Agradecimientos

En primer lugar quiero agradecer a mi supervisor de tesis, el profesor Joan Herrero. Su amabilidad desde el inicio y su disponibilidad total para resolver mis dudas y guiarme para tomar el camino correcto en cada etapa del desarrollo del trabajo fueron imprescindibles. Me siento totalmente afortunada de haber tenido un supervisor tan dedicado y tan pendiente del trabajo que se encontraba bajo su dirección. Agradezco también la enorme cordialidad de mi co–supervisora, la profesora Dolors Puigjaner, su ayuda, su dirección y sus correcciones siempre tan oportunas. Gracias a la amabilidad y a la incondicional ayuda de estas dos personas y al buen ambiente de trabajo que encontré en nuestro grupo de investigación DSfluids, este trabajo llegó a buen término siendo satisfactorio y gratificante.

A Gus, gracias por la invitación a emprender este camino juntos, tanto académico como personal, por su compañía, por su apoyo que va más allá de las meras palabras, por sus ánimos, por creer en mí y por su ejemplo. Por compartir esta etapa tan inolvidable de nuestras vidas y por seguir compartiendo juntos y por llenar mi vida.

Quiero agradecer también a mis padres, Gerardo y Clarita, porque gracias al amor y a la educación que ellos me brindaron es que tuve la oportunidad de llegar aquí. Por supuesto que sin ellos, esto hubiera sido imposible. Gracias a sus constantes ánimos y oraciones y a su apoyo incondicional.

Gracias a mis hermanos Marce y David y también a Sergio y a Marisol, por quienes también he llegado a este lugar, por su cariño, por estar siempre pendientes de mí y por alegrarse con mis alegrías, sin sus ánimos y sus conversaciones este hubiera sido un camino mucho más difícil de recorrer. Gracias a los dibujos de Jero y sus charlas que siempre me alentaron tanto y a Jacobo quien con solo saber que viene en camino me llena de felicidad.

Gracias a mis amigos Carlos y Shirley, nuestra familia y nuestros ángeles de la guarda en Tarragona. Su alegría nos hizo siempre ver todo más bello en esta ciudad y aprender a conocerla y disfrutarla al máximo. Su incondicional ayuda en todo momento nos alivió muchas cargas que no tenemos forma de corresponder y que valen mucho más de lo que ellos se imaginan.

Gracias a Ana, quien desde el inicio de este proceso estuvo ahí y quien a pesar de la distancia y el tiempo, sigo importándole y sigue estando allí para oirme, darme fuerzas y ayudarme a ver las cosas de la mejor manera.

Gracias al apoyo financieron recibido del proyecto DGIC CTQ2008-04857/PPQ y del CIRIT “Programa de Groups de Recerca Consolidats de la Generalitat de Catalunya” (2009SGR-1529).

Publications

- C.T. Gonzalez-Hidalgo, J. Herrero, D. Puigjaner, "Mixing intensification by natural convection with application to a chemical reactor design", *Chem. Eng. J.* **200**, p 506–520, 2012.
- C.T. Gonzalez-Hidalgo, J. Herrero, D. Puigjaner, "Enhancement of mixing in a catalytic chemical reactor consisting of a stack of corotating disks in a cylindrical enclosure", *Submitted*.

Contents

1 Introduction **1**

2 Problem formulation **7**
2.1 Forced convection problem 7
2.1.1 Fluid mechanics model 7
2.1.2 Mass transfer model 9
2.2 Natural convection problem 10

3 Numerical method **15**
3.1 Forced convection problem 17
3.1.1 Velocity field 17
3.1.2 Concentration field 18
3.2 Natural convection problem 20
3.2.1 Concentration field 21
3.2.2 Dynamical Analysis 22
3.3 Accuracy assessment 23
3.3.1 One–dimensional limit 23
3.3.2 Forced convection problem 26
3.3.3 Natural convection problem 29

4 Results and Discussion **31**
4.1 Efficiency Assessment 31
4.2 Forced convection problem 34
4.2.1 Velocity Field 34
4.2.2 Discontinuous operation 37
4.2.3 Semicontinuous operation 47
4.3 Natural convection problem 51
4.3.1 Natural convection flow 51
4.3.2 Concentration field 57
4.3.3 Scaling Analysis 58

5 Conclusions **69**

Appendices **72**

A Discretization procedure of the forced convection problem **73**

B Discretization procedure of the natural convection problem **77**

Chapter 1

Introduction

Process intensification, understood as a significant reduction in the size of process units and the enhancement of their versatility and efficiency is one of the main chemical engineering purposes. This increment of efficiency must arise as a consequence of novel designs of process equipment that adapt dynamically the mixing in its interior to each kind of application regarding the demand of heat or mass transfer.

Chemical and environmental engineering, biotechnology, and pharmaceutical industries widely use process catalysts. The chemical reactions that occur in such processes take place on catalyst surfaces or pellets. Examples of important processes where catalytic reactions are involved are the isomerization of glucose and fructose to produce fructose rich syrups [1], lactose hydrolysis to produce commercial infant milk formulas or low lactose milk products [2], cellulose produced by bacteria to use in medicine and cosmetics [3], or hydroformylation of olefins to aldehydes to manufacture products such as detergents, surfactants or plasticizers [4], among many different kind of reactions and applications.

Immobilized catalysts have been preferred over dissolved or suspended ones in stirred reactors since immobilization facilitates catalyst reutilization and avoids catalyst recovery and purification processes [5, 6]. In a typical reactor fluid system, when immobilized catalysts are attached to an impermeable solid support, molecules are convected from the bulk of fluids into the vicinity of the catalyst surface and then transported to the catalyst active sites by molecular diffusion. This is the reason why mixing is a very important issue in many applications since the substrate has to be brought into contact with the active sites of catalysts. In many cases, mass transfer resistances are strongly dependent on substrate diffusivity, porosity of catalyst carrier and reactor hydrodynamic conditions.

Traditionally, stirred tank reactors have been used since they favour a good distribution of substrate over the catalyst and it is possible to attain homogeneous conditions over, for instance, the cell cultures in bioreactions, by regulating the degree of agitation. When mixing is provided by an impeller, convection can be very fast and the process is then controlled either by the rate of molecular diffusion or by the rate of reaction. Different authors, have analyzed the influence of the mass transfer resistance on the efficiency of different kind of chemical reactors. For example, Justen et al. [7], studied the dependence of *penicillium chrysogenum* growth and productivity in fed-batch fermentations (to produce penicillin) on impeller type and agitation intensity. They found that for a given impeller the growth rates and the overall biomass concentrations increased with agitation intensity, establishing that higher agitation intensities appeared to cause more fragmentation which could have led to increased formation of new growing tips. They also suggested that the total power input and the choice of

impeller geometry determine the mechanical forces that might affect microorganisms in a fermentor, thereby influencing growth or production. Sánchez Pérez et al. [8] analyzed the shear rate in a stirred tank reactor motivated by the fact that microorganisms and other suspended solids are susceptible to damage depending on the prevailing shear rate, which they show is a function of the rotational speed of the impeller. Han et al. [9], performed the numerical simulation on micromixing of viscous fluids in a stirred tank reactor. They found better micromixing is achieved with a fluid of lower viscosity and a higher agitation speed, as a result the formation of side products is disfavored and the reaction rates are accelerated.

Thus, when impellers are used, it may be attained high levels of shear in the vicinity of the impeller blades. This may cause for example cell damages and changes in their morphological state, which would decrease reaction yield in a given reactor. Accordingly, there is the need to find equipment which does not use any kind of stirrers, without hindering efficiency. Given that it is crucial to search for alternatives to traditional agitated systems, the aim of this work is the design of flow systems that improve mixing considering elimination of any mechanical mixing accessories. We focus our investigation in the device of highly efficient and compact configurations for heterogeneous chemical reactors, in particular, in reactors that have an immobilized catalyst in a solid surface and that follows a first order kinetic law. We study the mixing enhancement in these reactors via forced convection, by means of a pair of corotating disks enclosed by a cylindrical cavity, and natural convection, by means of a cubical cavity where convection is imposed by a difference of temperatures between the top and bottom wall.

Forced convection flow may cause an efficiency increment facilitating the transport of the reactant (product), towards (from) the catalytic surface. It is worth to spotlight some works [10–13] that make use of this. Yu et al. [10] studied the effect of vortex breakdown on the fluid environment for cell growth via an homogeneous reaction. They made a numerical study of fluid flow and oxygen transfer in a cylindrical bioreactor whose rotating base wall is used to generate the medium flow and mixing. Zeng et al. [11], simulated the fluid flow and mass transfer in a rectangular microchannel bioreactor with a monolayer of cells adherent to the bottom. The species of interest transfer from the inlet to the cell surface at the bottom of the channel, with a uniform inlet flow velocity, by a convective-diffusive mechanism. Al-Shannag et al. [12] proposed and analyzed an immobilized enzyme reactor, a cavity of square cross section where mixing is provided by the sliding top lid. This bioreaction system, led to low mechanical stresses compared to traditional stirred tank reactors. The highest velocities and velocity gradients occur near the top wall which is free of enzymes while biocells are attached at the bottom wall where shear is small. More recently, Al-Shannag [13] showed a similar setup in a toroidally-shaped cavity of square cross section. The stability of these kind of flows had been previously studied for cartesian and cylindrical geometry [14,15].

Rotation has also been used as a forced convection generator. Examples of this are the rotating packed beds (RPB) which are very much used nowadays in several applications. For example, Cheng et al. [16] studied experimentally separation processes for the capture of carbon dioxide from a gas by chemical absorption with aqueous solutions containing alkanolamines in a RPB. They found CO_2 capture efficiency increased with increasing temperature and was dependent on rotation speed, gas and liquid flow rates. Sung et al. [17], studied a RPB equipped with blade packings and baffles with potential application to transfer of volatile organic compounds, from gas to liquid. Using an isopropyl alcohol absorption process, they determined their model enhanced the mass transfer coefficient value, which was mainly attributed to the increase in slip angular velocity of the gas and improved liquid

mixing, dispersion and distribution in the rotor by static baffles. Hsu et al. [18] discussed the absorption performance of a rotating packed bed with blade packings in removing methanol and 1-butanol from binary mixtures finding that the rotating packed bed would be an excellent absorber for the removal of alkanols from gas streams.

A very classical system to enable and enhance mass transfer is the one of a single rotating disk. Peev et al. and Peshev et al. [19, 20], studied theoretically and experimentally the dissolution in liquid film flow on a horizontal rotating disk by means of dissolving gypsum in two aqueous solutions. Peshev et al. concluded that the speed of rotation is the most important operative parameter intensifying the dissolution rate in film flow of shear thinning liquid on a horizontal rotating disk. Tsibranska et al. [21] studied the oxygen desorption from two water polymer solutions. Numerical and experimental data demonstrate a synergetic effect of the increase of disk revolutions and decrease of liquid rheology index in intensifying the mass transfer process. Torras, et al. [22], studied numerically and experimentally the flow inside a flat membrane module with a smooth rotating disk. They suggested high permeate fluxes for the device due to large average shear stresses on the membrane and the absence of stagnant zones inside the module, which are desirable features to avoid membrane fouling processes.

Application of a single rotating disk to chemical reactors is as well found. Hardacre et al. [23], studied the selective heterogeneous catalytic reduction of phenyl acetylene to styrene over palladium supported on calcium carbonate, in a vertical rotating disk reactor (not all the disk is in contact with the liquid all the time). The reaction in the rotating disk reactor is dominated by reaction in the entrained film on the disk compared with very limited reaction in the bulk liquid. Belfiore [24], studied the dynamic shear in continuous flow rotating disk catalytic reactors. In his parallel disk reactor setup, the reactants chemisorb on the surface of the rotating plate (the other one remains immobile) and catalytic sites are replenished from the bulk fluid toward the active surface. Chemical reaction is enhanced by viscous shear at the interface between the bulk fluid and the rotating plate. The reaction/diffusion boundary condition on the surface of the rotating plate accounts for stress sensitive reactant consumption. Meeuwse et al. [25] proposed a setup that consists of a rotor-stator geometry which consists in a single rotating disk with a catalytic coating spinning inside a fixed cavity where the fluid flows. A fast chemical reaction (glucose oxidation) takes place in the catalytic medium which is located on the inferior disk surface. They found an unexpected result, the Sherwood number, scales as $Sh \propto Re^{2.02}$ ($10^5 \leqslant Re \leqslant 7 \times 10^5$) very different compared with the 0.5 and 0.9 which are the established values for laminar and turbulent flow respectively.

Instead of using a single rotating disk, our proposal is to use a stack of corotating enclosed disks as a mixing enhancer in a catalytic chemical reactor. To model it we use only two corotating disks since no interaction is considered between adjacent spaces. Several investigations on the flow between two corotatory disks has taken the scientific community attention [26–40] since it is a simple model that allows to understand the fluid dynamics basic features of the flow of air inside the computer hard disks. Figure 1.1 shows the most common geometry used in order to define the problem. As shown, it is made up of two disks of radius R_2 attached to a hub of radius R_1 that rotates at an angular velocity Ω. The disks are separated by a distance H and are confined in a cylindrical cavity which is at rest. The dimensionless parameters that rule the incompressible flow for this geometry are the Reynolds number, $Re = \Omega R_2^2/\nu$, where ν is the kinematic viscosity of the fluid; the aspect ratio, $S = H/R_2$ and the radii ratio, $\gamma = R_1/R_2$. Disks rotation produce a secondary flow in the transversal plane where the fluid is moving toward the exterior along the Ekman's

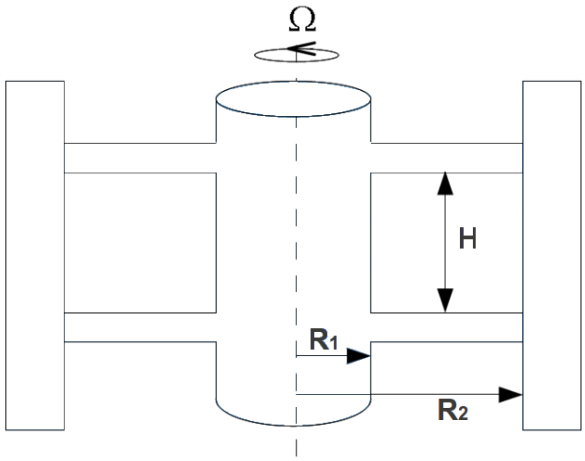

Figure 1.1: Sketch of the pair of corotating disks problem.

boundary layer close to the surface of each disk. At low Re numbers, the flow is axisymmetric, i.e., independent of the angular coordinate, and it is characterized by the presence of a couple of vortices in the transversal plane, similar to the ones that can be observed in the Taylor-Couette flow [26, 27, 29–31]. It is known that, for laminar flow the heat transfer velocities for the corotatory disks system are scaled in a similar way to the classical problem of one rotatory disk, $Nu \propto Re^{1/2}Pr^{1/3}$ [31, 36].

Considering the boundary layer flow type characteristic of the problem of the pair of corotatory disks, it is not surprising that several technological applications have been developed involving heat or mass transfer between the disk surface and the fluid not only of a pair but of a set of more than two disks. Engin et al. [41] studied a multiple–disk Tesla type fan. Sarkar et al. [42] proposed a rotating disk bioreactor which has several vertical corotating disks. Drumm et al. [42–44] studied numerically and validated experimentally liquid-liquid extraction in a rotating disk contactor type extraction column (several rotating disks act as stirrers in the column).

As previously mentioned, our first proposal as an alternative to traditional systems to enhance mixing and improve efficiency in a chemical reactor is the model of a pair of corotating disks enclosed by a cylindrical cavity. Then, the extension to more than two disks is made piling up several pairs of corotating disks. The catalyst will be on the surface of each disk and hence the specific catalyst surface will be higher. When only one pair is considered the catalyst will be on the interior surface of the disks. We aim to study numerically the flow for the arrangement described, to investigate its mixing properties and assess if its behavior is suitable to a chemical reactor application and if it improves the performance of the typical models. Two configurations are analyzed, discontinuous (batch) and semicontinuous. For the former type of operation, the cavity is filled with the reactant and then set to start working, for the latter one an external flow gets into the reactor through the outer wall while the reactor is operating. Several aspect ratios are analyzed and the behavior of the system under the variation of the parameters Re, Sc and ϕ (dimensionless kinetic constant) is analyzed for both configurations. We focus on the laminar regime for which the model remains 2D. (This part of our research has been already submitted to publication under the title “Enhancement of mixing in a catalytic chemical reactor consisting of a stack of corotating disks in a cylindrical enclosure” [45]).

As a second alternative to enhance mixing with application to a chemical reactor, we postulate a novel fashion of mixing enhancement by means of natural convection flow for which we expect shear rate decreases making this kind of reactor ideal for enzymatic type of reactions. Thus, we analyze numerically an approach where mixing within the reactor is promoted by fully static means, that is, no mechanical device nor forced convection flow is used. The components of agitation are eliminated by simply heating the reactor volume in order to generate a natural convection flow pattern. (This part of our research has been already published in the *Chemical Engineering Journal* **200**, p 506–520, 2012; under the title "Mixing intensification by natural convection with application to a chemical reactor design" [46]).

Rayleigh-Bènard convection, has been the object of study in the fluids physics field during several decades [47, 48]. There are several works in the literature where the potential of natural convection flow to increase mixing in confined flows is shown. However, none of them considered the application in a chemical reactor. De la Cruz et al. [49], for example, demonstrated that chaotic mixing in a bidimensional cavity can be achieved by imposing alternating hot and cold wall temperatures in a periodic manner. Gelfgat et al. [50], studied numerically two-fluid natural convection flow in an horizontal cylindrical annulus and its effect on mass transfer through the liquid-liquid interface of two immiscible fluids. They show that the mass transfer of a protein, for instance, through the interface can be significantly enhanced by the convective flow generated by heating the inner or outer cylindrical boundary. Ma et al. [51], modeled the flow in a cylindrical cavity heated from the side, showing that the basic steady flow that develops in such a situation is a toroidal pattern. On the other hand, Campbell et al. [52, 53], did consider a chemical reaction application. They investigated an exothermic reaction occurring in a spherical vessel, where the strong temperature gradients lead to the development of natural convection flows. In this way their results suggested that in liquid phase the natural convection flow is quite likely to favour a good mixing of reactant and product species.

Puigjaner et al. [54–57] has investigated very well stability in natural convection in a cubical cavity with constant bottom and top walls temperatures, T_h and T_c respectively ($T_h > T_c$), for Rayleigh numbers $Ra \leqslant 1.5 \times 10^5$. They have shown multiple stable stationary solutions of the momentum and energy conservation equation, as well as a great number of unstable solutions. In [54] analysis of the bifurcations and stability of steady convective flow pattern of air ($Pr = 0.71$) was done in a cubical cavity as described above, with adiabatically lateral walls. A Galerkin method with globally defined basis functions along with a parameter continuation method were used to determine the bifurcations and stability of the steady solutions. It was determined different stable steady flow patterns can coexist for moderate values of Ra. In [55] the same kind of cavity filled with silicon oil ($Pr = 130$) was studied. The variation of the Nusselt number as a function of Pr was also investigated for three of the stable flow patterns. The bifurcation diagram was determined and fifteen steady solutions were tracked. The stability analysis predicted that six flow patterns were stable and that two, three, or even four of these patterns coexisted over certain ranges of Ra. It was found that whereas the Nusselt changes within the region $0.71 \leqslant Pr \leqslant 10$ it tends to an asymptotic values with increasing Pr. Several Hopf bifurcations were identified within the region $Ra \geqslant 9 \times 10^4$. The symmetry properties of flow patterns were used to analyze their spatial configuration. Some of the flow patterns evolve to rather complex spatial configurations as the Rayleigh number increases. In general, all flow patterns tend to develop secondary rolls as the Rayleigh number increases. Bifurcation diagrams were found

to be strongly dependent on the Prandtl number and the evolution of flow patterns as the Rayleigh number increases is also rather dependent on Pr. The variation of the Nusselt number Nu with Pr reveals that heat transfer rates for any of the three stable solutions that set in at bifurcations from the conductive state change significantly within the region $0.71 \leqslant Pr \leqslant 10$ tending to an asymptotic value beyond. In [56] conducting sidewalls were imposed instead of the adiabatically ones previously studied. Both $Pr = 0.71$ and 130 were studied. For both cases bifurcation diagrams were more complex than those for adiabatic sidewalls. Four and nine different convective solutions were stable over certain ranges of Ra were identified at $Pr = 0.71$ and $Pr = 130$, respectively. The dependence of the bifurcation diagrams and of the topology of the flow patterns on the Prandtl number were also stronger in the case of conducting sidewalls. Most of the flow patterns investigated evolve to double toroid–like topologies with increasing Rayleigh number. In [57], Simó et al. investigated the mixing capacity in a cubical cavity with conducting sidewalls and $Pr = 130$, by means of dynamical systems tools. Using Poincaré maps they clarified the global structure of the flows studied. Regions with regular and chaotic motion were identified, showing chaotic region increase rapidly as Ra is increased. The chaotic nature of the flows has been quantified by the maximal Lyapunov exponent and the metric entropy. As a previous understanding of the flow inside a cubical cavity is known, there is room then to formulate the natural convection as the stimulus driving the mixing in catalytic and enzymatic reactors.

The natural convection setup that is selected in the present investigation is that of a cubical cavity with a difference of temperatures between the top and bottom walls and with adiabatic lateral sidewalls. There are three reasons for the choice of such a geometry. First, in the absence of previous knowledge on the subject it is reasonable to choose a simple geometry to start with. Second, a knowledge on the stability and dynamics of the flow patterns that can be generated by natural convection is necessary to control the type of circulation that mostly favors mixing. In this respect, we take advantage of the highly accurate numerical and analytical tools previously developed by Puigjaner et al. [54, 55]. Third, the current problem is a very challenging one from the numerical point of view. Most of the previous analytical and numerical studies of convection mass transfer into or from a solid interface relied on two-dimensional calculations or on a simplified version of the real three-dimensional flow geometry [12, 24]. The key point is that for realistic flow conditions, the cavity is filled with a liquid phase with properties similar to those of water, molecular diffusivity is much smaller than kinematic viscosity. In these conditions, molecular diffusion is dominating the total resistance to mass transfer within a very thin region in the vicinity of the catalytic surfaces.

An accurate calculation of concentration profiles within the region enclosed by the geometries of the setups described would be prohibitively expensive if classical methods, such as finite-elements or finite-differences, had to be used for the discretization of the differential conservation equations in three dimensions for the cubical reactor case or in two dimensions for the corotating disks reactor case. Nonetheless, the simplicity of the geometries selected in the present work, cylindrical and cubical, allows the development of a spectral Galerkin method which was implemented to solve the conservation equations.

Chapter 2

Problem formulation

2.1 Forced convection problem

2.1.1 Fluid mechanics model

An incompressible laminar flow of a Newtonian fluid inside a cylindrical catalytical chemical reactor is considered. The reactor, which is sketched in Fig.2.1, consists of two coaxial disks attached to and corotating with a hub enclosed in a cylindrical cavity. A first order catalytic chemical reaction takes place at the interior surface of each disk. The velocity and concentra-

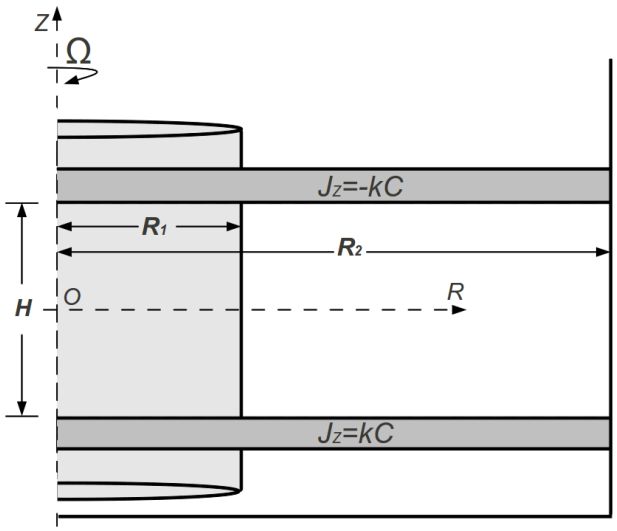

Figure 2.1: Sketch of the corotating disk reactor in the discontinuous operation mode. Note that since axisymmetry is assumed only the reactor projection into the radial–axial (R,Z) plane is shown. A first order catalytic chemical reaction takes place on the inner surface of each disk.

tion fields are assumed to be axisymmetric, that is, velocity and concentration depend only on the radial (R) and axial (Z) cylindrical coordinates. The $2D$–flow assumption is justified by the fact that within the range of Reynolds numbers investigated, ($Re \leqslant 10^5$), the flow is laminar. Notwithstanding, it is known that for each aspect ratio S there exists a bifurcation value, $Re_t \leqslant 10^5$, at which a three-dimensional (3D) flow arises from the basic axisymmetric flow [30, 32, 40]. The resulting 3D flow, however, is of the wavy type, that is, it can be understood as the circumferential oscillation with a given wavenumber of an averaged 2D flow which would be very similar to the corresponding solution of the axisymmetric branch at the same Reynolds number. Indeed, Herrero et al. [31] calculated the heat transfer between two corotating disks set at different temperatures and found no significant difference in the

respective Nusselt numbers computed for the 2D and the corresponding 3D flows at the same Re values. Under the aforementioned assumptions, the mass and momentum dimensionless conservation equations in a frame of reference rotating at the angular velocity Ω may be written as,

Mass

$$\frac{1}{S}\frac{\partial W}{\partial Z}+\frac{\partial U}{\partial R}+\frac{U}{R}=0 \tag{2.1}$$

Radial momentum

$$\frac{\partial U}{\partial \tau}+\frac{W}{S}\frac{\partial U}{\partial Z}+U\frac{\partial U}{\partial R}=-\frac{\partial P}{\partial R}+\frac{1}{Re}\left\{\frac{\partial}{\partial R}\left(\frac{1}{R}\frac{\partial}{\partial R}\left[RU\right]\right)+\frac{1}{S^2}\frac{\partial^2 U}{\partial Z^2}\right\}+\left(2V+\frac{V^2}{R}+R\right) \tag{2.2}$$

Circumferential momentum

$$\frac{\partial V}{\partial \tau}+\frac{W}{S}\frac{\partial V}{\partial Z}+U\frac{\partial V}{\partial R}=+\frac{1}{Re}\left\{\frac{\partial}{\partial R}\left(\frac{1}{R}\frac{\partial}{\partial R}\left[RV\right]\right)+\frac{1}{S^2}\frac{\partial^2 V}{\partial Z^2}\right\}-\left(2U+\frac{UV}{R}\right) \tag{2.3}$$

Axial momentum

$$\frac{\partial W}{\partial \tau}+\frac{W}{S}\frac{\partial W}{\partial Z}+U\frac{\partial W}{\partial R}=-\frac{1}{S}\frac{\partial P}{\partial Z}+\frac{1}{Re}\left\{\frac{1}{R}\frac{\partial}{\partial R}\left(R\frac{\partial W}{\partial R}\right)+\frac{1}{S^2}\frac{\partial^2 W}{\partial Z^2}\right\} \tag{2.4}$$

where R and Z are the dimensionless radial and axial coordinates, respectively; U, V and W are the dimensionless radial, circumferential and axial components of velocity, respectively; τ is the dimensionless time and P is the dimensionless pressure.

The length scales used to obtain the dimensionless variables in Eqs. (2.1)–(2.4) are R_2 and H respectively, so the nondimensional domain is:

$$\Upsilon=[\gamma,1]\times\left[-\frac{1}{2},\frac{1}{2}\right] \tag{2.5}$$

where $\gamma=R_1/R_2$ is the radius ratio. The velocity components, modified pressure $(p-\rho gz)$ and time were respectively scaled by the quantities,

$$U_0=\Omega R_2,\quad \mathcal{P}=\rho\Omega^2R_2^2\quad\text{and}\quad t_{diff}=R_2^2/D \tag{2.6}$$

Thus, Eqs. (2.1)–(2.4) depend on two dimensionless parameters, namely, the Reynolds number, Re, and the height to outer radius ratio, S, which are respectively defined as $Re=\Omega R_2^2/\nu$ and $S=H/R_2$. Ω is the angular velocity at which the disks rotate and ν is the kinematic viscosity. Note that in the rotating frame of reference the circumferential component of velocity, V, vanishes at the hub and disk surfaces. The rightmost term R in Eq. (2.2) denotes the centrifugal force while the terms $2V$ and $-2U$ within the rightmost parenthesis in Eqs. (2.2) and (2.3) are the respective components of the Coriolis force. The boundary conditions for equations (2.1)–(2.4) are

$$U=V=W=0\quad\text{at}\quad Z=\pm1/2\quad\text{and}\quad R=\gamma \tag{2.7}$$

$$U=W=0,\ V=-1\quad\text{at}\quad R=1. \tag{2.8}$$

Instead of solving the mass and momentum conservation equations in terms of velocity and pressure, we used the axisymmetric velocity potential, Ψ, also known as streamfunction,

$$U = -\left(\frac{1}{R}\right)\frac{\partial \Psi}{\partial Z} \tag{2.9}$$

$$W = \left(\frac{S}{R}\right)\frac{\partial \Psi}{\partial R} \tag{2.10}$$

It is clear that when Eqs. (2.9) and (2.10) are used, the continuity equation (2.1) is automatically fulfilled. Besides, boundary conditions (2.7) and (2.8) may be written as

$$V = \frac{\partial \Psi}{\partial Z} = \frac{\partial \Psi}{\partial R} = 0 \quad \text{at} \quad Z = \pm\frac{1}{2} \quad \text{and} \quad R = \gamma \tag{2.11}$$

$$V = -1 \quad , \quad \frac{\partial \Psi}{\partial Z} = \frac{\partial \Psi}{\partial R} = 0 \quad \text{at} \quad R = 1 \tag{2.12}$$

Note that since Ψ must be continuous along the boundary, Eqs. (2.11)–(2.12) can be replaced by

$$V = \Psi = \frac{\partial \Psi}{\partial Z} = 0 \quad \text{at} \quad Z = \pm\frac{1}{2} \tag{2.13}$$

$$V = \Psi = \frac{\partial \Psi}{\partial R} = 0 \quad \text{at} \quad R = \gamma \tag{2.14}$$

$$V = -1 \quad , \quad \Psi = \frac{\partial \Psi}{\partial R} = 0 \quad \text{at} \quad R = 1 \tag{2.15}$$

The mass and momentum conservation problem (2.1)–(2.8) is therefore determined by the values of three dimensionless parameters, namely the Reynolds number, Re, the height to outer radius ratio, S, and the radius ratio, γ. The latter quantity only appears explicitly in the boundary condition (2.15) at the rotating hub surface.

2.1.2 Mass transfer model

Two different operation modes, a discontinuous reactor and a semicontinuous reactor, were investigated. In the discontinuous reactor, sketched in Fig.2.1, the walls of the external cylinder were assumed to be impermeable. In the semicontinuous reactor, we considered that a steady flux entered the reactor through the external cylinder wall (see Fig.2.2). In both cases the catalytic reaction is assumed to take place on the surfaces of the corotating disks.

The dimensionless molar conservation equation of the solute species, can be written as

$$\frac{\partial C}{\partial \tau} = \left[\frac{1}{R}\frac{\partial C}{\partial R} + \frac{\partial^2 C}{\partial R^2} + \frac{1}{S^2}\frac{\partial^2 C}{\partial Z^2}\right] - ReSc\left[U\frac{\partial C}{\partial R} + W\frac{1}{S}\frac{\partial C}{\partial Z}\right] \tag{2.16}$$

where C is the molar concentration and $Sc = \nu/D$ is the Schmidt number, D being the binary coefficient of molecular diffusion for the solute/solvent pair and ν the kinematic viscosity as mentioned before. Boundary conditions for Eq. (2.16) can be defined as

$$\frac{\partial C}{\partial Z} = \pm\phi C \quad \text{at} \quad Z = \mp\frac{1}{2} \tag{2.17}$$

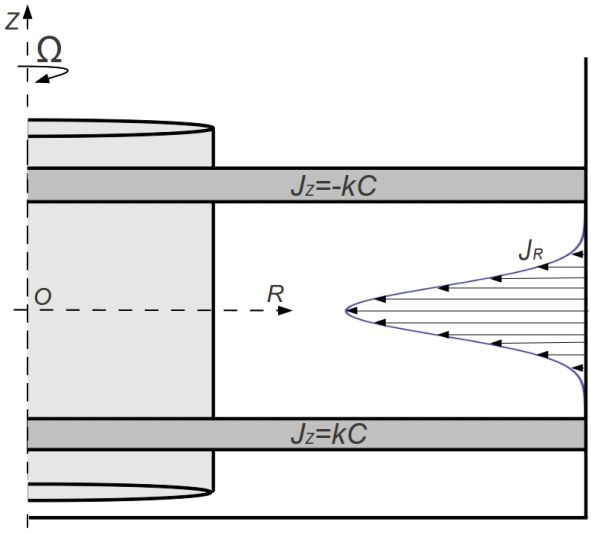

Figure 2.2: Sketch of the corotating disk reactor in the semicontinuous operation mode. The only difference with respect to the discontinuous reactor in Fig. 2.1 is in the molar flux of reactant, $J_R = J_R(Z)$, which is being continuously fed through the outer enclosure wall; see Eq. (2.19).

$$\frac{\partial C}{\partial R} = 0 \quad \text{at} \quad R = \gamma \tag{2.18}$$

$$\frac{\partial C}{\partial R} = J_R(Z) \quad \text{at} \quad R = 1 \tag{2.19}$$

where ϕ is the Damköhler number which represents the ratio of the rate of chemical reaction to the rate of molecular diffusion and it is defined as $\phi = kH/D$, k being the constant of the rate of chemical reaction. In Eq. (2.19) $J_R(Z)$ represents the flux entering the reactor through the external cylinder wall. Therefore, $J_R = 0$ when the discontinuous reactor is considered. In the case of the semicontinuous reactor we assumed a molar flux with a Gaussian profile that is constant in time. Thus, we used

$$J_R(Z) = Be^{-(2Z)^2/\sigma^2}. \tag{2.20}$$

2.2 Natural convection problem

We consider the incompressible flow of a Newtonian fluid in a cubical cavity with impermeable and adiabatic lateral walls. The Boussinesq approximation is used in the mass and momentum conservation equations, i.e., it is assumed that the fluid density varies linearly with temperature while the rest of physical properties and transport coefficients are constant through the whole domain.

The geometry of the problem is sketched in Fig. (2.3). The top and bottom walls are kept at uniform temperatures T_c and T_h ($T_c < T_h$), respectively. It is assumed that a first order catalytic chemical reaction takes place at the bottom plate of the cavity. The initial concentration of solute (reactant species) in the cavity is considered to be small enough not to alter the velocity field, that is, it is assumed that fluid density does not depend on concentration. Moreover, any effect of the heat of reaction is neglected.

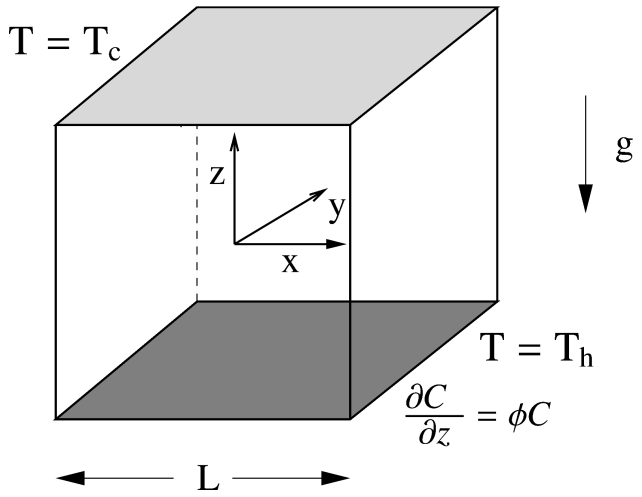

Figure 2.3: Sketch of the geometry of the problem of the cubical catalytical reactor driven by natural convection.

The dimensionless differential equations governing the conservation of mass, momentum and energy can therefore be written as:

$$\frac{1}{Pr}\left[\frac{1}{Le}\frac{\partial \mathbf{V}}{\partial \tau} + Ra^{1/2}\left(\mathbf{V}\cdot\nabla\right)\mathbf{V}\right] - \nabla^2\mathbf{V} - Ra^{1/2}\theta\,\mathbf{e_z} + \nabla p = 0 \tag{2.21}$$

$$\frac{1}{Le}\frac{\partial \theta}{\partial \tau} + Ra^{1/2}\left(\mathbf{V}\cdot\nabla\right)\theta - \nabla^2\theta - Ra^{1/2}\,w = 0 \tag{2.22}$$

$$\nabla\cdot\mathbf{V} = 0 \tag{2.23}$$

with boundary conditions

$$\begin{aligned} \mathbf{V} = \frac{\partial\theta}{\partial X} = 0 \quad &\text{at} \quad |X| = \frac{1}{2} \\ \mathbf{V} = \frac{\partial\theta}{\partial Y} = 0 \quad &\text{at} \quad |Y| = \frac{1}{2} \\ \mathbf{V} = \theta = 0 \quad &\text{at} \quad |Z| = \frac{1}{2} \end{aligned} \tag{2.24}$$

where X, Y and Z are the dimensionless cartesian coordinates, $\mathbf{V} = (u, v, w)$ is the dimensionless velocity vector, ∇ is the nabla operator in dimensionless cartesian coordinates, τ is the dimensionless time, θ is the dimensionless temperature, p is the dimensionless pressure and $\mathbf{e_z} = (0, 0, 1)^T$ is the unit vector in the Z direction. The dimensionless parameters governing the flow of the system are the Rayleigh number, $Ra = \beta\Delta T g L^3/(\alpha\nu)$; Prandtl number, $Pr = \nu/\alpha$ and Lewis number, $Le = Sc/Pr = \alpha/D$; where β is the coefficient of thermal expansion, ΔT is the vertical temperature drop $(T_h - T_c)$, g is the acceleration of the gravity, α is the thermal diffusivity, ν is the kinematic viscosity and D is the binary coefficient of molecular diffusion for the solute/solvent pair.

Equations (2.21-2.24) were adimensionalized on basis of the following scales: the volume of the cavity was scaled by the the length of its side, L, to obtain the nondimensional domain

$$\Upsilon = \left[-\frac{1}{2}, \frac{1}{2}\right] \times \left[-\frac{1}{2}, \frac{1}{2}\right] \times \left[-\frac{1}{2}, \frac{1}{2}\right], \tag{2.25}$$

the velocity, temperature, pressure and time were respectively scaled by the quantities,

$$U_0 = \left[\frac{\beta \Delta T g \alpha L}{\nu}\right]^{1/2}, \quad \Delta T = T_h - T_c \quad , \quad P = \frac{\rho \nu U_0}{L}, \quad \text{and} \quad t_{diff} = L^2/D. \tag{2.26}$$

Notice the scale that defines the dimensionless time, τ, is a characteristic time for molecular diffusion.

A value of $Pr = 6$, typical of water at ambient temperature, is assumed. The differential equation for the conservation of the solute species in terms of its molar concentration $C(\tau, X, Y, Z)$ may be written as:

$$\frac{\partial C}{\partial \tau} + \left(\frac{Sc}{Pr}\right) Ra^{1/2} \left(\mathbf{V} \cdot \nabla\right) C - \nabla^2 C = 0 \tag{2.27}$$

with boundary conditions

$$\begin{aligned} \frac{\partial C}{\partial X} &= 0 \quad \text{at} \quad |X| = \frac{1}{2} \\ \frac{\partial C}{\partial Y} &= 0 \quad \text{at} \quad |Y| = \frac{1}{2} \\ \frac{\partial C}{\partial Z} &= 0 \quad \text{at} \quad Z = \frac{1}{2} \end{aligned} \tag{2.28}$$

$$\phi C = -\left(\frac{J_Z L}{D}\right) = \frac{\partial C}{\partial Z} \quad \text{at} \quad Z = -\frac{1}{2}. \tag{2.29}$$

where J_Z is the vertical component of the solute molar diffusion flux and $\phi = kL/D$ is the Damköhler number, k being the constant of the chemical reaction rate. Equation (2.29) defines the first order catalytic chemical reaction at the bottom plate by equating the diffusive flux on the surface to the rate of chemical reaction.

Note that the Damköhler number, ϕ, is the ratio of t_{diff} to the characteristic time scale for the chemical reaction, L/k. A third relevant scale is the characteristic time for convective transport, $t_{conv} = L/U_0 = L^2/(\alpha Ra^{1/2})$. The ratio of the convective time scale to molecular diffusion time scale can be written as

$$\frac{t_{conv}}{t_{diff}} = \frac{D}{\alpha Ra^{1/2}} = \frac{(Pr/Sc)}{Ra^{1/2}} = \frac{1}{LeRa^{1/2}} \tag{2.30}$$

Equation (2.30) expresses the main idea that motivated the investigation of natural convection as a potential mixer. For values of the Rayleigh number of order $Ra = 10^5$ we have $t_{conv} \ll t_{diff}$, that is, natural convection is fast enough to provide adequate mixing levels to the reactor, especially when the cavity is filled with a liquid phase ($Le \gg 1$). Note that since the ratio of t_{conv} to L/k is equal to $\phi/(LeRa^{1/2})$ the natural convection–driven reactor would not be competitive in case of a very fast chemical reaction (very high values of the Damköhler number ϕ).

It is worth pointing out that Eqs. (2.21-2.24) are independent of Eqs. (2.27-2.29) and consequently they can be solved separately. The initial condition used to integrate in time the system (2.27-2.29) is discussed in Subsection 3.3.1 below.

The integration domain (2.25) and Eqs. (2.21-2.24) are respectively invariant and equivariant under the sixteen elements of the symmetry group D_{4h}. This group is generated by the reflection symmetries $\mathbf{S_y}, \mathbf{S_{d_+}}$ and $\mathbf{S_z}$ whose actions are described by:

$$\begin{aligned} \mathbf{S_y} :&(X, Y, Z) \to (X, -Y, Z) \\ &(u, v, w, \theta, C) \to (u, -v, w, \theta, C) \end{aligned} \tag{2.31}$$

$$\begin{aligned} \mathbf{S_{d_+}} :&(X, Y, Z) \to (Y, X, Z) \\ &(u, v, w, \theta, C) \to (v, u, w, \theta, C) \end{aligned} \tag{2.32}$$

$$\begin{aligned} \mathbf{S_z} :&(X, Y, Z) \to (X, Y, -Z) \\ &(u, v, w, \theta) \to (u, v, -w, -\theta) \end{aligned} \tag{2.33}$$

and which matricial form is represented by:

$$\mathbf{S_y} = \begin{pmatrix} 1 & 0 & 0 \\ 0 & -1 & 0 \\ 0 & 0 & 1 \end{pmatrix} \tag{2.34}$$

$$\mathbf{S_{d_+}} = \begin{pmatrix} 0 & 1 & 0 \\ 1 & 0 & 0 \\ 0 & 0 & 1 \end{pmatrix} \tag{2.35}$$

$$\mathbf{S_z} = \begin{pmatrix} 1 & 0 & 0 \\ 0 & 1 & 0 \\ 0 & 0 & -1 \end{pmatrix} \tag{2.36}$$

Note that any other symmetry can be defined by the subsequent application of the generator symmetries $\mathbf{S_y}, \mathbf{S_{d_+}}$ and $\mathbf{S_z}$. For example, $\mathbf{S_x} = \mathbf{S_{d_+}} \cdot \mathbf{S_y} \cdot \mathbf{S_{d_+}}$. Because of the lack of symmetry in the Z direction, Eqs. (2.27- 2.29) are only equivariant under the eight elements of the group D_4 generated by $\mathbf{S_y}$ and $\mathbf{S_{d_+}}$. The symmetries of the problem are used to reduce the computational effort and to understand the spatial configuration of flow and concentration patterns that are solutions of the governing equations.

Chapter 3

Numerical method

The main goal of the present work is to find the velocity and concentration fields of the established problems in order to evaluate different quantities that give us account of the behavior of the system. To achieve so, it is required to solve the set of partial differential equations (PDEs) that govern each system. Thus, basically it is necessary to discretize the set of equations after which is obtained a set of ordinary differential equations (ODEs) which can then be solved by any time–marching scheme. Several methods are used with this aim such as finite difference method, finite element method or spectral methods. We have used a Galerkin spectral method for the reasons that are discussed below.

Spectral methods are a class of spatial discretization for differential equations and it presents various formulations: Galerkin, tau, and collocation [58, 59]. Approximations are defined in terms of a truncated series expansion and it is considered that these methods belong to the general class of weighted residual methods in which some quantity that should be exactly zero, called the residual, is forced to be zero only in an approximate sense. The key components for its formulation are the trial functions and the test functions. The trial functions are linear combination of suitable basis functions and are used to provide the approximate solution of the system. If it is considered the expansion of a one–dimensional function $u(x)$ in the truncated series

$$u_N(x) = \sum_{i=0}^{N} \hat{u}_i \varphi_i(x), \quad \alpha \leqslant x \leqslant \beta \tag{3.1}$$

the $\varphi_i(x)$ are the trial functions, that in spectral methods are orthogonal, and the expansion coefficients $\hat{u}_i$ are the ones that must be determined. When the expansion $u_N(x)$ is substituted in the differential equation

$$Lu = f(x) \tag{3.2}$$

where L is the differential operator, the result is the so called residual function

$$R(x; \hat{u}_0, \hat{u}_1, ..., \hat{u}_N) = f - Lu_N. \tag{3.3}$$

The test functions are used to assure that the differential equation, and might be some of the boundary equations, are satisfied as much as possible in the truncated series expansion. This is achieved minimizing, with respect to an appropriate norm, the residual produced when the truncated expansion has been used instead of the exact solution [58]. The objective will be to made it zero in the mean, according to

$$\langle R, \psi_j \rangle_\omega = \int_\alpha^\beta \left(f - L \sum_{i=0}^{N} \hat{u}_i \varphi_i(x) \right) \psi_j \omega dz = 0, \quad j = 0, ..., N \tag{3.4}$$

where ψ_j are the test functions [58,59]. The spectral methods are distinguished by the particular choice of the trial functions. The most frequently used are trigonometrical polynomials, Chebyshev polynomials and Legendre polynomials. The choice of the test functions defines the method: Galerkin-type method uses the same test functions as the trial functions while the collocation method uses a Dirac delta–function. [59, 60]

One of the greatest advantages of the spectral methods, and the reason to use one of those methods, is the high accuracy obtained. The error obtained decay faster than any finite power of N due to the fact that the power in the error formula is always increasing too. This desirable property is known as exponential convergence. When many decimal places of accuracy are needed, these methods exceed by far the finite difference and finite element methods. For example, to equal the accuracy of a spectral procedure of, for instance, $N = 10$, one would need a tenth-order finite difference or finite element method with an error of $O(h^{10})$. Furthermore, even if not so high accuracy is needed, the high order of pseudospectral methods makes it possible to obtain the desired error with about half as many degrees of freedom, in each dimension, as needed for example by a fourth order method. To put it in another way, spectral methods are *memory-minimizing*. Problems that may require high resolution can often be solved satisfactorily by spectral methods when a three–dimensional second order finite difference code would fail because the need for eight or ten times as many grid points would exceed the core memory of the available computer [61].

Finite element methods are similar in their philosophy to the spectral methods. The main difference is that finite element cut the interval or region studied into several subintervals and choose the trial functions as local functions. On the other hand, spectral methods use basis global functions in which the trial function is a polynomial or a trigonometric polynomial. Advantages of the finite elements method are that the differential equations lead to sparse matrices and that in multidimensional problems, the subintervals can take different shapes such as triangles or tetrahedral to adjust them to irregular domains. Low precision due to the low degree in polynomials is a disadvantage, though. Spectral methods lead to algebraic equations with full matrices but in compensation the high basis functions degree achieve a high precision. As spectral methods use fast iterative processes, the resolution of the matrices could be much faster than in other kind of methods. However, they are more useful for soft and regular geometries [61]. Some disadvantages of the spectral methods are: *i)* That they are usually more difficult to program. *ii)* That they are more costly per degree of freedom. *iii)* That irregular domains lead to losses of accuracy and efficiency.

Once the set of partial differential equations is converted into a set of ordinary differential equations there is several time-marching schemes to solve them. Specifically, we have used two methods, the first one, a 7-8th order Runge-Kutta-Fehlberg method (*RK78*) [62] with adaptive time step, where the control of stepsize was done using the difference of the 7th and 8th order approximations, and the new stepsize is calculated by means of

$$h_{new} = 0.9 h_{old} \left[\frac{\delta}{e} \right]^{\frac{1}{1+p}} \tag{3.5}$$

where δ is the prescribed tolerance of the truncation error, e, which is defined by the difference between the solution obtained for each order used, i.e., 7th and 8th order, in this case, and p

is the order used, in this case 7th [62,63]. The second method we used was an implicit three-level second order backward-differencing scheme (*bdf2*). In it, the derivative is approximated by

$$\left(\frac{df}{dt}\right)_{n+1} \approx \frac{3f_{n+1} - 4f_n + f_{n-1}}{2\Delta t} \tag{3.6}$$

which leads to

$$f_{n+1} = \frac{4}{3}f_n - \frac{1}{3}f_{n-1} + \frac{2}{3}g(t_{n+1}, f_{n+1})\Delta t. \tag{3.7}$$

While the *RK78* explicit method is much more precise it has the flaw that tends to impose very small stepsize, which leads to very big times of calculations, on the other hand, the implicit *bdf2* method allows for the utilization of much bigger stepsize, furthermore this method has the property that for any $\Delta t > 0$ the error level is bounded in time, which is called A-stability.

The velocity field of the natural convection problem, had been previously solved by Puigjaner et al. for $Pr = 0.71$ and $Pr = 130$ in [54] and [55], respectively. Thus, this solution was used in the case $Pr = 6$. Numerical codes to find the concentration fields for both, natural and forced convection problems, were completely implemented from scratch by the author of the present thesis. Codes were written in programming language Fortran2003 under Linux and were run in a processor 4×Intel(R)Xeon(R) CPU E5620 @2.40GHz.

3.1 Forced convection problem

3.1.1 Velocity field

We begin assuming that the solute concentration, C, is small and therefore fluid properties, and more precisely, kinematic viscosity, ν, do not depend on C. Under this assumption, mass and momentum conservation equations (2.1)–(2.4) and (2.7)–(2.8) are solved independently of the solute (molar) conservation equations (2.16)–(2.19). In addition, only steady state solutions are considered. As discussed above, the steady flow assumption is reasonable in the range of low to moderate Reynolds numbers investigated, $10^3 \leqslant Re \leqslant 10^5$, even though the real flow would be three–dimensional, and thus unsteady, in the upper part of this Re range. The assumption of a steady velocity field implies that the time derivative in the left-hand-side of (2.2)–(2.4) vanishes.

The introduction of the streamfunction Ψ defined by (2.9)–(2.10) in the steady state version of (2.1)–(2.4) reduces from four (U, V, W, P) to three (Ψ, V, P) the number of dependent variables. The resulting system of partial differential equations was discretized by means of a spectral tau–Galerkin method, also known as Galerkin method with boundary bordering [61] where Chebyshev polynomials were used as basis functions:

$$\Psi(R, Z) = \sum_{i=4}^{N_{R,\Psi}} \sum_{j=4}^{N_{Z,\Psi}} \psi_{ij} f_i(R^*) f_j(Z^*) \tag{3.8}$$

$$V(R, Z) = \sum_{i=0}^{N_{R,V}} \sum_{j=0}^{N_{Z,V}} v_{ij} T_i(R^*) T_j(Z^*) \tag{3.9}$$

In expansions (3.8)–(3.9) $Z^* = 2Z$, $R^* = 2[(R-\gamma)/(1-\gamma) - 1/2]$, T_i denotes the Chebyshev polynomials of the first kind of order i and f_i are suitable linear combinations of Chebyshev polynomials that satisfy $f_i(\pm 1) = f_i'(\pm 1) = 0$. Thus, boundary conditions (2.13)–(2.15) for Ψ are automatically fulfilled with this choice of the basis functions. Note that no expansion is needed for the pressure, P, because the pressure gradient terms in (2.2) and (2.4) vanish when these equations, as an essential part of the Galerkin method, are projected into the subspace of the basis functions used in the Ψ expansion (3.8). As a result of the Galerkin projection, a system of nonlinear algebraic equations is obtained. This system of equations was solved for the unknowns, the ψ_{ij} and v_{ij} coefficients in the expansions (3.8) and (3.9), by means of the Newton iterative method.

A special treatment is needed to deal with the discontinuity in the boundary conditions for V at the external enclosure corners. That is, boundary conditions for V in (2.13) and (2.15) do not match as $0 = V(1, \pm 1/2) = -1$ is obviously impossible. Hence, we replaced the boundary condition $V(R, \pm 1/2) = 0$ in (2.13) by the following exponential function along the disk surfaces,

$$V(R, \pm 1/2) = -\exp\left[\frac{\ln(V_{res})}{\epsilon}(R-1)\right] \tag{3.10}$$

Equation (3.10) was inspired by the treatment of a similar velocity discontinuity at a boundary in a previous work by Lopez and Shen [64], which was later applied [65] to the calculation of the flow inside an annular container with a rotating bottom lid and inner cylinder. The idea behind the particular form of Eq. (3.10) is that at a small dimensionless radial distance from the outer enclosure wall, $\epsilon \ll 1$, V should already have attained a residual value $V = -V_{res} \approx 0$. In all of the calculations discussed below we used $V_{res} = 10^{-3}$ and $\epsilon = 0.05$. It was checked that using values of ϵ down to $\epsilon = 0.01$ yielded velocity fields that were basically indistinguishable from those obtained with the standard value $\epsilon = 0.05$. In order to implement the modified boundary condition (3.10) the radial span $R \in [\gamma, 1]$ was extended to $R \in [\gamma, 1+\epsilon]$ in Eqs. (2.1)–(2.4) and (2.7)–(2.8) as well as in in the molar conservation model (2.16)–(2.19) and in the definition of R^* (see appendix A).

The use of the V boundary condition (3.10) is justified on physical grounds by the fact that $\epsilon = 0$ is unattainable in an experimental equipment. From a theoretical point of view, it is known that in the limit case with $\epsilon \to 0$ a very large number of functions ($N_{R,V} \to \infty$) would be needed in expansion (3.9) to properly characterize the problem. When the current $V_{res} = 10^{-3}$ and $\epsilon = 0.05$ values were used in Eq. (3.10) it was numerically found that the required increase in the maximum polynomial degree reduced to $N_{R,V} \geqslant N_{R,\Psi} + 20$. When values of $N_{R,V}$ not fulfilling this constraint were used the resulting V velocity fields turned out to be somewhat *wiggly* in the vicinity of the disk surfaces, $Z = \pm 1/2$. Furthermore, in all of the cases investigated we set identical values of the truncation parameters for the axial direction in expansions (3.8) and (3.9), that is, $N_{Z,\Psi} = N_{Z,V}$.

3.1.2 Concentration field

The solute conservation equation (2.16) was solved by means of a spectral tau–Galerkin method, using the concentration expansion

$$C(\tau, R, Z) = \sum_{i=0}^{N_R} \sum_{j=0}^{N_Z} c_{ij}(\tau) T_i(R^*) T_j(Z^*) \tag{3.11}$$

where c_{ij} are the unknown time–dependent expansion coefficients of the truncated expansion for the concentration. The application of the tau–Galerkin method reduces Eqs. (2.16)–(2.19) into an ordinary differential equation that can be written as

$$\hat{\mathbf{B}}\dot{\mathbf{c}} = \hat{\mathbf{Q}}\mathbf{c} + \hat{\mathbf{A}} \tag{3.12}$$

The vector $\mathbf{c}$ and the matrices $\hat{\mathbf{B}}$, $\hat{\mathbf{Q}}$ and $\hat{\mathbf{A}}$ in Eq. (3.12) are defined in appendix A where the tau–Galerkin method is detailed.

Equation (3.12) was advanced in time for both the discontinuous and semicontinuous configurations using the *bdf2* scheme [62]. The initial condition for the discontinuous mode is that the reactant species is perfectly mixed, i.e., $C(0, R, Z) = 1$. However, we used a slightly modified initial concentration distribution (explained in Subsection 3.3.1) in order to fulfill boundary condition (2.17) at $\tau = 0$. For the semicontinuous configuration the initial concentration field was set to $C(0, R, Z) = 0$, which means that initially there is no reactant inside the reactor volume. In the case of the semicontinuous reactor the steady state was determined by solving the linear system

$$\hat{\mathbf{Q}}\mathbf{c} = -\hat{\mathbf{A}} \tag{3.13}$$

that follows from Eq. (3.12). The systems of linear equations in (3.12) and (3.13) were solved using the LAPACK numerical package [66, 67].

In the semicontinuous case, the amplitude B of the Gaussian flux in (2.20), was chosen so that the average concentration on the disks, $\widehat{C}(\tau, \pm 1/2)$, was equal to 1, for the time $\tau = \tau_S$ at which the reactor reaches a stationary state, i.e., when the rate of solute fed is equal to the rate of solute consumed. To find the value of B that fulfills the conditions stated above, we make the following considerations: From Fick's law we got

$$\frac{dC}{dR} = \frac{R_2}{D} J_r(z) = J_R(Z) \tag{3.14}$$

where z is the axial coordinate in m and

$$J_r(z) = Ae^{-(2z)^2/(H\sigma)^2} \tag{3.15}$$

is the flux getting into the reactor through the external wall in mol/(m^{2}s). Hence, taking into account (2.20) and (3.15) B can be expressed as

$$B = \frac{R_2}{D} A. \tag{3.16}$$

Now, to find the appropriate value of A, we perform the mass balance so that indeed the solute fed equals the solute consumed,

$$2\left(2\pi \int_{R_1}^{R_2} J_z(r) r dr\right) = 2\pi R_2 \int_{-H/2}^{H/2} J_r(z) dz \tag{3.17}$$

r is the radial coordinate in m and $J_z(r)$ is the flux on the disks in mol/(m^{2}s) which for a first order chemical reaction is $J_z = kC(t, r, z)$. The left hand side of the equality corresponds to the amount of solute consumed (the 2 before the parenthesis indicates the two disk surfaces) and the right hand side of the equality corresponds to the amount of solute fed through the external wall. Using the dimensionless variables we got

$$2kR_2^2 \int_{\gamma}^{1+\epsilon} C(\tau, R, Z) R dR = R_2 H \int_{-1/2}^{1/2} J_r(Z) dZ \tag{3.18}$$

where the integration is carried out until $1+\epsilon$, taking into account the small gap between the tip of the disk and the external wall of the cylinder, as explained above in Subsection 3.1.1 (Eq. (3.10)). To express the left hand side integral in a different way, let us define the average concentration over the disk surface as

$$\widehat{C}(\tau, \pm 1/2) = \frac{2\pi \int_{\gamma}^{1+\epsilon} C(\tau, R, \pm 1/2) R dR}{\pi \left((1+\epsilon)^2 - \gamma^2\right)} \tag{3.19}$$

Thus,

$$\int_{\gamma}^{1+\epsilon} C(\tau, R, \pm 1/2) R dR = \frac{1 + 2\epsilon + \epsilon^2 - \gamma^2}{2} \widehat{C}(\tau, \pm 1/2) \tag{3.20}$$

Inserting (3.20) in (3.18), taking into account (3.15) and that k can be expressed as $k = \phi D/H$, we have

$$\frac{2\phi D}{H} R_2^2 \widehat{C}(\tau, \pm 1/2)(1 + 2\epsilon + \epsilon^2 - \gamma^2) = R_2 H A \int_{-1/2}^{1/2} e^{-(2Z)^2/\sigma^2} dZ \tag{3.21}$$

As we stated above, we want to impose the condition that $\widehat{C}(\tau, \pm 1/2) = 1$ in the stationary state, when the solute fed equals the solute consumed, hence

$$\frac{2\phi D}{H} R_2^2 (1 + 2\epsilon + \epsilon^2 - \gamma^2) = R_2 H A \int_{-1/2}^{1/2} e^{-(2Z)^2/\sigma^2} dZ \tag{3.22}$$

Calling I the integral on the right hand side

$$I = \int_{-1/2}^{1/2} e^{-(2Z)^2/\sigma^2} dZ \tag{3.23}$$

the constant A will be equal to

$$A = \frac{2\phi D (1 + 2\epsilon + \epsilon^2 - \gamma^2)}{I R_2 S^2} \tag{3.24}$$

and finally, applying (3.16) we have the following expression for the constant B of the Gaussian profile of the flux entering the external wall,

$$B = \frac{2\phi (1 + 2\epsilon + \epsilon^2 - \gamma^2)}{I S^2}. \tag{3.25}$$

3.2 Natural convection problem

As previously mentioned, the velocity field of the natural convection problem, had been previously solved by Puigjaner et al. [54] for $Pr = 0.71$. Thus, the solution for our problem with $Pr = 6$ was found using their algorithms. Both set of equations (2.21-2.24) and (2.27-2.29) were discretized by means of a Galerkin spectral method. As discussed above, a spectral method was chosen for the discretization of the governing equations due to its high efficiency when applied to regular domains [61,68,69]. The complete, divergence-free set of basis functions reported in [54] was used to characterize the steady solutions of Eqs.(2.21-2.24). This

set of basis functions has the property that boundary conditions (2.24) are automatically fulfilled. Once velocity and temperature are approximated by truncated expansions in terms of the basis functions the governing partial differential equations are transformed into a system of ordinary differential equations whose unknowns are the coefficients in the expansions. These ODEs are then projected into the subspace generated by the basis functions and the resulting system is solved, if a steady state solution is being sought, or advanced in time otherwise. It is worth noting that pressure is eliminated from the equations in the process of projection (see [54] for details). The Galerkin method was combined with a continuation procedure to determine steady solutions branches for the target value of the Prandtl number, $Pr = 6$. The bifurcations and stability character of the different solution branches were determined in the range of Rayleigh numbers with $Ra_c \leqslant Ra \leqslant 1.5 \times 10^5$; here, Ra_c denotes the critical Rayleigh number for the onset of convection, $Ra_c = 3389$ [54, 70].

3.2.1 Concentration field

In order to solve Eqs. (2.27-2.29) the concentration of the solute species, C, was expanded according to

$$C(\tau, X, Y, Z) = \sum_{i=2}^{N}\sum_{j=2}^{N}\sum_{k=1}^{N} c_{ijk}(\tau) h_i(X) h_j(Y) h_k(Z) \tag{3.26}$$

where $c_{ijk}(\tau)$ are the unknown time-dependent coefficients of the truncated expansion. The basis functions chosen in Eq. (3.26) have the form,

$$\begin{aligned} h_1(Z) &= T_2(Z^*) - 4T_1(Z^*) \\ h_2(Z) &= T_0(Z^*) \\ h_k(Z) &= T_k(Z^*) - \frac{k^2}{(k-2)^2} T_{k-2}(Z^*), \quad k \geq 3 \end{aligned} \tag{3.27}$$

where $T_k(Z^*)$ are Chebyshev polynomials of the first kind and $Z^* = 2Z$. The same basis functions are defined for the X and Y expansions with the exception of $h_1(Z)$. Since the basis functions (3.27) satisfy ($h_k'(\pm 1/2) = 0 \; \forall \; k > 1$) the concentration boundary conditions (2.28) are implicitly fulfilled. On the contrary, Eq. (2.29) has to be projected into the subspace defined by the functions of the type $h_i(X)h_j(Y)h_1(Z)$. Equations (2.21-2.24), which do not depend on the concentration field, were solved for the velocity and temperature fields under the assumption of small solute concentrations. Once the velocity field was obtained, it was introduced in Eqs. (2.27-2.29) to calculate the time evolution of the concentration field.

For the sake of homogeneity between Eqs. (2.21-2.24) and (2.27-2.29), the calculated velocity fields were projected into the space generated by Chebyshev polynomials. Thus, u, v and w were expanded as,

$$\begin{aligned} u(X, Y, Z) &= \sum_{p=0}^{M}\sum_{q=0}^{M}\sum_{r=0}^{M} u_{pqr} T_p(X^*) T_q(Y^*) T_r(Z^*) \\ v(X, Y, Z) &= \sum_{p=0}^{M}\sum_{q=0}^{M}\sum_{r=0}^{M} v_{pqr} T_p(X^*) T_q(Y *^{)}\, T_r(Z^*) \\ w(Z, Y, Z) &= \sum_{p=0}^{M}\sum_{q=0}^{M}\sum_{r=0}^{M} w_{pqr} T_p(X^*) T_q(Y^*) T_r(Z^*) \end{aligned} \tag{3.28}$$

where u_{pqr}, v_{pqr} and w_{pqr} are the velocity coefficients in the new basis and $X^* = 2X$, $Y^* = 2Y$ like the variable Z^* explained above. The value of the truncation parameter M in expansions (3.28) was chosen large enough to guarantee that the mass conservation constraint was accomplished to machine accuracy. When expansions (3.26) and (3.28) are introduced in Eq. (2.27) and (2.29) and the result is projected into the subspace of basis functions an ODE system arises:

$$\mathbf{B}\dot{\mathbf{c}} = \mathbf{Q}\mathbf{c} \tag{3.29}$$

In Eq. (3.29) $\mathbf{B}$ and $\mathbf{Q}$ are square matrices and $\mathbf{c}$ is a vector with the coefficients of the concentration expansion. Details of the structure of these matrices are given in the appendix B. Arranging the indices of the unknown time–dependent coefficients according to their parity [54], the matrices $\mathbf{B}$ and $\mathbf{Q}$ have a 8×8 block structure. Each of these blocks is a $N_D \times N_D$ square matrix where $N_D = \left(\frac{N-1}{2}\right)^3$ and N is the number of polynomial functions used in expansion (3.26). For solutions with some specific symmetries it is possible to reduce the dimension of the problem since the number of non-zero blocks in $\mathbf{B}$ and $\mathbf{Q}$ reduces to 4×4.

3.2.2 Dynamical Analysis

The mixing capabilities of the natural convection flow are assessed by means of a methodology that combines the Eulerian and Lagrangian representations of fluid motion. The methods used in the present study were used by Simó et al. [71]. These authors used dynamical systems tools to assess the mixing capabilities of several Rayleigh-Bénard convection flow patterns in a cubical cavity with perfectly conducting sidewalls at $Pr = 130$. The basis of the methodology is to find the trajectories of a large number (512) of passive particles that are initially uniformly seeded through the whole volume of the cavity , integrating in time the equations

$$\dot{x}_1 = u_1(x_1, x_2, x_3), \quad \dot{x}_2 = u_2(x_1, x_2, x_3), \quad \dot{x}_3 = u_3(x_1, x_2, x_3) \tag{3.30}$$

by means of a *RK78* method. In all the current calculations the local error tolerance in the *RK78* procedure was set to 10^{-12} and the integration is performed until a time equal to 2×10^3. Particle trajectories allow the calculation of Poincaré maps and several quantities that are considered good indicators of mixing, such as percentage of chaotic region or maximal Lyapunov's exponents [72, 73].

A Poincaré map can be obtained by considering the intersections of several particle trajectories with a certain lower–dimensional subspace, called the Poincaré section. Poincaré maps are useful to distinguish well–mixed chaotic regions from unmixed regular regions in the flow and to qualitatively identify changes in the shape of these regions as one or more parameters vary.

Regular regions are characterized by the presence of nested invariant tori. These, represent an important obstacle to efficient mixing. Consequently, the knowledge of the shape and size of regions with regular flow motion would be determinant in predicting the mixing efficiency of the flow. We used the algorithm developed in [71] which is based on the trajectories of several initial conditions to estimate the shape and size of these regular regions. The key ideas of the algorithm are:

i) The cubical cavity is divided into $n \times n \times n$ equally sized cubic cells (in this case $n = 200$).

ii) For each initial condition x_0 in a certain set C_I, the trajectory described by a fluid particle initially located at x_0 is calculated by numerically integrating Eq. (3.30) (in this case $C_I = \{(-0.375 + i/4, 0.48, -0.375 + j/4), i, j = 0, ..., 6\}$).

iii) At each integration time step, the cubic cells that have been visited by one or more fluid particle trajectories are stored.

iv) The number of cells $N_r(t)$ that at time t have not yet been visited by any particle trajectory is calculated for any t multiple of the selected Δt (in this case $\Delta t = 200$).

v) The procedure is stopped when the integration time exceeds a maximum integration time t_M (in this case $t_M = 5 \times 10^5$).

It is worth to note that the symmetry properties of the studied flow patterns were used to reduce the calculations. The chaotic zone is understood as the set of points in the cubical domain which are outside invariant tori. Of course, there are small chaotic zones bounded by tori, but they hardly contribute to the mixing.

A quantitative analysis of the mixing efficiency of a given flow pattern can be obtained by computing the maximal Lyapunov exponent L_M. A Lyapunov exponent is a magnitude that indicates the rate of separation of infinitesimally close trajectories. Two trajectories with initial separation δ_0 diverge at a rate

$$|\delta_t| \approx e^{\lambda t}|\delta_0| \tag{3.31}$$

where λ is the Lyapunov exponent. This can be different for different orientations of initial separation vector. The largest one of the λs is called the maximal Lyapunov exponent L_M. A positive L_M is commonly a signal of *chaoticity* in the system. Lyapunov exponents are related to the mixing efficiency of the fluid flow system [71, 74].

3.3 Accuracy assessment

3.3.1 One–dimensional limit

The species conservation equations (2.16) and (2.27) are considered in the diffusive limit case, when Re and Ra are equal to zero, respectively. In this limit the mentioned equations reduce to the following one-dimensional (1D) problem

$$\frac{\partial C(\tau,\xi)}{\partial \tau} - \frac{\partial^2 C(\tau,\xi)}{\partial \xi^2} = 0 \tag{3.32}$$

with boundary conditions

$$\frac{\partial C(\tau,\xi)}{\partial \xi} = \phi C(\tau,\xi) \quad \text{at} \quad \xi = 0 \tag{3.33}$$

$$\frac{\partial C(\tau,\xi)}{\partial \xi} = 0 \quad \text{at} \quad \xi = 1 \tag{3.34}$$

which reflect the catalytic reaction and zero flux boundary conditions respectively. For the natural convection problem, $\xi = 1/2 - Z$. Considering the forced convection problem, we see there is a symmetry of the boundary conditions with respect to the plane $Z = 0$, the

same catalytic reaction is occurring on each disk. Thus, we can divide the domain of the problem in two subdomains, namely, $[-1/2, 0]$ and $[0, 1/2]$. Notice that for each subdomain the catalytic reaction is taking place in the inferior (superior) extreme and the zero flux condition is happening at the superior (inferior) extreme. Hence, for the first subdomain, $\xi = 1 + 2Z$, while for the second subdomain $\xi = 1 - 2Z$.

It is known that Eqs. (3.32-3.34) with initial condition

$$C(0, \xi) = 1 \tag{3.35}$$

have the following analytical solution [75],

$$C^a(\tau, \xi) = 2 \sum_{i=1}^{\infty} \frac{1}{\mu_i} \left[1 + \frac{1}{\phi} + \left(\frac{\mu_i}{\phi} \right)^2 \right]^{-1} \frac{\cos(\mu_i \xi)}{\sin \mu_i} e^{-\mu_i^2 \tau} \tag{3.36}$$

where the eigenvalues μ_i are the roots of the equation

$$\frac{\cos \mu}{\sin \mu} = \frac{\mu}{\phi} \tag{3.37}$$

A very good numerical approximation of this analytical solution can be obtained by using the first one–thousand terms in series (3.36) provided that the time τ is not too close to zero. Figures 3.1 and 3.2 show the concentration profiles for the natural and forced convection problems, respectively, for $\tau = 1 \times 10^{-3}$ and $\phi = 1$.

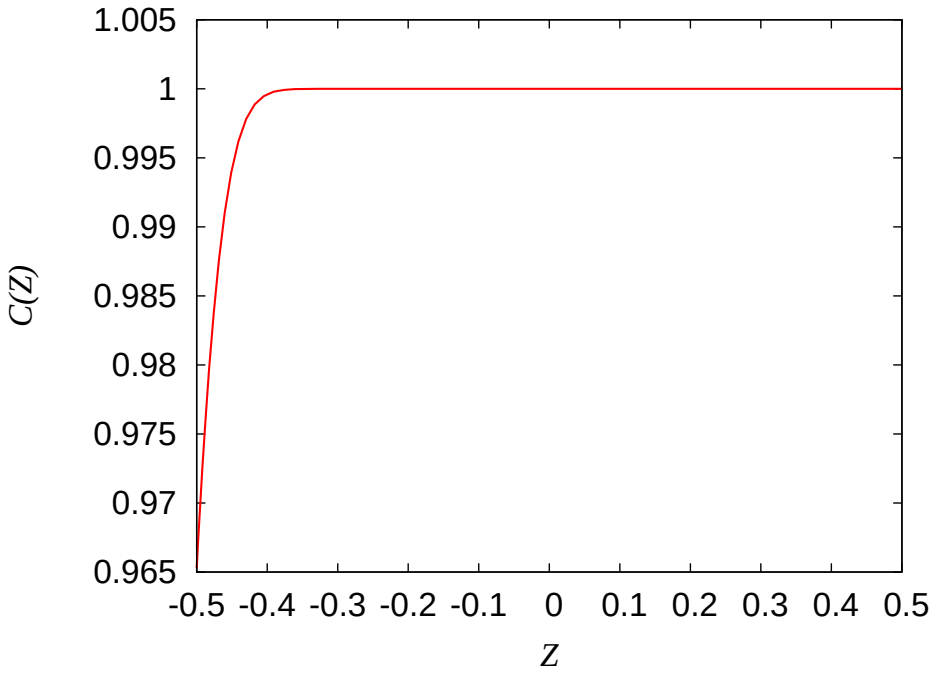

Figure 3.1: Concentration profile in the case $\phi = 1$ and $\tau = 1 \times 10^{-3}$ for the 1D natural convection problem.

On the other hand, when a simplified version of the Galerkin method is applied to Eqs. (3.32-3.33) the 1D problem is converted into an ODE system of the form:

$$\mathbf{B}_{1D} \dot{\mathbf{c}}_{1D} = \mathbf{Q}_{1D} \mathbf{c}_{1D} \tag{3.38}$$

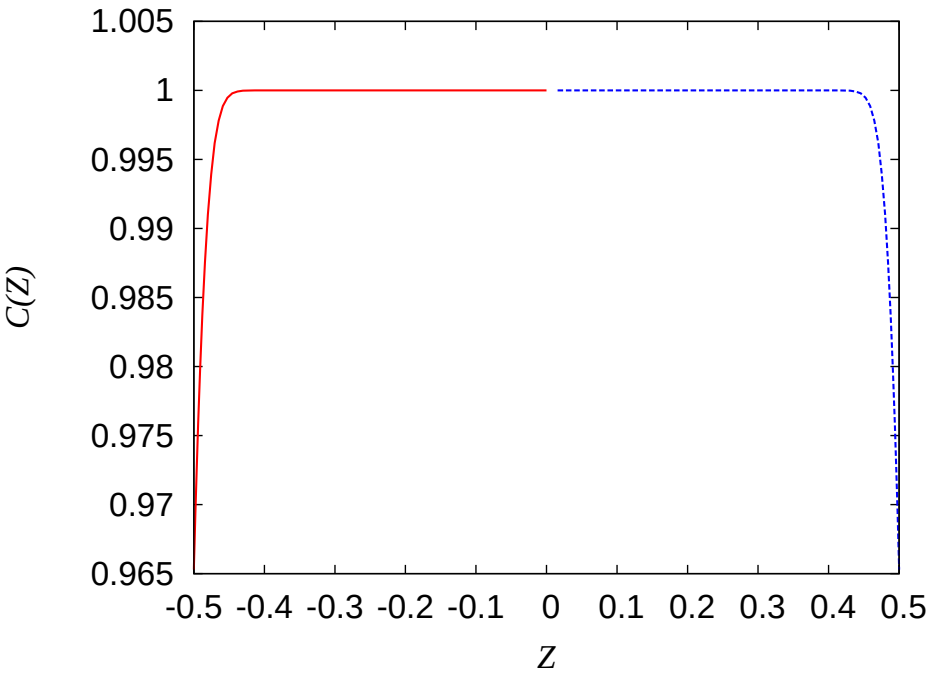

Figure 3.2: Concentration profile in the case $\phi = 1$ and $\tau = 1 \times 10^{-3}$ for the 1D forced convection problem.

The accuracy of the current implementation of the *RK78* time–integrator was tested by solving Eq. (3.38) both analytically and numerically. The analytical solution of the ODE system (3.38) may be written as:

$$\mathbf{c}_{1D}(\tau) = \left[e^{\left(\mathbf{B}_{1D}^{-1}\mathbf{Q}_{1D}\right)\tau} \right] \mathbf{c}_{1D}(\tau_0) \tag{3.39}$$

For any given value of the truncation parameter N, the analytical time evolution (3.39) and the one given by the *RK78* integrator are identical down to an accuracy level of order 10^{-9} in terms of relative error. The numerical solutions given by the *RK78* integrator could be made even more accurate by fine–tuning the algorithm for the automatic adjustment of the time–step [62] but that would be at the expense of a larger computational time. In order to assess the accuracy of the Galerkin spatial discretization, the numerical solutions of (3.38) obtained with different values of N were compared with the analytical solution (3.36) (truncated at $i = 1000$). The evolutions in time of the relative difference of the solute concentration at the bottom surface, $E = |C^a(\tau, -1/2) - C(\tau, -1/2)|/C^a(\tau, -1/2)$, are plotted in Fig. 3.3 for $\phi = 100$ and different values of N. Note that due to the boundary condition (3.33) the quantity plotted in Fig. 3.3 is equivalent to the relative error in the calculated molar fluxes entering the bottom catalytic surface, $J_Z(\tau, -1/2)$. Figure 3.3 shows that the maximum relative errors vary between approximately 1.5×10^{-2} for $N = 11$ and 10^{-5} for $N = 29$. A value of $N = 19$ would be a good compromise between accuracy and efficiency for solving the 1D diffusion-reaction problem.

The analytical solution (3.36-3.37) of the $1D$ problem (3.32-3.35) at a time τ_0 very close to zero would seem a suitable choice as an initial condition for the numerical integration of (3.12) and (3.29), i.e., $C(\tau_0, X, Y, Z) = C^a(\tau_0, Z)$ or $C(\tau_0, R, Z) = C^a(\tau_0, Z)$ in the corresponding Z domains. However, the initial $1D$ concentration profile at a very small τ_0 is too similar to a step function of Z and, thus, very difficult to project into a polynomial basis (an unreasonably high value of N would be necessary). Therefore, an initial value of time not so close to zero, namely $\tau_0 = 0.001$, was used instead. In physical terms, this choice might be interpreted as

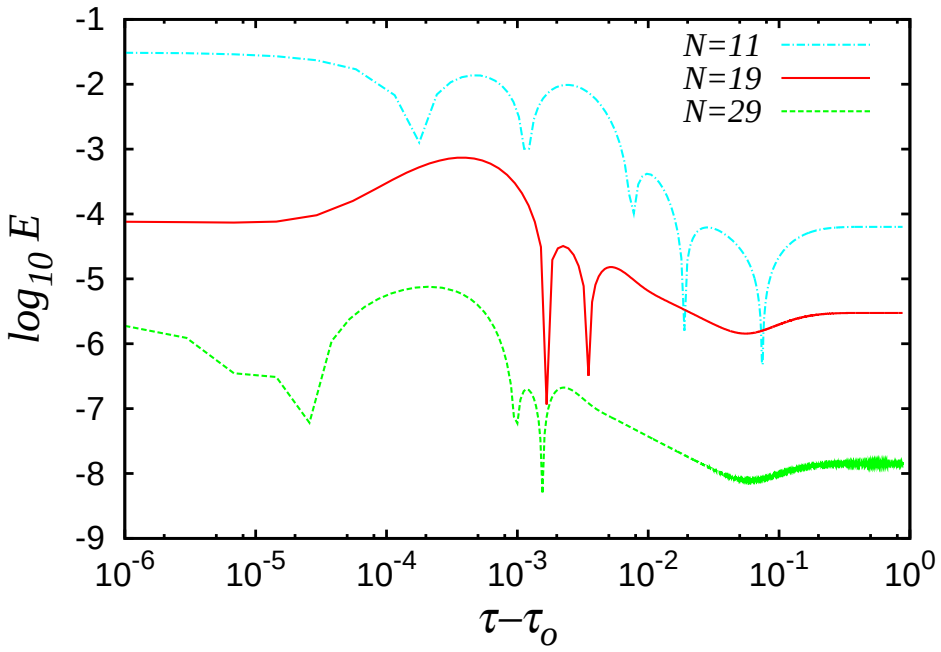

Figure 3.3: Discretization errors in the numerical integration of the 1D problem for different values of the truncation parameter N. The quantity plotted is the relative error $E = |C^a(\tau, -1/2) - C(\tau, -1/2)|/C^a(\tau, -1/2)$, where $C(\tau, -1/2)$ is the value of the solute concentration at the bottom wall obtained from the numerical integration of the system (3.38) and $C^a(\tau, -1/2)$ is the corresponding analytical value given by Eq. (3.36).

a delayed start of the natural convection in the reactor (note that for example in the natural convection problem, for Rayleigh numbers below $Ra_c = 3389$ there is no convection). As it is shown below, the use of this delayed start procedure has no qualitative effect on the results obtained.

3.3.2 Forced convection problem

Velocity field

As discussed above, the flow between a pair of corotating disks has been thoroughly investigated in the last decades. The accuracy of the current numerical results can be therefore checked by comparing them with some well–established numerical results. In particular we compared our results with those obtained by Herrero et al. [30] for $Re = 13710$, $S = 0.091$ and $\gamma = 0.537$. Figures 3.4a and 3.4b respectively show the current calculated contours of Ψ and V that were obtained with $N_{R,\Psi} = N_{Z,\Psi} = 21$. These results agree very well with the corresponding contours reported in [30] where a second-order finite-difference method with grid sizes as large as 200 and 100 in the radial and axial directions, respectively, was used instead. Notwithstanding, in order to guarantee the accuracy of the calculated velocity fields a minimum of $N_{R,\Psi} = 41$ and $N_{Z,\Psi} = 41$ was used even for the smaller Reynolds numbers considered ($Re = 10^3$). For $S = 0.25$ it was found that the number of basis functions in expansions (3.8) and (3.9) had to be increased as Re increased up to $N_{R,\Psi} = 91$ for $Re = 10^5$. An increase in the aspect ratio S also forced an increase in the truncation parameter up to $N_{Z,\Psi} = 101$ for the maximum S value investigated, $S = 1$.

a)

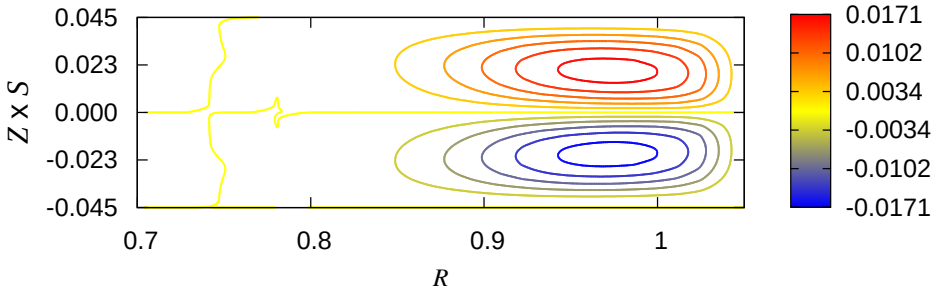

b)

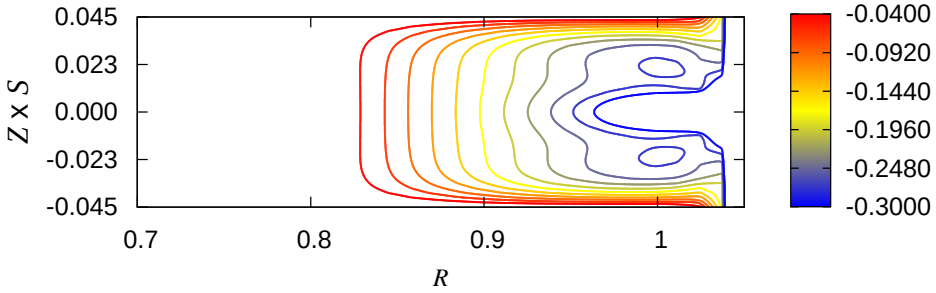

Figure 3.4: Velocity field obtained in a calculation with $Re = 13710$, $S = 0.197$ and $\gamma = 0.537$ a) Flow streamlines with Ψ levels ranging between -0.017076 and 0.017076 with an increment of 0.0034152. b) Contours of V levels ranging between -0.300 and -0.040 with an increment of 0.026. The contour levels match those plotted in [30] except for a factor of 2.81 between the respective Ψ levels due to a different choice of the reference flow rate, $\Omega H R_2^2(1-\gamma^2)/2$ instead of the current $\Omega H R^2$.

Concentration Field

The *bdf*2 scheme was used to advance in time the ODE system. A timestep equal to 10^{-4} was used for the lowest ϕ values studied and 10^{-5} otherwise. A preliminary set of calculations was performed for $Sc = 1$ using the same truncation parameters in expansion (3.11) that were previously used in the velocity calculation, that is $N_r = N_{R,\Psi}$ and $N_z = N_{Z,\Psi}$. We subsequently increased N_r and N_z until the calculated concentration field became basically independent of the truncation parameters. The values of N_r and N_z had to be increased with increasing Schmidt number, Sc, as the length scale for molecular diffusion becomes increasingly smaller. Figure 3.5 illustrates the convergence of the concentration field with increasing values of the truncation parameters for the case of the discontinuous reactor with $Re = 8 \times 10^4$, $Sc = 100$ $S = 0.25$ and $\phi = 2000$. This figure shows axial profiles of the

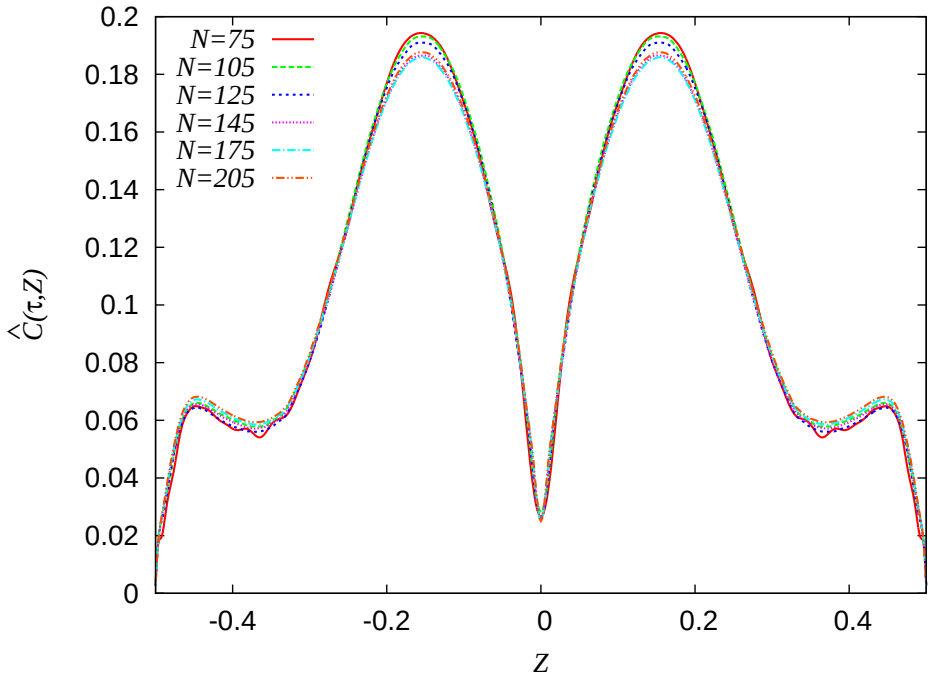

Figure 3.5: Axial profiles of the radially averaged concentration field, $\widehat{C}(\tau, Z)$, at the time instant $\tau = \tau_{90}$ when a reactant conversion of 90% is reached. Results from several calculations with $Re = 8 \times 10^4$, $Sc = 100$, $S = 0.25$, $\phi = 2000$ and different values of the truncation parameter, $N = N_R = N_Z$ in Eq. (3.11), are included.

radially averaged concentration at the time instant at which a reactant conversion of 90% was reached. The most significant differences between the profiles obtained with different values of the truncation parameter, $N = N_R = N_Z$, are observed at the maxima located at $Z = \pm 0.156$ and at the local minima at $Z = \pm 0.371$. In the latter point we can even see that for the lowest resolution $N = 75$ the profile is wiggly. The appearance of wiggles due to insufficient spatial resolution was frequently observed in preliminary low–resolution calculations at $Sc = 100$ and 1000. As it can be seen in Fig. 3.5, in this particular case with $Sc = 100$ a truncation value as high as $N = 205$ had to be used to achieve convergence of the calculated solution. In general, a value of the truncation parameter $N = \max(N_R, N_Z)$ equal or larger than $N = 175$ had to be used in calculations for the discontinuous reactor with $Sc = 100$ and values as high as $N = 251$ had to be used in most of the calculations with $Sc = 1000$ in which the time of calculation was around 9.7×10^4 s of CPU time.

In the semicontinuous reactor, calculations were even more demanding due to the presence of much larger concentration gradients in the region near the outer enclosure wall. Preliminary calculations were also carried out for all of the four values of the Schmidt number, $Sc = 1, 10, 100$ and 1000. However, it was found that part of the calculations with $Sc \geqslant 100$ were not properly converged even with the highest N values that we could use without exceeding the available computer memory (24 GBytes). This is the reason why only results with $Sc \leqslant 10$ are included in Section 4.2.3 below. For most of steady calculations the computational workload was around 8.6×10^2 s of CPU time.

3.3.3 Natural convection problem

It is important to notice that the results of the 1D limit do not apply only for $Ra = 0$ but also for $Ra < Ra_c$, that means the no convection limit. The three-dimensional problem (3.29) that arises whenever $Ra > Ra_c$ is more challenging. The point is that as the $LeRa^{1/2}$ factor in Eq. (2.27) increases the matrix $\mathbf{Q}$ in Eq. (3.29) becomes worse conditioned and consequently a larger value of N has to be prescribed. This numerical tendency can be understood as a consequence of the change in the physics of the problem as $LeRa^{1/2}$ increases: concentration gradients are restricted to an increasingly thinner layer in the vicinity of the walls and thus they become increasingly steeper. The numerical results obtained from (3.29) tend to converge with increasing values of the truncation parameter N in the Galerkin expansion (3.26). The value of N used in a particular calculation was selected so that the relative difference in the average concentration values, $\widehat{C}(\tau, -1/2)$, between a N– and a N-2–solution at the time $\tau = 5 \times 10^{-2}$ is no greater than 0.1%. The selected N values depend on the problem parameters (Ra, Le, ϕ) and varies between $N = 21$ and 37.

The ODE system (3.29) was advanced in time using a *RK78* [62] with adaptive time-step. In the most challenging conditions investigated ($Le = 333.33$ and $Ra = 1.5 \times 10^5$) the average time step used in the *RK78* time integrator was about 10^{-6} and the truncation parameter in expansions (3.26) was $N = 37$. Since the flow pattern investigated in the current study has several symmetries the dimension of the problem with $N = 37$ was reduced to $4N_D = 23328$. The worst case scenario resulted in a computational workload of 8.02×10^6 s of CPU time. In less demanding calculations (lower Le values) this maximum workload was reduced down to a value of 3.72×10^3 s ($Le = 1$).

Chapter 4

Results and Discussion

4.1 Efficiency Assessment

The mass transfer efficiency, η, gives a measure of the mixing capability of the system. It is defined as the ratio of the average rate of reaction at the catalytic surface to the maximum value of the average rate of reaction, that is, the one value that would be only attained in the ideal perfect mixing limit,

$$\eta(\tau) = \frac{\text{actual average rate of reaction}}{\text{ideal average rate of reaction}}. \tag{4.1}$$

Hence, if the mixing was perfect, the average concentration on the catalytic surface, $\widehat{C}$ would be the same as the volumetric average concentration $\overline{C}$. Because the rate of reaction is proportional to the concentration in first–order reactions,

$$\eta(\tau) = \frac{\widehat{C}(\tau, Z_{cat.surf.})}{\overline{C}(\tau)} \tag{4.2}$$

where $Z_{cat.surf}$ corresponds to the value of Z where it is placed the catalytic surface. For the cubical geometry $Z_{cat.surf.} = -1/2$ and

$$\widehat{C}(\tau, -1/2) = \int_{-1/2}^{1/2}\int_{-1/2}^{1/2} C(\tau, X, Y, -1/2)\, dX\, dY \tag{4.3}$$

$$\overline{C}(\tau) = \int_{-1/2}^{1/2}\int_{-1/2}^{1/2}\int_{-1/2}^{1/2} C(\tau, X, Y, Z)\, dX\, dY\, dZ \tag{4.4}$$

while for the cylindrical geometry $Z_{cat.surf.} = \pm 1/2$ and

$$\widehat{C}(\tau, \pm 1/2) = 2\pi \int_{\gamma}^{1+\epsilon} C(\tau, R, \pm 1/2)\, R\, dR \tag{4.5}$$

$$\overline{C}(\tau) = 2\pi \int_{-1/2}^{1/2}\int_{\gamma}^{1+\epsilon} C(\tau, R, Z)\, R\, dR\, dZ \tag{4.6}$$

Note that in the ideal limit $\widehat{C}(\tau, Z_{cat.surf.}) = \overline{C}(\tau)$ making the efficiency $\eta = 1$.

The rate equation for convective mass transfer is defined as

$$J_z = \widehat{K}(\tau)\left[C_\infty - \widehat{C}_(\tau, Z_{cat.surf.})\right] \tag{4.7}$$

where J_z is the diffusive flux on the catalytic surface, $\widehat{K}(\tau)$ denotes the surface averaged convective mass transfer coefficient and C_∞ is the typical value of C in the bulk region, far away from the catalytic region, hence

$$k\,\widehat{C}(\tau,-1/2) = \widehat{K}(\tau)\left[C_\infty - \widehat{C}(\tau,-1/2)\right]. \tag{4.8}$$

The Sherwood number is a dimensionless mass transfer coefficient defined as

$$Sh(\tau) = \frac{\widehat{K}(\tau)G}{D} \tag{4.9}$$

where G is a characteristic length, $G = R_2$ for the cylindrical geometry and $G = L$ for the cubical one. Thus, relating (4.8) and (4.9) we got

$$Sh(\tau) = \frac{\phi\,\eta(\tau)}{g[C_\infty/\overline{C}(\tau) - \eta(\tau)]} \approx \frac{\phi\,\eta(\tau)}{g[1-\eta(\tau)]} \tag{4.10}$$

where $g = S$ for the cylindrical geometry and $g = 1$ for the cubical one and where we have considered the concentration in the bulk region approximates to the volumetric average concentration, $C_\infty \approx \overline{C}(\tau)$. In problems where interficial mass transfer is combined with chemical reaction an overall mass transfer coefficient is usually defined as,

$$\frac{1}{Sh_{ov}(\tau)} = \frac{g}{\phi} + \frac{1}{Sh(\tau)} \approx \frac{g}{\phi\,\eta(\tau)}. \tag{4.11}$$

where g has the same meaning as explained above.

Equation (4.11) tells us that if the surface reaction is a slow one (small ϕ), the rate of solute transfer from the bulk region into the disk surface by combined convection plus molecular diffusion will be comparatively fast and values of $\eta(\tau)$ close to one will be attained. In the opposite situation, a fast reaction yielding a large ϕ value, the overall mass transfer process will be basically controlled by the rate of convection plus diffusion thus yielding very low values of $\eta(\tau)$.

Obviously, the question is how to quantify the above qualitative trends, that is, how close to one or zero will be $\eta(\tau)$ when ϕ takes a small or large value, respectively. One of the goals of the present study is to find the relation between the reactor mass transfer efficiency and the parameters of the problem, that is, what is the dependence of η (or Sh) on ϕ, Sc and Ra or Re depending on the reactor studied. Therefore, much attention will be devoted below to the relation between the reactor mass transfer efficiency, the reactor configuration and the parameters of the problem. In particular, if the overall process of solute transfer into the catalytic surface is controlled by molecular diffusion through a boundary layer region then one would expect the Sherwood number to depend on a product of powers of S, Re and Sc or Ra and Sc depending on which reactor we are talking about.

Another quantity that may give an indication of the efficiency is the conversion, defined by

$$\chi(\tau) = \frac{\overline{C}(0) - \overline{C}(\tau)}{\overline{C}(0)} \tag{4.12}$$

which gives account of how much solute has reacted in a determined time. If for a certain conversion, for example, 90%, we wished to predict this time, namely, τ_{90}, i.e., $\chi(\tau_{90}) = 0.9$, we could do it based on the following considerations. If the value of η for any time $\tau > \tau_\infty$

was somehow known and furthermore, was found to be constant, calling it η_∞, it may be shown that it is easy to obtain a good estimate of τ_{90}. In order to do this, the molar balance is performed through the whole reactor volume:

$$\frac{d\overline{C}(\tau)}{d\tau} = G\phi\widehat{C}(\tau, \pm 1/2) \tag{4.13}$$

where $G = 2/S^2$ for the cylindrical reactor and $G = 1$ for the cubical one. Then we introduce the $\eta(\tau)$ definition (4.2) in the above equation to obtain:

$$\frac{d\overline{C}(\tau)}{d\tau} = G\phi\eta(\tau)\overline{C}(\tau) \tag{4.14}$$

The ordinary differential equation (4.14) can be integrated using $(\tau_\infty,\ \overline{C}(\tau_\infty))$ as initial condition:

$$\frac{\overline{C}(\tau)}{\overline{C}(\tau_\infty)} = e^{[-G\phi\eta_\infty(\tau-\tau_\infty)]} \tag{4.15}$$

If we now assume that the transient is short, that is, $\tau_\infty \to 0$ and $\overline{C}(\tau_\infty) \approx \overline{C}(0)$, Eq. (4.15) can be simplified into:

$$-\frac{\overline{C}(\tau)}{\overline{C}(0)} \approx -e^{(-G\phi\eta_\infty\tau)} \tag{4.16}$$

Thus the evolution in time of the reactor conversion, $\chi(\tau)$, can be approximated by

$$\chi(\tau) = \frac{\overline{C}(0) - \overline{C}(\tau)}{\overline{C}(0)} \approx 1 - e^{(-G\phi\eta_\infty\tau)} \tag{4.17}$$

Assuming that the values of η_∞ are previously known, the values of τ_{90} can be therefore estimated as:

$$\tilde{\tau}_{90} = -\frac{\log(0.1)}{G\phi\eta_\infty} \tag{4.18}$$

Note that as long as the efficiency, η, has reached a constant value, we could find the time in which any conversion, χ^*, is achieved, as

$$\tilde{\tau}_{\chi^*} = -\frac{\log(1-\chi^*)}{G\phi\eta_\infty}. \tag{4.19}$$

We define also the following quantities that will be useful for analyzing the results obtained. The normalized concentration, for a given position $\mathbf{s}$, is defined as

$$\Sigma(\tau, \mathbf{s}) = \frac{C(\tau, \mathbf{s})}{\overline{C}(\tau)} \tag{4.20}$$

where $\mathbf{s} = (R, Z)$ for the cylindrical geometry and $\mathbf{s} = (X, Y, Z)$ for the cubical one. The normalized radially (horizontally) averaged concentration for the cylindrical (cubical) geometry is given by,

$$\Lambda(\tau, Z) = \frac{\widehat{C}(\tau, Z) - \widehat{C}(\tau, -1/2)}{\overline{C}(\tau) - \widehat{C}(\tau, -1/2)}, \tag{4.21}$$

and the normalized radially (horizontally) averaged vertical solute flux for the cylindrical (cubical) geometry is,

$$\Gamma(\tau, Z) = \frac{\dfrac{\partial \widehat{C}(\tau, Z)}{\partial Z}}{\phi \widehat{C}(\tau, -1/2)} \tag{4.22}$$

4.2 Forced convection problem

In this part of the work four different values of the Schmidt number, namely Sc =1,10,100 and 1000, and several values of the Damköhler number within the range $1 \leqslant \phi \leqslant 8000$ were considered. Note that values of $Sc \approx 1$ would typically be found in a gas–phase reactor at atmospheric pressure while the largest $Sc = 1000$ value is typical of a liquid phase reactor. For each particular combination of Sc and ϕ calculations were performed at several values of Re and S, as is explained in what follows. A unique value of the radius ratio, $\gamma = 0.5$, was used in all of the present calculations.

4.2.1 Velocity Field

Velocity fields were calculated at four different values of the height to radius aspect ratio, namely $S = 0.125$, 0.25, 0.50 and 1, and four different values of the Reynolds number, namely $Re \times 10^{-3} = 1$, 5, 10 and 20. In addition, for the particular $S = 0.25$ value calculations were extended up to a Reynolds number of $Re = 10^5$. Figure 4.1 shows the flow streamlines (isolines of the streamfunction Ψ) calculated at $Re = 2 \times 10^4$ and two different aspect ratios, $S = 0.125$ and 0.25. The velocity fields plotted in these two figures are symmetric with re-

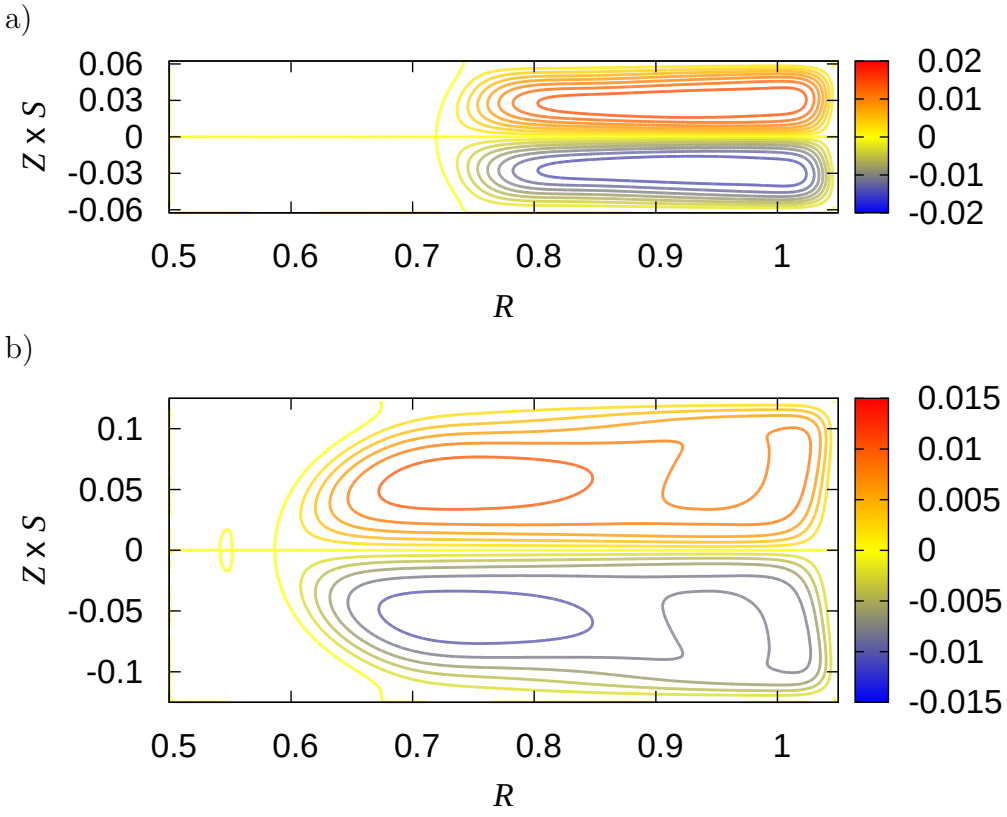

Figure 4.1: Flow streamlines for $Re = 2 \times 10^4$ and two different values of the height to radius aspect ratio, $S = 0.125$ (a) and $S = 0.25$ (b).

spect to the horizontal midplane ($Z = 0$). Although this feature may seem quite natural, the existence of solution branches with symmetry–breaking has also been reported [28, 30, 38]. The present numerical method allows the calculation of such symmetry-breaking solutions, as both even and odd functions along the Z direction were used in expansions (3.8) and (3.9). Notwithstanding, only symmetric solutions were detected in all of the cases investigated. As a consequence, only Chebyshev polynomials of even degree were considered along the Z direction in the concentration expansion (3.11). Therefore, $\widehat{C}(\tau)$ and $\eta(\tau)$ in (4.2) can be indistinctly calculated either at $Z = -1/2$ or $Z = 1/2$.

Figure 4.1 shows the cross-stream, secondary motion that is typical of the flow between a pair of corotating disks. In the vicinity of both disk surfaces fluid is moving outwards along the boundary layer region known as Ekman layer. It should be kept in mind that, as illustrated in Fig. 3.4b, the main motion occurs in the circumferential direction, that is, it would be normal to the paper in Fig. 4.1. The secondary motion is basically driven by the imbalance between the inwards directed radial pressure force and the outward directed centrifugal force along the disk Ekman layers (see, for example, the theoretical analysis in Ref. [76] and the references therein). Moreover, as shown in Fig. 3.4b, the radial region around $R = 1$ is characterized by very high shear levels as the circumferential velocity, V, must drop to its minimum $V = -1$ value at the outer enclosure wall.

As can be seen in Figs. 3.4 and 4.1, when the aspect ratio S is low the cross-stream vortices do not reach the vicinity of the rotating hub as there is an inner core region where fluid is nearly in solid-body rotation with the disks and hub, that is, $V \approx 0$, with cross-stream motion much weaker than the one in the outer region. Let $R_{sep} = R_{sep}(Re, S)$ be the radial location where the separation between the Ekman layer region and the inner core is observed at the disk surface. In the case with $S = 0.125$, which is the most unfavorable in terms of effective catalyst surface, we have $R_{sep} = 0.73$ in Fig. 4.1a and therefore the Ekman layer region ($R > R_{sep}$) extends over about 2/3 of the total disk surface. The R_{sep} location decreases with increasing S down to the point that at $S = 1$ (results not shown here) there is no inner core.

According to theory, the thickness of the Ekman layer, δ_E, should be proportional to $\sqrt{\nu\Omega}$ and thus $\delta_E/H \propto Re^{-1/2}S^{-1}$. For each of the present calculations, an averaged value of the Ekman layer thickness, $\widehat{\delta}_E$, was estimated as follows. We first averaged the radial component of velocity, $U(R, Z)$, within the radial region with $R_{sep} \leqslant R \leqslant 1$ to obtain the axial profiles $\widehat{U}(Z)$. Figure 4.2 shows the $\widehat{U}(Z)$ profiles obtained for two different aspect ratios, $S = 0.125$ and 0.50. In almost all of the cases $\widehat{U}$ raises quickly from the zero value at the disk surface up to a maximum value and then it drops down to a negative minimum value at the $Z = 0$ midplane (where the strongest inwards cross-stream flow is observed in Figs. 4.1). A straightforward estimate of $\widehat{\delta}_E/H$ is therefore obtained by measuring the axial distance between the maximum location and the disk surface. The profile for $Re = 1000$ in Fig. 4.2a is obviously anomalous. It appears that at the lowest Re value considered the Ekman layers are not well developed yet.

A fit of the estimated $\widehat{\delta}_E/H$ values in the form,

$$\log\left(\frac{\widehat{\delta}_E}{H}\right) = a + b\log(S) + c\log(Re) \tag{4.23}$$

yielded $a = 0.112 \pm 0.160$, $b = -1.020 \pm 0.0382$, $c = -0.517 \pm 0.0176$. Thus, we have

a)

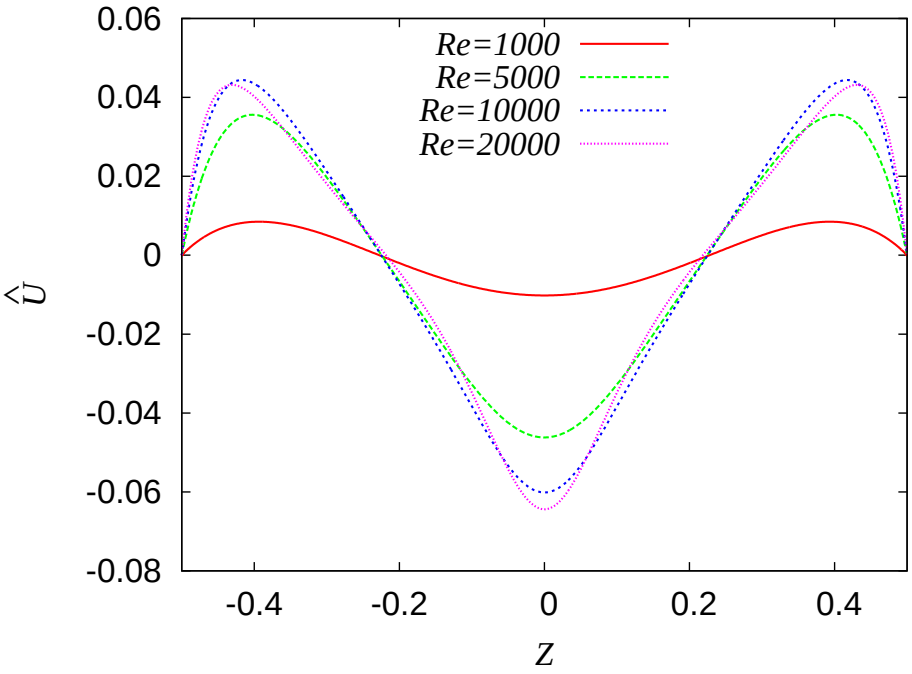

b)

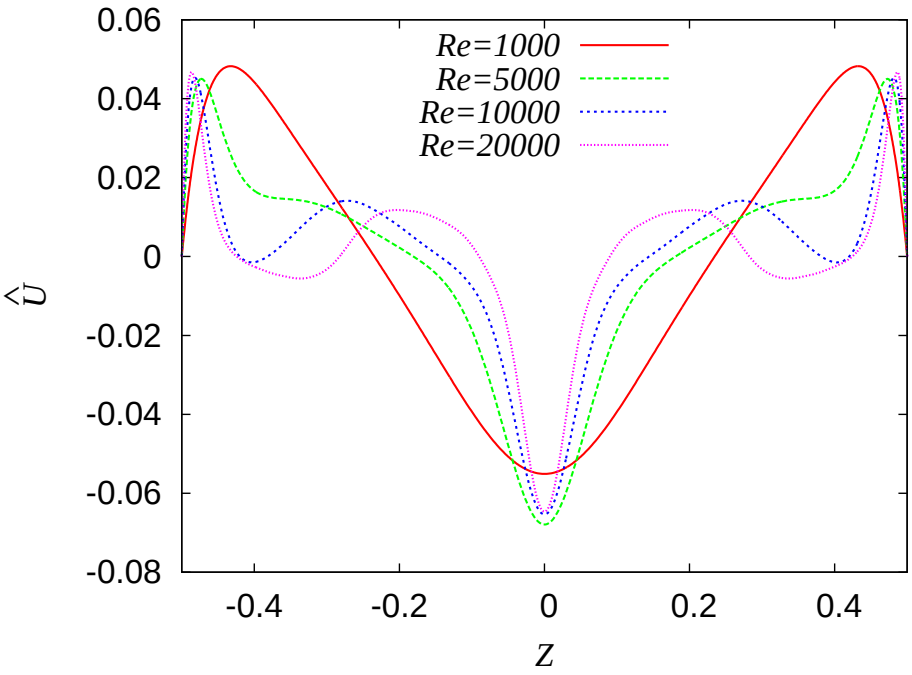

Figure 4.2: Axial profiles of the radially averaged radial component of velocity, $\widehat{U}(Z)$, for four different values of the Reynolds number in the range $10^3 \leqslant Re \leqslant 2 \times 10^4$ and two different values of the height to radius aspect ratio, $S = 0.125$ (a) and $S = 0.5$ (b).

$\widehat{\delta}_E/H = 1.19\, S^{-1.02}\, Re^{-0.517}$, in good agreement with theory. The anomalous data point at $Re = 1000$ and $S = 0.125$ was not included in the fit.

4.2.2 Discontinuous operation

In the discontinuous reactor model it is assumed that initially ($\tau = 0$) the solute is perfectly well-mixed through all of the volume with an arbitrary concentration level equal to one. In fact, since the strict initial condition $C(0, R, Z) = 1$ would be incompatible with the boundary condition at the disk surface, Eq. (2.17), the concentration field was initialized using the same method as in Subsection 3.3.3. That is, a one-dimensional solution of (2.16)–(2.19) in the limiting no convection case, $Re = 0$, at a very short integration time, $\tau_0 = 0.001$, is extended radially to obtain the two-dimensional field $C(0, R, Z)$. Since in the discontinuous mode no reactant is fed during operation, i.e., $J_R = 0$ in the boundary condition (2.19), the reactant conversion $\chi(\tau)$ will be continuously growing. In each particular run, the ODE system (3.12) was advanced in time until a conversion level of $\chi = 0.90$ was reached.

Influence of the height to radius aspect ratio

Let us imagine that a particular reactor setup with a unique pair of corotating disks and certain values of the outer radius R_2 and the height H does already exist. The volume of such a reactor would be equal to $\pi\,(R_2^2 - R_1^2)\,H$. Let us further imagine that for some practical reason we need to double the reactor volume. One obvious way of doing so would be to simply double the height H. A second way would be to add a third disk on top of the second, with the vertical distance between the second and third disks set to the same H value. The second method would be obviously more expensive but has the advantage of maintaining the same ratio of catalyst surface to reactor volume, that is, $a_g = 2/H$. Which of the two methods ought to be preferred in practice to increase the reactor volume? There is no evident answer and we intend that the results and analytical tools presented in what follows may be helpful whenever a choice between the two methods has to be made. In particular, we will focus in the analysis of the reactor mass transfer efficiency and the time needed to reach a given conversion level.

Four different values of the height to radius aspect ratio, namely $S = 0.125$, 0.25, 0.5 and 1.0, and four values of the Reynolds number, $Re \times 10^3 = 1, 5, 10$ and 20 were considered. Once the velocity fields were obtained for each of the 16 (Re, S) pairs, in each case four values of Sc and four values of ϕ were considered thus giving a total of 256 calculations. Note that since the Damköhler number, $\phi = kH/D$, is defined on the basis of H, in order to assess the effect of an increase in height alone, keeping the same values for k and D, the value of ϕ must be changed along with the value of S. That is, if at $S = 0.125$ we set a given ϕ value then at the corresponding calculation at $S = 0.25$ we set $2\phi_0$, and so on.

Figure 4.3a shows the evolution in time of the reactor efficiency, η, for all of the four values of S investigated when the rest of parameters are fixed to $Re = 10^4$, $Sc = 1$ and $\phi_0 = 1$. As expected, since the specific catalyst surface, $a_g = 2/H$, decreases with increasing S the time τ_{90} needed to achieve the target conversion also increases. There is also a slight drop in the efficiency levels with increasing S but, as will be seen below, such a behavior cannot be generalized to other conditions. One interesting result, is that after a relatively short transient $\eta(\tau)$ reaches a plateau–like, constant value. In all of the cases, $\eta(\tau)$ achieves a maximum value during the transient and then experiences a considerable drop until it reaches the final asymptotic value. Notice these characteristics are those described in Sub-

a)

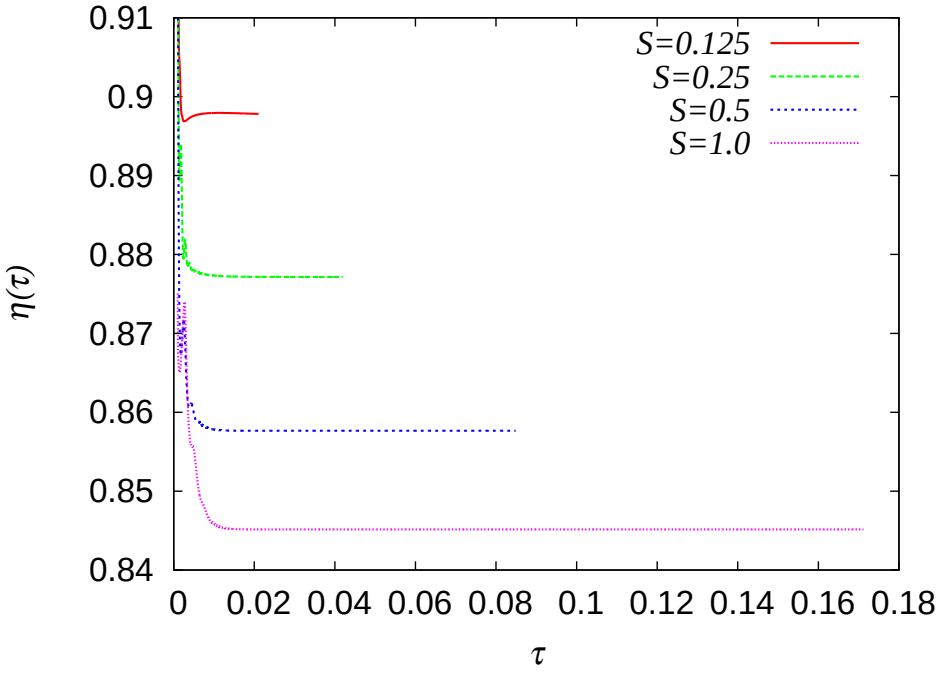

b)

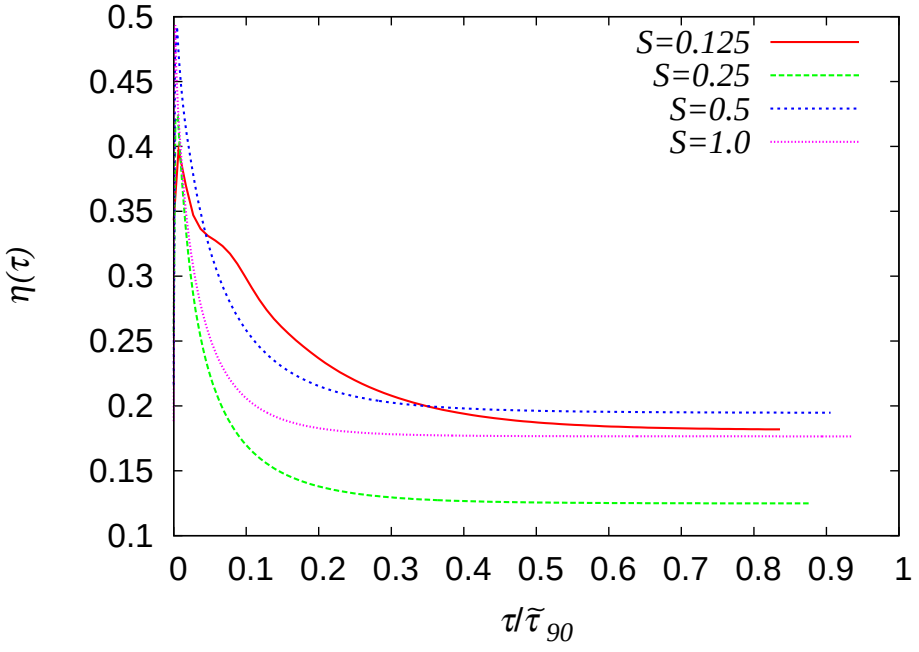

Figure 4.3: Evolution in time of the reactor efficiency, $\eta(\tau)$, for two specific cases with a) $Re = 1 \times 10^4$, $Sc = 1$ and $\phi_0 = 1$, and b) $Re = 2 \times 10^4$, $Sc = 1000$ and $\phi_0 = 100$. Note that in the latter plot (b) the normalized time $\tau/\tilde{\tau}_{90}$ is used in the abscissa.

section 4.1, so that τ_{90} value can be predicted using (4.18), where η_∞ will be the asymptotic value mentioned. Figure 4.4 shows a comparison between the $\tilde{\tau}_{90}$ estimates and the τ_{90} values obtained in the calculations. In general, Eq. (4.18) produces a good estimate of τ_{90} with the

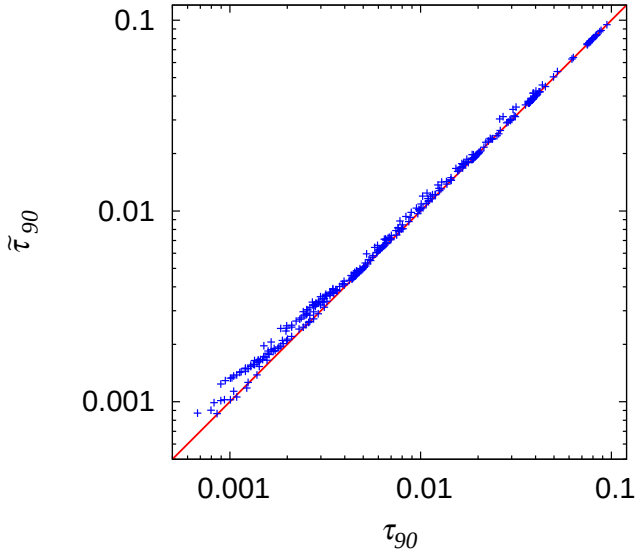

Figure 4.4: The values of τ_{90} predicted by Eq. (4.18), $\tilde{\tau}_{90}$, are plotted against the corresponding τ_{90} values obtained in all of the calculations for the discontinuous reactor configuration.

largest departures observed for the smallest reaction times (small S and/or large ϕ values), that is, in those cases where the ratio τ_∞/τ_{90} is not small enough so that the approximation (4.16) differs most from the exact solution of Eq. (4.15).

Obviously, in order to calculate a $\tilde{\tau}_{90}$ value we need to know first what is the asymptotic efficiency of the reactor, η_∞. The dependence of η_∞ on the flow parameters will be discussed in the following sections. Before that, let us further analyze some qualitative aspects. When the surface reaction is slow, η_∞ is close to one and then Eq. (4.18) consistently shows that the overall mass transfer process is controlled by the rate of reaction as basically $\tilde{\tau}_{90} \propto 1/\phi$. On the opposite situation of a very fast reaction, large ϕ values, it is convenient to use an alternative equation based on the Sherwood number. Let Sh_∞ be the quantity obtained from Eq. (4.10) for $\tau \geqslant \tau_\infty$ and let us combine equations (4.10) and (4.18):

$$\tilde{\tau}_{90} = -\frac{S\log(0.1)}{Sh_\infty\,(1-\eta_\infty)} \tag{4.24}$$

The point is that if Sh_∞ is roughly independent of ϕ then Eq. (4.24) reflects that when the reaction is fast enough the overall mass transfer is controlled by the rate of combined convection plus diffusion mass transfer. That is, we have the situation where η_∞ will be close to zero (low concentration levels at the disk surface) and therefore, for a given S, $\tilde{\tau}_{90} \propto 1/Sh_\infty$. For example, in the present calculations with $\phi_0 = 0.125\,\phi/S = 1000$ the calculated values of η_∞ are typically one order of magnitude smaller than the corresponding values for $\phi_0 = 100$. Notwithstanding, in almost all of the cases the latter value is already small to the point that τ_{90} decreases very slightly between $\phi_0 = 100$ and 1000, as predicted by (4.24). Another obvious consequence, in view of Eq. (4.10), is that when ϕ is large we would expect, for fixed values of S, Re and Sc, a $\eta_\infty \propto 1/\phi$ dependence.

It is found that the normalized solute concentration Σ, defined in (4.20) becomes independent of time for $\tau \geqslant \tau_\infty$, that is, we can define $\Sigma_\infty(R,Z) = \Sigma(\tau,R,Z) : \tau \geqslant \tau_\infty$. Figures 4.5 and 4.6 show respectively the contours of $\Sigma_\infty(R,Z)$ obtained for $S = 0.125$ and $S = 0.25$ at $Re = 2 \times 10^4$ and three different values of the Schmidt number, namely $Sc = 1$, 10 and 1000. When the reaction is comparatively fast, $\phi_0 = 100$ (plots d), e) and f) in

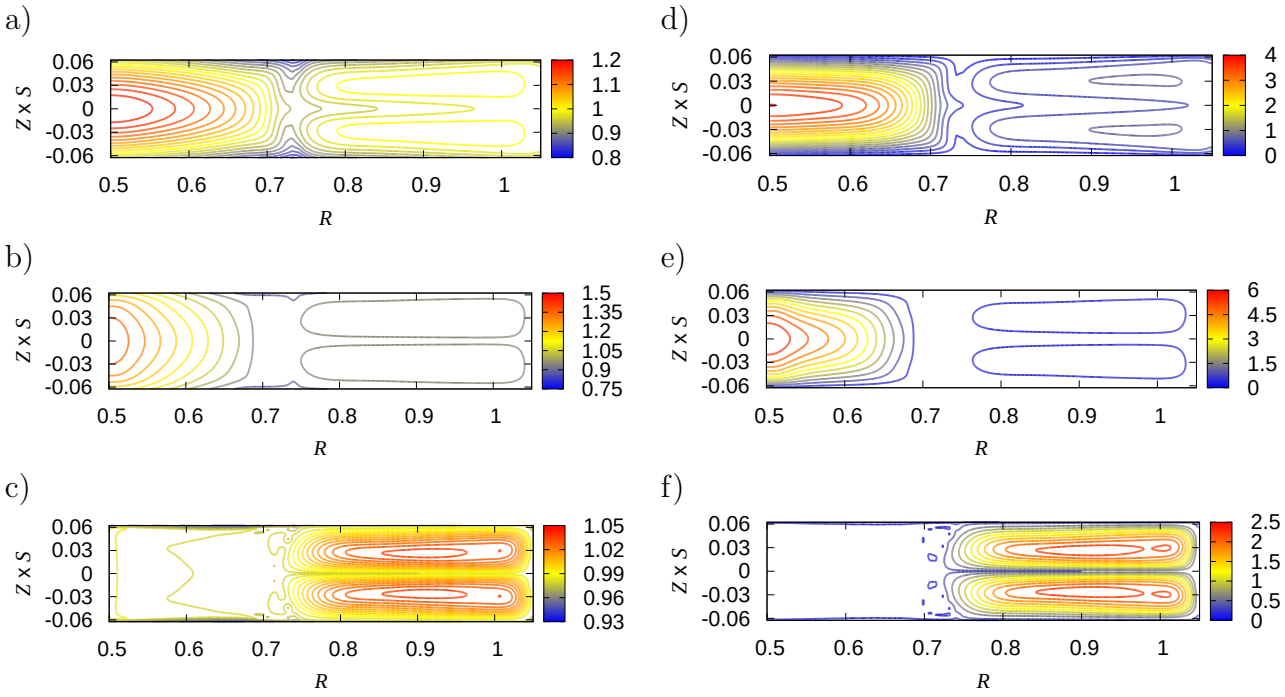

Figure 4.5: Contours of the normalized concentration, Σ_∞, for $S = 0.125$ and $Re = 2 \times 10^4$ in the discontinuous reactor. The values of the Damköhler number are $\phi = 1$ in plots a), b) and c) and $\phi = 100$ in plots d), e) and f). The values of the Schmidt number are $Sc = 1$ in plots a) and d), $Sc = 10$ in plots b) and e) and $Sc = 1000$ in plots c) and f).

both figures), we see that the minimum levels of Σ_∞ are close to zero. Since the smallest concentration values are always found at the disk surface, $\Sigma_\infty \to 0$ means, on account of (4.2), that the reactor efficiency will be small. On the contrary, the largest levels of Σ_∞ are always found in the bulk region. Note that the larger the maximum level of Σ_∞, the larger the contribution of convection plus diffusion to the overall mass transfer resistance. This is why in all six cases with faster reaction ($\phi_0 = 100$) the maximum concentration values are much higher. At $Sc = 1$ (plots a) and d) in Figs. 4.5 and 4.6) when characteristic times of mass convection and molecular diffusion coincide, regions with largest concentration occur within the inner core region, $R < R_{sep}$. This is due to the fact that convection in the inner core is much weaker than in the region occupied by the pair of counter-rotating secondary vortices. The concentration contours at $Sc = 1000$, plots c) and f), are however somewhat intriguing at first sight. The maximum Σ_∞ values are not found in the inner core anymore but in the center of the secondary vortices. That is, it appears that solute remains trapped within a sort of bubble as it cannot easily reach the Ekman layer region.

On the other hand, if the overall mass transfer process from the bulk region into the disk surface is to be controlled by molecular diffusion in the vicinity of the disks, i.e., within the Ekman layers, then one would expect a dependence of the form $Sh \propto Re^{1/2}Sc^{1/3}$ [77] for the Sherwood number defined in (4.10). Such a behavior is consistent with the notion, discussed above, that the Ekman layer thickness, δ_E, is independent of S so that the strength

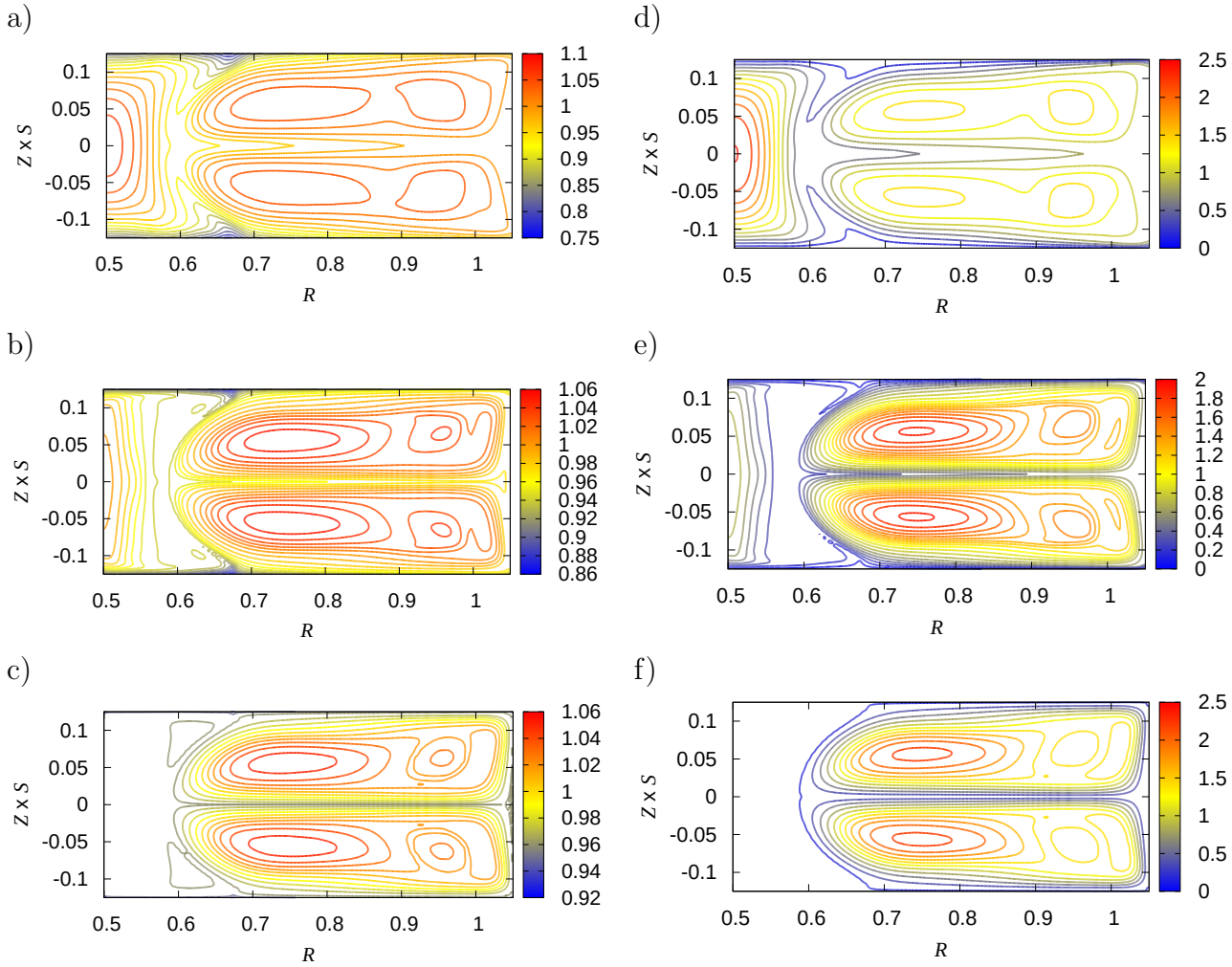

Figure 4.6: Contours of the normalized concentration, Σ_∞, for $S = 0.25$ and $Re = 2\times10^4$ in the discontinuous reactor. The values of the Damköhler number are $\phi = 2$ in plots a), b) and c) and $\phi = 200$ in plots d), e) and f). The values of the Schmidt number are $Sc = 1$ in plots a) and d), $Sc = 10$ in plots b) and e) and $Sc = 1000$ in plots c) and f).

of the secondary motion in the Ekman layer should be proportional to ΩR_2 (see Fig. 4.1). Then, since we are considering constant values of the ϕ/S ratio it follows from (4.10) that η_∞ should be roughly independent of the aspect ratio S. Present results with $Sc = 1$ are in fairly good agreement with the expected theoretical behavior, as illustrated in the case with $Re = 10^4$ and $Sc = 1$ in Fig. 4.3a where the maximum variation of η_∞ with S is within 6%. However, departures from the theoretical behavior become increasingly significant with increasing values of ϕ and, especially, of Sc. Figure 4.3b shows time evolutions of $\eta(t)$ for all the four values of S when the rest of parameters take the value $Re = 2 \times 10^4$, $Sc = 1000$ and $\phi_0 = 100$. Note that in this plot the time in the abscissa is scaled in each case with the $\tilde{\tau}_{90}$ value predicted by (4.18). Because of the high value of ϕ used in these calculations the initial transients are not negligible, that is, τ_∞/τ_{90} is significantly larger than zero. Note that while the η_∞ values for $S = 0.125, 0.5$ and 1 are around 0.18 the corresponding value for $S = 0.25$ is anomalously smaller by about a 30%.

In view of the concentration contours in Figs. 4.5 and 4.6 one plausible explanation for such an unexpected dependence of η_∞ on S might be that the catalyst surface in the inner core, $R < R_{sep}$, is not effective because of the weak cross-stream circulation. Then a higher R_{sep} value would imply a higher contribution of the less effective inner core area into the definite integral of the numerator of Eq. (4.2). Notwithstanding, Fig. 4.7 shows that the relative size of the inner core only has a slight effect on the surface-averaged value η_∞. This

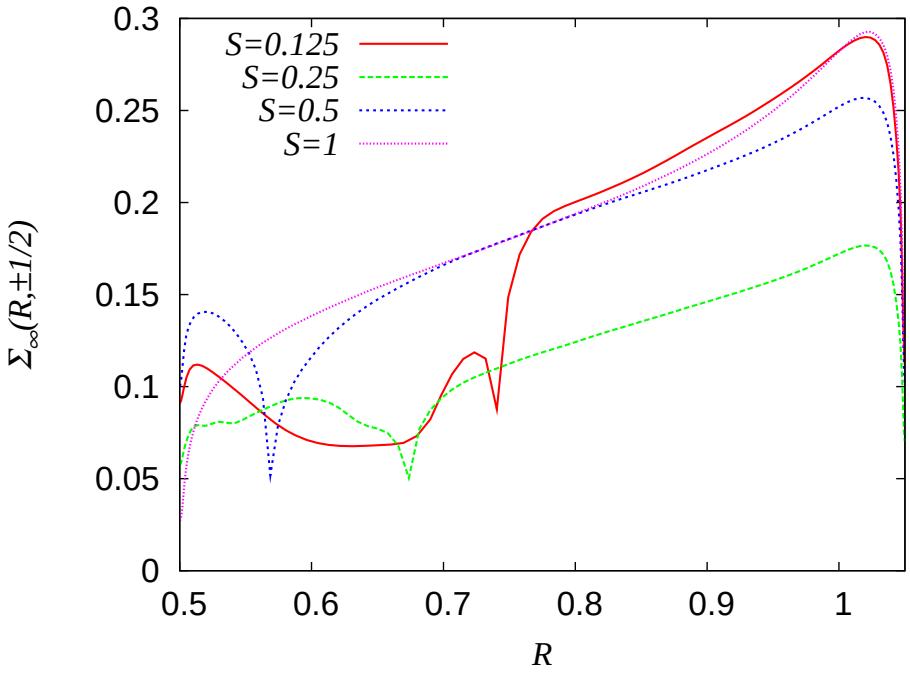

Figure 4.7: Radial profiles of the normalized concentration at the disk surface, $\Sigma_\infty(R, \pm 1/2)$, for all the four aspect ratios investigated in the discontinuous reactor and the same conditions as in Fig. 4.3b), i.e., $Re = 2 \times 10^4$, $Sc = 1000$ and $\phi_0 = 100$.

plot shows the radial profiles of $\Sigma_\infty(R, \pm 1/2)$ for the case with $Re = 2 \times 10^4$, $Sc = 1000$ and $\phi_0 = 100$ for each value of S (that is, the same conditions as in Fig. 4.3b). In all of the profiles the maximum Σ_∞ value is found near the enclosure wall, $R \approx 1.02$, basically at the location where the cross-stream vortices detach from the disk surface and the shear stress attains its maximum levels. In the less efficient case with $S = 0.25$ we see that the maximum value, $\Sigma_\infty \approx 0.18$, is considerably lower and this deficit is maintained in the region with $R \geqslant 0.75$. Except for the case with the largest aspect ratio, $S = 1$, the R_{sep} location

is marked by a local minimum in the radial profile of Σ_∞. In all of the cases we see that the concentration values at the disk surface are smaller but not negligible in the inner core region, $R \leqslant R_{sep}$. In summary, Fig. 4.7 suggests that the lower η_∞ value for the case with $S = 0.25$ in Fig.4.3b is basically due to the relative inability of the flow field, compared to the ones for the other aspect ratios, to transport reactant from the bulk region into the vicinity of the disk surface.

The variations of η_∞ with S are to be therefore attributed to the existence of bulk regions with high concentration levels, as seen in Figs. 4.5 and 4.6. That is, large amount of solute accumulates within the bulk region far from the disk surface. A higher Sc value means a lower molecular diffusivity so that the solute is having more difficulty to reach the catalytic surface. The mass transfer resistance concentrates not only in the vicinity of the disk surface but there is also a significant contribution to the overall resistance associated to the transport of solute from the bulk region into the Ekman layer. This phenomenon will be further analyzed in the next sections. As there appears to be no systematic dependence of η_∞ on S, we will focus hereinafter on a single value of the height to radius aspect ratio. In particular, the value $S = 0.25$ is selected because, as illustrated in Fig. 4.3b, is the one typically showing higher relative levels of mass transfer resistance. Moreover, calculations for $S = 0.25$ were extended to higher Reynolds numbers up to $Re = 10^5$ in order to characterize better the Re dependence while ruling out the low-Re effects that were detected in some calculations with the lowest $Re = 1000$ value.

Performance Analysis

For the chosen $S = 0.25$ aspect ratio additional calculations were performed for Reynolds numbers between $Re = 4 \times 10^4$ and $Re = 1 \times 10^5$ every 10^4 units. Our purpose here is to assess to what extent the transport of reactant into the catalyst surface is controlled by the rate of mass transfer within the disk boundary layer and, if possible, to correlate the mass transfer efficiency as a function of the flow parameters, Re, Sc and ϕ. At a qualitative level, it is observed that all of the calculated η_∞ values increase with increasing Re and Sc and decrease with increasing ϕ. In terms of Sherwood number, however, it is not clear at first sight whether or not there is some dependence of Sh_∞ on ϕ. The idea is to use the radially averaged concentration profiles to quantify the thickness of the concentration boundary layer, δ_C/H. Then a dependence of δ_C/H on the flow parameters would be looked for to finally search for a dependence of η_∞ on δ_C/H. Note that such a procedure is equivalent, on account of (4.10), to directly obtain a fit of the type $Sh_\infty = Sh_\infty(Re, Sc, \phi)$ but it has the advantage that the hypothesis $Sh_\infty \propto H/\delta_C$ is also tested along the way.

In the present problem, it appears that such a methodology is only suitable when the radially averaged concentration profiles are similar to the one in Figure 4.8a, corresponding to $Re = 10^4$, $Sc = 1$ and $\phi = 2$. The quantity plotted in this figure is in fact the normalized radially averaged concentration, Λ, defined in (4.21), for $\tau = \tau_\infty$. Contrary to what was previously found for the Ekman layer thickness in Fig.4.1, it is not straightforward how to define δ_C from the axial concentration profiles. In Fig.4.8a we see that Λ is continuously growing between the reference zero value at the disk surface and the maximum value attained at $Z = \pm 0.17$. Note that the maximum Z–location is basically the axial location of the center of the cross-stream vortices, as previously seen in the concentration contours of Figs. 4.5 and 4.6. We may base on the estimation not of δ_C/H itself but of a different quantity, ε/H, which provided a good measure of δ_C/H. Figure 4.8a also includes the normalized radially averaged vertical diffusion flux, Γ, defined in (4.22) for $\tau = \tau_\infty$. Note that $\Gamma(\tau_\infty, \pm 1/2) = 1$

a)

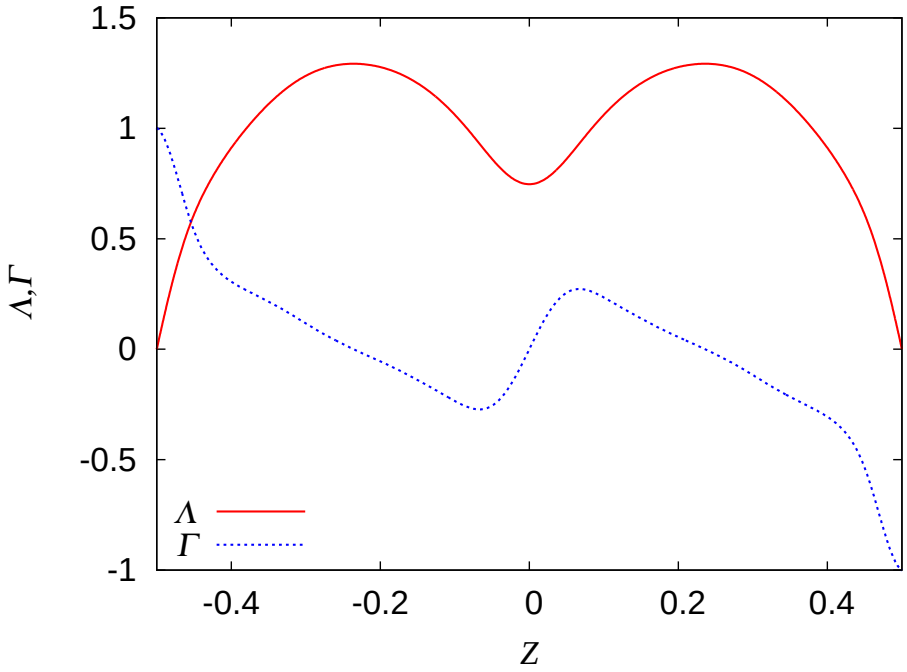

b)

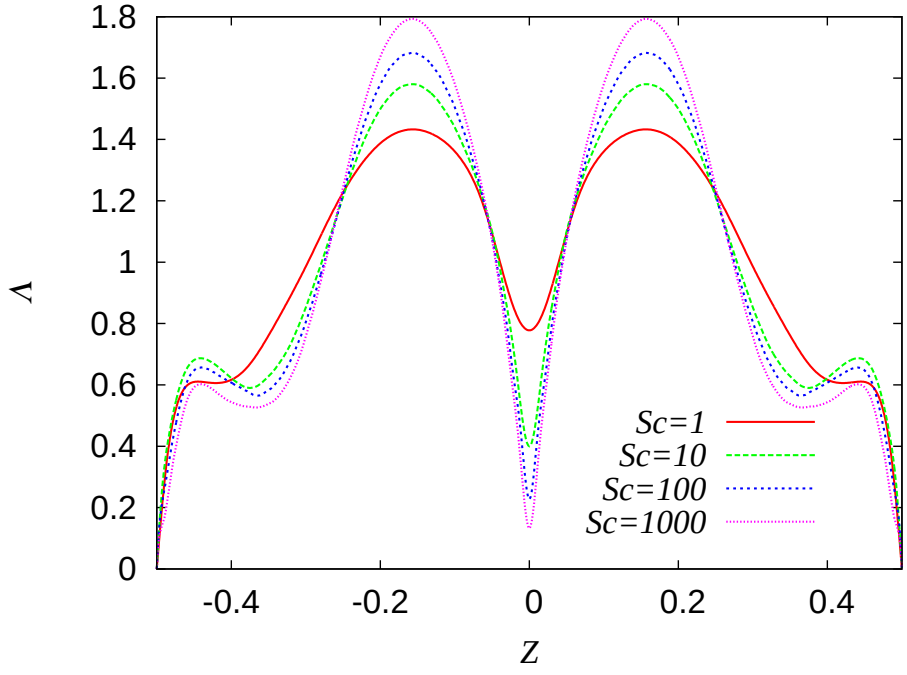

Figure 4.8: a) Axial profiles of the radially averaged normalized concentration, $\Lambda(\tau_\infty, Z)$, and the normalized molar flux, $\Gamma(\tau_\infty, Z)$, respectively defined by Eqs. (4.21) and (4.22), for $Re = 1 \times 10^4$, $Sc = 1$ and $\phi = 2$. b) Axial profiles of $\Lambda(\tau_\infty, Z)$ for $Re = 6 \times 10^4$, $\phi = 2000$ and all of the four values of the Schmidt number investigated.

because of boundary condition (2.13). The value of ε/H is taken as $0.5 + Z_c$, where Z_c is the axial location where the profiles of Γ and Λ cross each other. The calculated ε values for $Re \geqslant 10^4$ were successfully fitted to $\varepsilon/H = ARe^b\phi^c$ only when $Sc = 1$ or 10. In both cases the exponent b was very close to $-1/2$ and c was positive but close to zero. Notwithstanding, at $Sc = 100$ and, especially, 1000 a strong correlation was detected between the b and c exponents and the fits were not statistically meaningful. Moreover, there was no significant fit for the $Sh_\infty \propto R_2/\varepsilon$, even for $Sc \leqslant 10$. The reasons for such a departure from the expected theoretical behavior can be understood when inspecting Λ profiles such as those in Fig. 4.8b, corresponding to $Re = 6 \times 10^4$ and $\phi = 2000$. In particular, it is noteworthy that:

- For all four values of the Schmidt number, the concentration profile has a first local maximum of about $\Lambda(\tau_\infty, Z) = 0.6 - 0.7$ not far from the disk surface ($Z < -0.4$).
- This local maximum is much lower than the global maxima observed in the bulk region, around $Z = \pm 0.17$; the value of Λ at the global maxima significantly increases with increasing Sc.
- The location of the first local maximum near the disk surface, $Z \approx -0.43$, is roughly independent of Sc, in disagreement with the $\delta_C/R_2 \propto Sc^{-1/3}$ expectation.
- After the first local maximum, the drop in Λ is small. Even though, this drop implies that, on the average, there is no direct solute transport by molecular diffusion between the bulk region and the disk Ekman layer regions.
- The value of Λ at the local minimum at $Z = 0$ decreases with increasing Sc. The Λ drop between the global maxima and the local minimum raises from about $\Delta\Lambda = 0.6$ units at $Sc = 1$ up to some $\Delta\Lambda = 1.7$ units for $Sc = 1000$.
- This $\Delta\Lambda$ drop is in all cases equal or larger than the Λ drop between the first local maximum and the $\Lambda = 0$ value at the disk surface.

In summary, we see that as molecular diffusion becomes slower a relatively larger amount of solute accumulates in the bulk region. Since transport by molecular diffusion between the bulk region and the disk Ekman layers does not seem to work solute is instead diffused into the midplane region where fluid is returned inwards (see Fig. 4.1). Thus, as the Schmidt number increases, the overall solute transfer rate is increasingly controlled by the rate of molecular diffusion transfer between the bulk region and the midplane ($Z = 0$) region.

It is therefore not surprising than a fit of the form

$$\log Sh_\infty = a + b\log(S) + c\log(Re) + d\log(Sc) + e\log(\phi) \tag{4.25}$$

does not really work. As shown in Fig. 4.9a, this fit ($a = 0.681 \pm 0.1012$, $b = -0.0792 \pm 0.0168$, $c = 0.37295 \pm 0.0100$, $d = 0.137 \pm 0.00394$ and $e = -0.0346558 \pm 0.00394$) is not very good with relative departures between calculated and fitted Sh_∞ values as large as 35%. Moreover, the comparison of present results with the theoretical dependence [77]

$$Sh = 0.62Re^{1/2}Sc^{1/3} \tag{4.26}$$

shown in Fig. 4.9b, reveals that mass transfer efficiency in the present discontinuous reactor is much lower than it would be for the boundary layer flow over a free rotating disk. Note that the d coefficient obtained in the fit (4.25) is anomalously below the theoretical 1/3 value. Thus, it is not surprising that the low efficiency of the current discontinuous setup

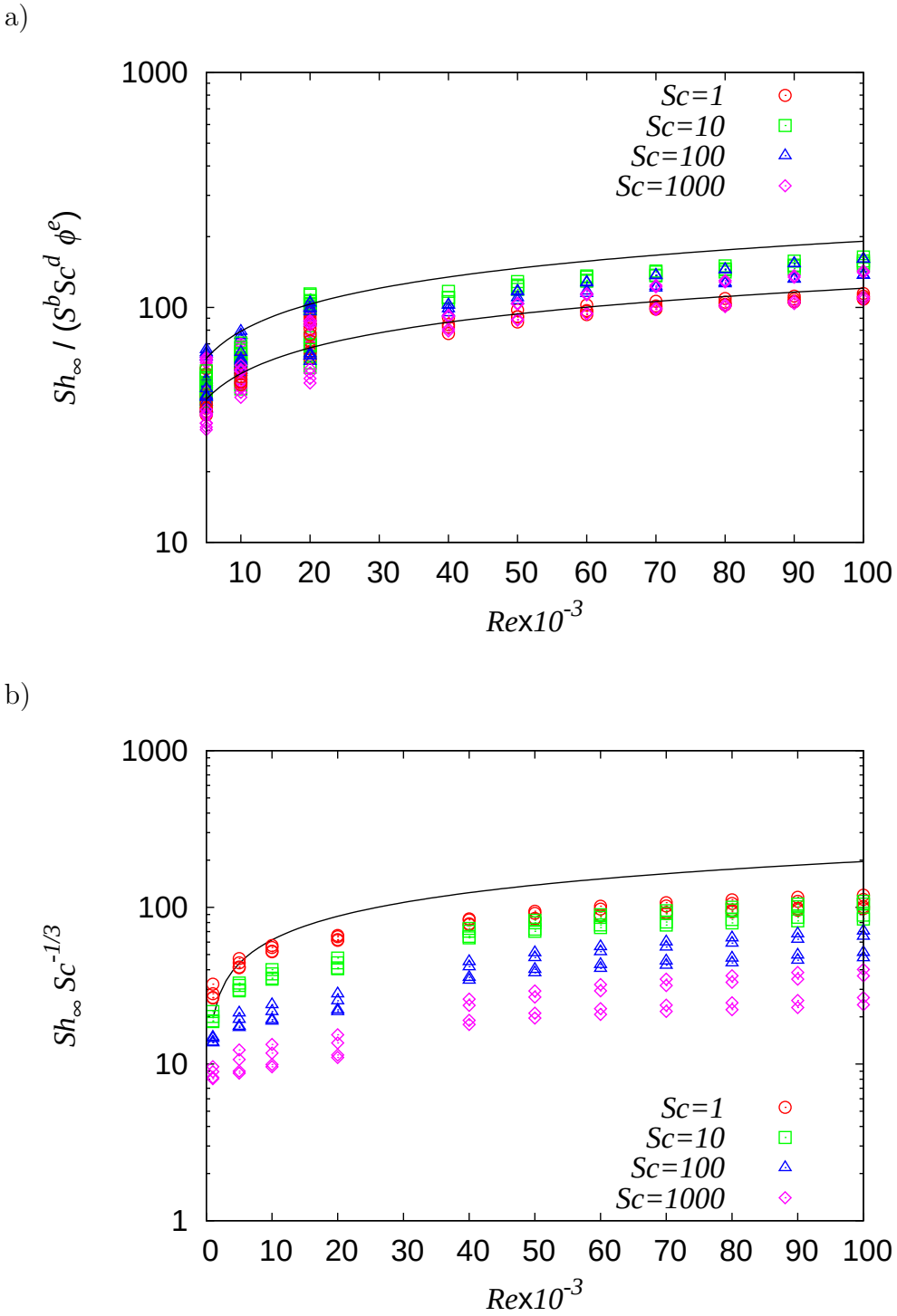

Figure 4.9: Variation with Re of the predicted values of the Sherwood number, Sh_∞, for all of the calculations for the discontinuous reactor configuration. In a), Sh_∞ is divided by $S^b Sc^d \phi^e$, where b, d and e denote the corresponding exponents obtained in the fit (4.25); the two solid lines denote the boundaries of the 95% confidence interval for the fit. In b), Sh_∞ is divided by $Sc^{1/3}$ instead and the theoretical boundary–layer prediction, Eq. (4.26), is plotted with a solid line. In both plots, circles, squares, triangles and diamonds respectively denote the results obtained with $Sc = 1$, 10, 100 and 1000.

gets increasingly evident in Fig. 4.9b as the Schmidt number increases. This fact confirms the interpretation of Fig. 4.8b given above, i.e., the overall mass transfer is not boundary layer–controlled as most of the resistance is probably due to the transfer of solute from the bulk region into the disk Ekman layer.

4.2.3 Semicontinuous operation

In the rotating disk reactor investigated by Meeuwse et al. [25] these authors reported, for $Re \approx 10^5$, a value of the Sherwood number roughly in agreement with the theoretical value given by Eq. (4.26). Why should our corotating disk setup be less efficient than Meeuwse et al.'s? In our configuration there are two corotating disks while Meeuwse et al.'s apparatus consisted of one rotating and one stationary disk. It appears that, for a fixed reactor volume, two corotating disks would induce a cross-stream flow at least as strong as the one produced in the rotor-stator configuration. Probably, the difference in terms of mass transfer efficiency is related to the fact that Meeuwse et al.'s reactor operated in continuous mode as a stream of fresh reactant was fed through the gap between the rotating disk and the external enclosure wall.

Although the inclusion of such a feed stream in the corotating disk setup is beyond the scope of the present investigation it is possible to modify the current model to incorporate a continuous reactant feed, as sketched in Fig. 2.2. In the semicontinuous reactor model a constant molar flux of reactant is fed through the external enclosure wall, which we therefore assume is made of some porous material. In particular, boundary condition (2.15) is used with a molar flux profile having a Gaussian shape, $J_R(Z) = B \exp(Z^2/\sigma^2)$ with $\sigma^2 = 0.1$. It is further assumed that the molar flux J_R is small enough not to alter the velocity field.

Calculations for the semicontinuous reactor were performed for a single aspect ratio value of $S = 0.25$, two values of the Schmidt number, $Sc = 1$ and 10, and all of the Re and ϕ values that were previously considered for the discontinuous reactor model in Section 4.2.2 above. The discrete forms of equations (2.16)–(2.19) were advanced in time starting from the initial condition $C(0, R, Z) = 0$, that is, zero reactant concentration in the moment where the feed is initiated. In all of the cases a steady field was reached after a relatively short transient τ_S, as illustrated in Figure 4.10 for two particular instances. Note that in the abscissa of Fig. 4.10 time is scaled with the τ_{90} values previously obtained in the corresponding calculations for the discontinuous reactor mode. That is, in semicontinuous operation the initial transient is, in all of the cases investigated, $\tau_S \approx \tau_{90}$. This means that in practice the semicontinuous reactor would operate most of the time within a pseudo-steady state. Note that eventually the reactor must be stopped in order to withdraw the reaction products accumulated during each operation cycle. In all of the cases the steady state reached at the end of the initial transient coincided with the one that was directly calculated by setting the time derivative term in (2.16) equal to zero.

The qualitative behavior of the system during steady state, $\tau \geqslant \tau_S$, is similar to that of the asymptotic operation for discontinuous reactor ($\tau \geqslant \tau_\infty$) in the sense that efficiency, η, increases with increasing Re and Sc and decreases with increasing ϕ. Concentration contours plots are shown in Fig. 4.11. Note that the quantity plotted in this figure is $C_S(R, Z)\eta_S = C(\tau_S, R, Z)\eta(\tau_S)$, whose volumetric average is equal to one. Comparing with the discontinuous reactor (Figs. 4.5 and 4.6), we see that for $Sc = 1$ there is less solute accumulated in the inner core region. For $Sc = 10$, the concentration levels in the outer bulk region are considerably lower in Fig. 4.11d than they were for the discontinuous reactor in

a)

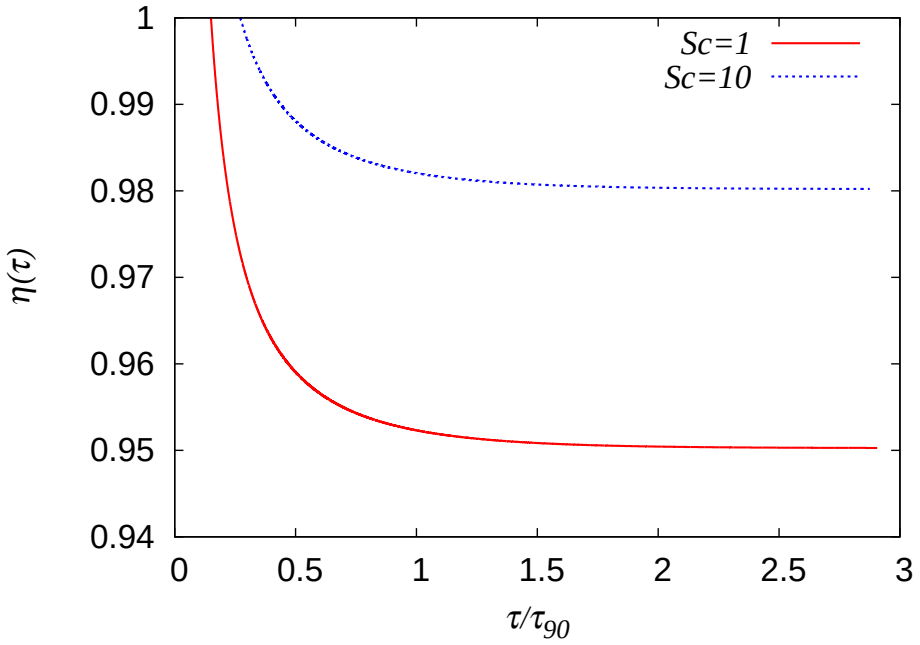

b)

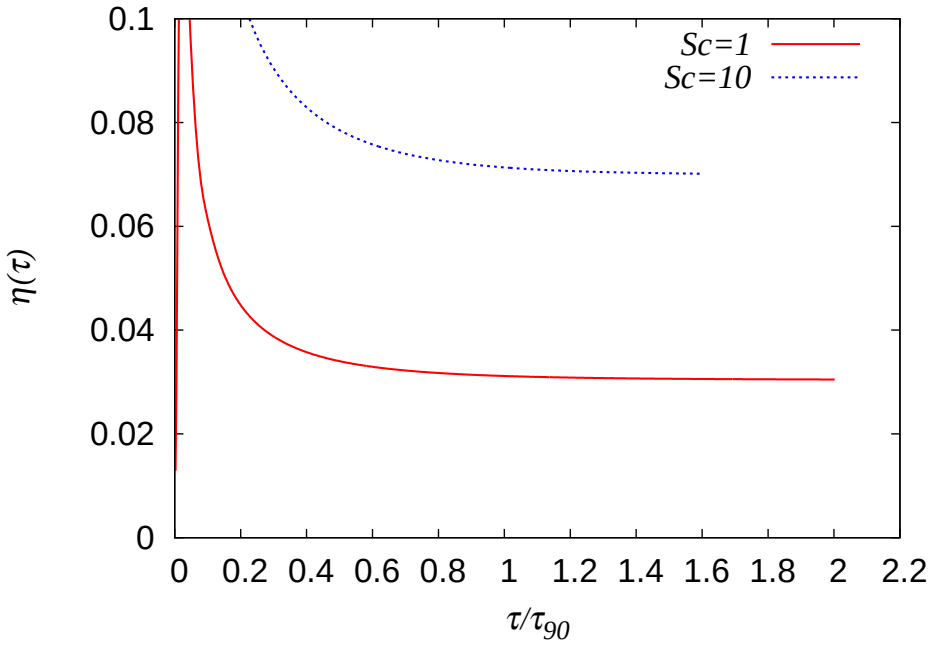

Figure 4.10: Evolution in time of the reactor efficiency, $\eta(\tau)$, for the cases of the semicontinuous reactor with $S = 0.25$, $Re = 7 \times 10^4$. The value of the Damköhler number is $\phi = 2$ in a) and $\phi = 2000$ in b). Note that in this figure the time in the abscissa is normalized as τ/τ_{90}, where the τ_{90} values are those previously calculated for the corresponding cases in the discontinuous reactor configuration.

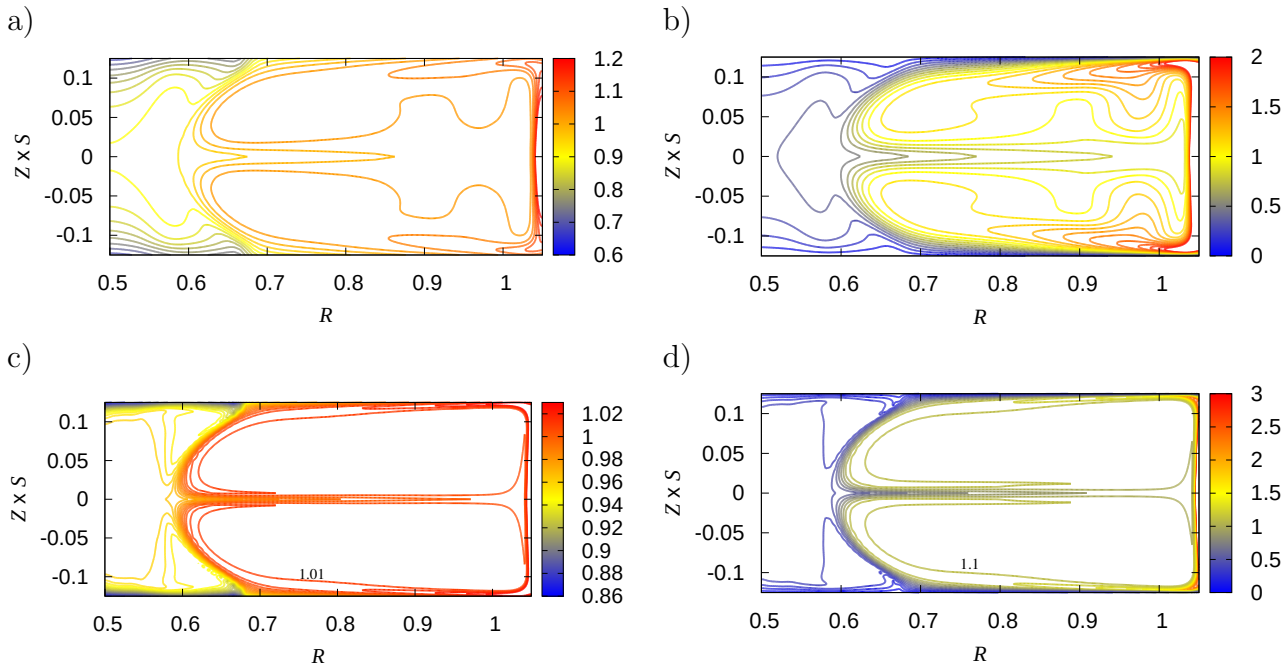

Figure 4.11: Concentration contours for the semicontinuous reactor calculations with $S = 0.25$ and $Re = 2 \times 10^4$. The values of the Schmidt number are $Sc = 1$ in plots (a) and (b) and $Sc = 10$ in (c) and (d). The values of the Damköhler number are $\phi = 2$ in plots (a) and (c) and $\phi = 200$ in (b) and (d). The quantity plotted in all four cases is the product $C_S(R, Z)\,\eta_S$, whose volumetric average is equal to one.

Fig. 4.6e. Not surprisingly, the highest concentrations levels in Fig. 4.11 are observed near the external enclosure wall where reactant is being continuously fed into the reactor. Figure 4.12 show the Λ_S profiles i.e., Λ in the steady state, for the same cases previously shown for the discontinuous reactor in Figure 4.8. In particular, comparing Figs. 4.8b and 4.12b we see that:

- The first local maximum near the disk-surface takes now a larger value, $\Lambda_S \geqslant 0.9$.
- The Λ_S value in the global maxima in the bulk region is now just a little higher than the first local maxima, $\Lambda_S \leqslant 1.2$; the global maxima value is roughly the same for $Sc = 1$ and 10.
- The location of the first local maximum seems closer to the disk surface for $Sc = 10$ than it is for $Sc = 1$
- The magnitude of the Λ_S drop after the first local maximum is maintained. Thus, direct solute transport by molecular diffusion from the bulk region into the disk Ekman layer remains problematic.
- The value of Λ_S at the local minimum at $Z = 0$ is now much higher ($\Lambda_S \approx 0.9$) and changes very little with Sc.
- The $\Delta\Lambda_S$ drop between the global maxima and the $Z = 0$ local minimum is now less than 0.3 units, much smaller than the drop between the first local maximum and the disk surface.

On the overall we see that in the semicontinuous reactor much less solute is trapped within the bulk region. This is not surprising since reactant is continuously being fed through the external porous wall with the maximum inlet flow occurring at the $Z = 0$ midplane. Thus, most of the reactant is being directly incorporated into the inwards stream between the two

a)

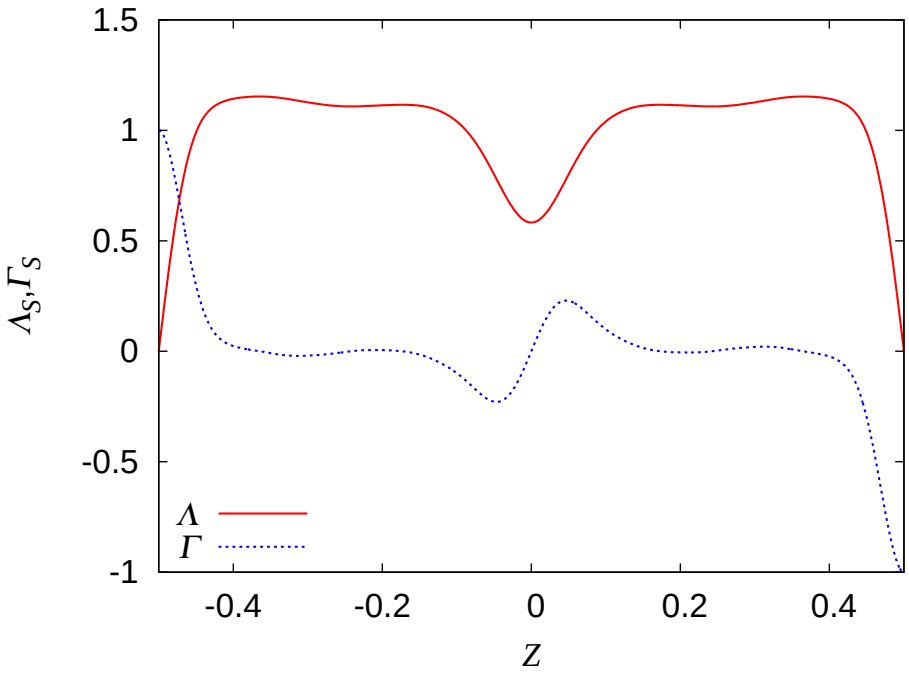

b)

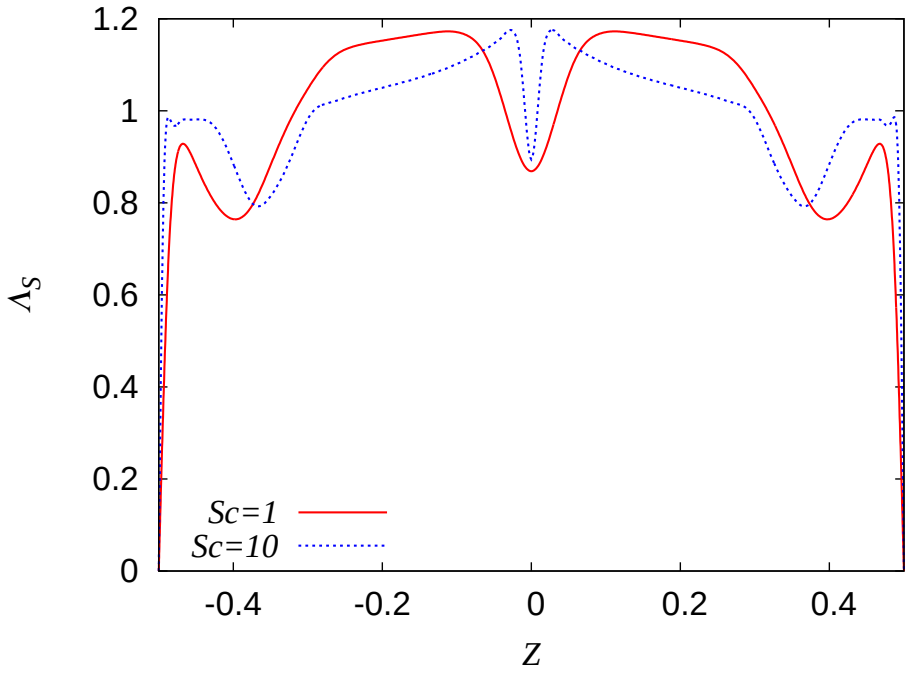

Figure 4.12: a) Axial profiles of the radially averaged normalized concentration and the normalized molar flux for $Re = 1 \times 10^4$, $Sc = 1$ and $\phi = 2$. The quantities Λ_S, and Γ_S are respectively defined in a similar manner as are Λ and Γ in Eqs. (4.21) and (4.22) except for the fact that the steady–state concentration, $C_S(R, Z)$, is used instead of the asymptotic concentration $C(\tau_\infty, R, Z)$. b) Axial profiles of Λ_S for $Re = 6 \times 10^4$, $\phi = 2000$ and $Sc = 1$ and 10.

counterrotating secondary vortices and it can afterward easily reach the vicinity of the disk surface. It is therefore not surprising that the concentration drop within the disk Ekman layers is now much larger thus implying a much larger rate of reactant consumption at the catalytic surface. Although not completely, now the overall mass transport seems to be much more boundary layer–controlled.

The calculated values of the Sherwood number (for $Re \geqslant 5 \times 10^3$) were fitted to an equation in the form:

$$\log Sh_S = a + b\log(Re) + c\log(Sc) + d\log(\phi) \tag{4.27}$$

where $Sh_S = Sh(\tau_S)$, i.e., Sherwood in the steady state, and the values $a = 0.5112 \pm 0.126$, $b = 0.4157 \pm 0.0117$, $c = 0.3602 \pm 0.00978$ and $d = 0.05402 \pm 0.00437$ were obtained. Compared to the fit (4.25) for the discontinuous reactor above, we see now a higher exponent in both the Reynolds and, especially, the Schmidt number, namely $b = 0.416$ instead of 0.373 and $c = 0.360$ instead of 0.137. The fact that the c value in (4.27) is much closer to the theoretical expectation ($c = 1/3$) confirms the notion that the overall mass transfer is now much more boundary layer–controlled than it was in the discontinuous reactor.

Figure 4.13 confirms that the fit of the calculated Sh_S values is much better than it was for the discontinuous reactor (Fig. 4.9). Moreover, we see in Fig. 4.13b that for the semicontinuous reactor the values of Sh_S are approximately in the same order of magnitude or, in most cases, surpass the theoretical values given by (4.26). In particular, for the largest Reynolds number investigated, $Re = 10^5$, the Sh_S values for $Sc = 10$ plotted in Fig. 4.13 are between 6 and 7 times higher than the corresponding values for the discontinuous reactor in Fig.4.9. Thus, it seems clear that the new semicontinuous configuration really overcomes the limitations that were detected in the discontinuous reactor as the mass transfer efficiency is highly improved.

4.3 Natural convection problem

4.3.1 Natural convection flow

We intend to analyze the viability of a mini-reactor, filled with an aqueous phase ($Pr = 6$), with a side length in the range 0.01 m$\leq L \leq$ 0.02 m, which would be easy to operate at a temperature drop in the range 5 K $\leq \Delta T \leq$ 10 K. Note that the specific catalyst surface would be in the range 50 m^2/m^3 $\leq L^2/L^3 \leq$ 100 m^2/m^3. An overall one–liter reactor volume could then be achieved by setting an array of about 30×30 mini–reactors embedded between two horizontal flat plates. Note that for a given total reactor volume the catalyst surface in 30×30 mini–cubes would be $(900)^{1/3}$ times larger than that provided by only one big cube. Assuming properties of the liquid phase similar to those of water the time scale for convection would range between $\tau_{conv} = 1.8$ and 9.9 s. Values of the Rayleigh number about $Ra = 10^5$ will be assumed. In practice, for given values of L and fluid properties the exact value of Ra would be determined through the value taken by ΔT during the operation.

Bifurcation Diagram

Figure 4.14 shows the calculated bifurcation diagram within the region of Ra of interest and a value of the Prandtl number equal to $Pr = 6$. The bifurcation diagram turns out to be a

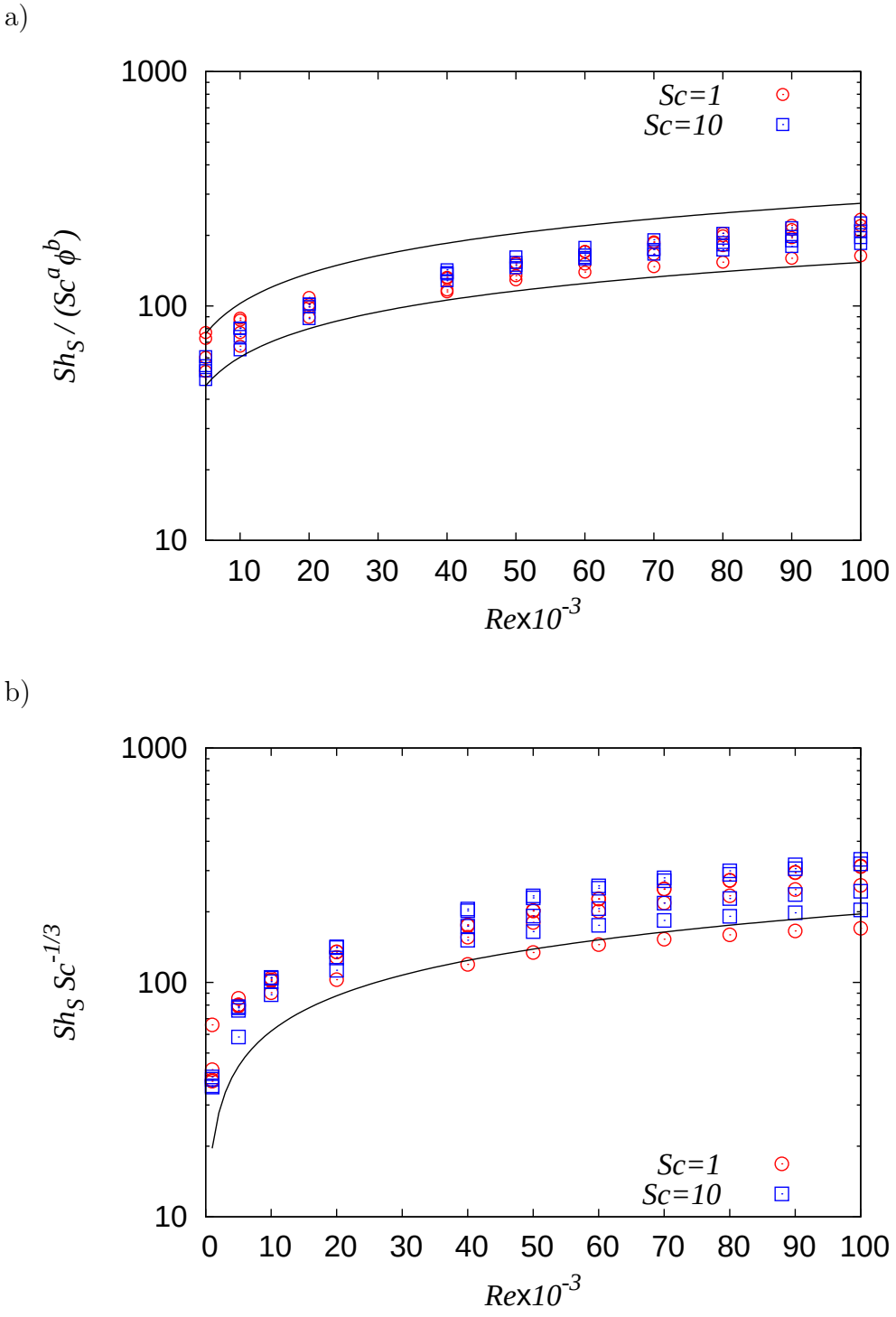

Figure 4.13: Variation with Re of the predicted values of the steady–state Sherwood number, Sh_S, for all of the calculations of the discontinuous reactor configuration. In a), Sh_S is divided by $Sc^c\phi^d$, where c and d denote the corresponding exponents obtained in the fit (4.27); the two solid lines denote the boundaries of the 95% confidence interval for the fit. In b), Sh_S is divided by $Sc^{1/3}$ instead and the theoretical boundary–layer prediction, Eq. (4.26), is plotted with a solid line. In both plots, circles and squares respectively denote the results obtained with $Sc = 1$ and 10.

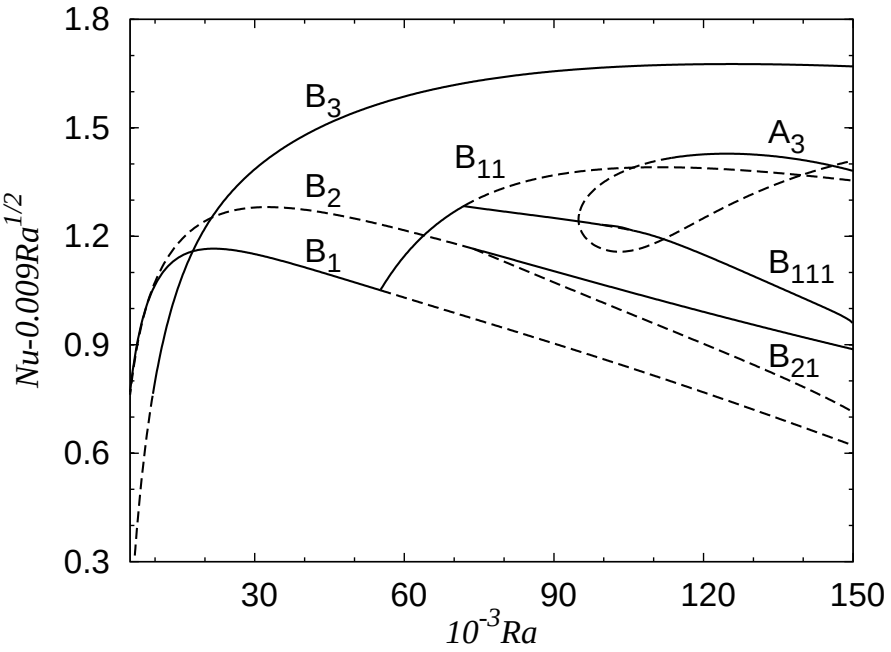

Figure 4.14: Bifurcation diagram for $Pr = 6$. Solid and dashed lines stand for stable and unstable solutions, respectively. Convective flow patterns that set in at a primary bifurcation are labeled B_i and flow patterns developed at bifurcation points of B_i are denoted by B_{ij} [55]. For the sake of clarity the variable $Nu - 0.009Ra^{1/2}$ was used instead of the Nusselt number Nu.

very useful tool to show the domains of existence, stability character, and bifurcations of the multiple solutions that may coexist as a function of a parameter. The Nusselt number, plotted in Fig. 4.14 as a function of Ra for the different solution branches, is the dimensionless convective heat transport coefficient defined by:

$$Nu = 1 - \int_{-1/2}^{1/2} \int_{-1/2}^{1/2} \frac{\partial \theta}{\partial Z}(X, Y, -1/2) dX dY \tag{4.28}$$

Note that for the sake of clarity the variable $Nu - 0.009Ra^{1/2}$ is used instead of the Nusselt number in Fig. 4.14. Stable (physically realizable) flow patterns are depicted with solid lines, while unstable patterns are represented by dashed lines. Only steady-state solutions, i.e., no time-dependent stable branches, have been found in the region with $Ra \leq 150,000$. Five different solution branches are stable within certain intervals of the Rayleigh number in the studied domain. At the onset of convection, $Ra_c = 3,389$, the initially stable ($x-$ or $y-$aligned) single-roll pattern B_1 and the initially unstable diagonally-aligned single roll pattern B_2 originate [54,70]. A third initially unstable flow pattern, denoted as B_3, branches from the basic conductive state at $Ra = 5,904$.

Figure 4.14 shows that the B_3 flow pattern has the widest stability domain ($Ra \geqslant 9,536$) and is the most effective flow pattern in transferring heat from the bottom to the top wall. Consequently, it would be ideal to operate the mini-reactor with the B_3 flow pattern set in. However, the question is whether or not B_3 will be the one flow pattern selected on startup. To investigate this issue, several simulations have been carried out using a code for the time-integration of Eqs. (2.21-2.24) that is described elsewhere [78]. Several tests have been performed for values of the Rayleigh number $Ra \times 10^{-3} = 75, 100, 125, 150$. In each test the initially conductive state ($\mathbf{V} = \theta = 0$) is seeded with a random perturbation and the time-integration is carried out until a given steady flow pattern is reached. The B_3 flow pattern

was always obtained at the three lowest values of Ra but at $Ra = 150 \times 10^3$ the preferred flow pattern was A_3. Notwithstanding, the desired B_3 pattern at $Ra = 150 \times 10^3$ is easily obtained by initially setting a value of $Ra = 125 \times 10^3$, which is increased to $Ra = 150 \times 10^3$ after a short time. The B_3 pattern developed at $Ra = 125 \times 10^3$ is therefore preserved when a further increase of 25×10^3 units in Ra is applied. Thus, the current study focuses on the steady flow pattern B_3.

The vertical velocity profiles on the horizontal planes $Z = 0$ and $Z = -0.25$ for the B_3 flow pattern at $Ra = 10^5$ are plotted in Fig 4.15. Figure 4.16 shows that the spatial con-

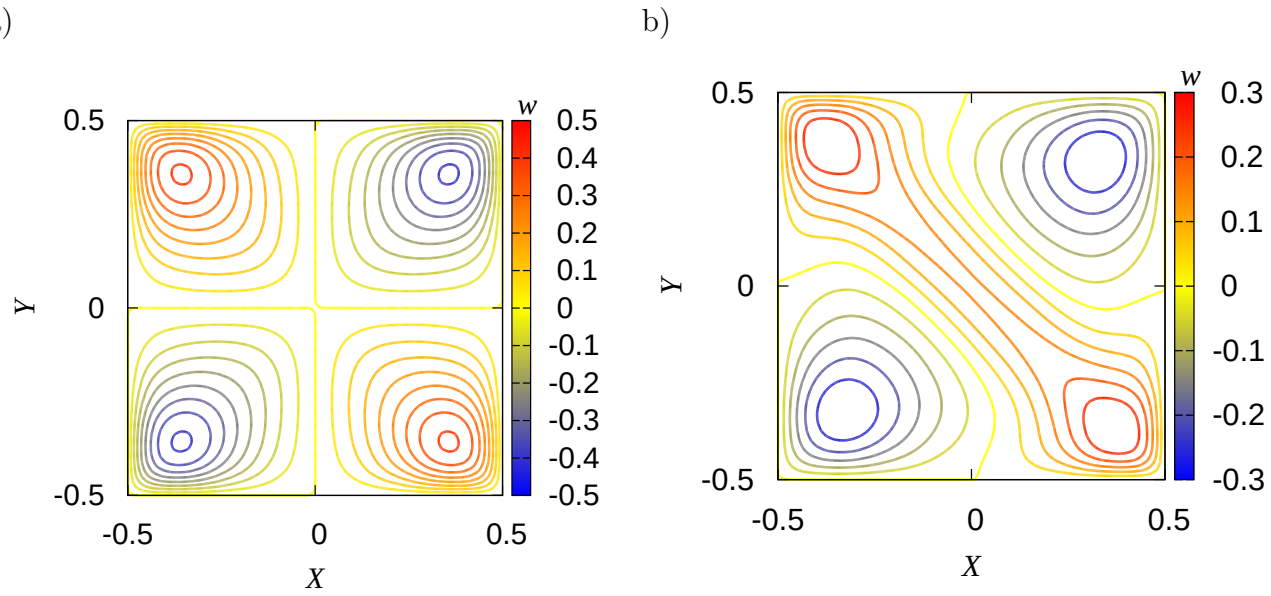

Figure 4.15: Contours of the vertical component of velocity, w, for the B_3 flow pattern at $Ra = 10^5$ and two different horizontal planes a) $Z = 0$ and b) $Z = -0.25$

figuration of the B_3 flow pattern at $Pr = 6$ consists of four connected half-rolls and is very similar to the ones reported at $Pr = 0.71$ and $Pr = 130$ [54,55]. This spatial configuration is invariant under the eight symmetry elements generated by $\mathbf{S_{d^+}}$ and $-\mathbf{S_y} = \mathbf{S_{d^+}} \cdot \mathbf{S_y} \cdot \mathbf{S_{d^+}} \cdot \mathbf{S_z}$, defined in (2.31)-(2.33). In particular the B_3 flow pattern is symmetric with respect to the two diagonal vertical planes $x = y$ ($\mathbf{S_{d^+}}$) and $x = -y$ ($\mathbf{S_{d^+}} \cdot \mathbf{S_x}$), with respect to π rotations around the $x-$, $y-$ or $z-$axis ($\mathbf{S_y} \cdot \mathbf{S_z}$, $\mathbf{S_x} \cdot \mathbf{S_z}$, $\mathbf{S_x} \cdot \mathbf{S_y}$) and with respect to $\pm\pi/2$ improper rotations around the $z-$axis ($\mathbf{S_{d^+}} \cdot \mathbf{S_y} \cdot \mathbf{S_z}$,$\mathbf{S_y} \cdot \mathbf{S_{d^+}} \cdot \mathbf{S_z}$).

It is shown below that the concept of a concentration boundary layer, which is closely related to a momentum boundary layer, plays a key role in the analysis of the present results. Concerning the momentum boundary layer it can be seen in Figs. 4.15 and 4.16 that the strongest fluid motion is located not far from the walls. In particular, there are strong upflows along two diagonally-opposed vertical edges of the cavity and strong downflows along the other two complementary edges. In addition, the fluid spreads laterally when such flows reach the vicinity of the top/bottom wall. The idea of decomposing Rayleigh-Bénard convection flows into two different regions, the boundary layers and a bulk region, is not only common but dominant in the field, e.g., [80, 81]. The thickness of the momentum boundary layer, denoted as δ_M, is assumed to be proportional to $1/\sqrt{Re}$. Defining the Reynolds number on the basis of U_0 and using the leftmost identity in (2.26), Re can be written as a function of the Ra and Pr:

$$\frac{\delta_M}{L} \propto \frac{1}{Re^{1/2}} \propto \left(\frac{\nu}{U_0 L}\right)^{1/2} = \frac{Pr^{1/2}}{Ra^{1/4}} \tag{4.29}$$

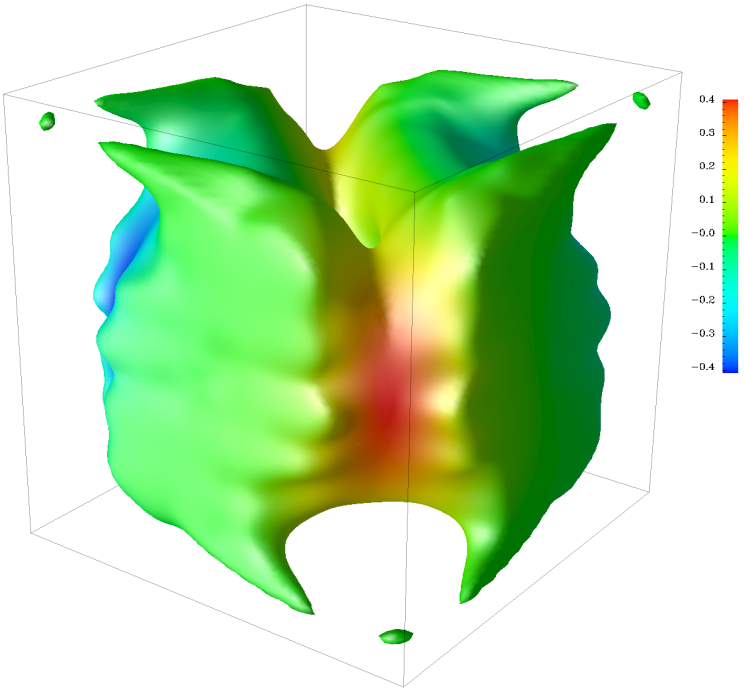

Figure 4.16: Three-dimensional picture of the flow pattern B_3 at $Ra = 10^5$. The vortical flow structure is portrayed using isosurfaces of $\lambda_2 = 0$, where λ_2 stands for the second largest eigenvalue of the sum of the symmetric and antisymmetric parts of the velocity gradient tensor [79].

The dependence of δ_M with $Ra^{-1/4}$ in (4.29) is consistent with the correlation of empirical data proposed by Grossmann and Lohse [80, 81]. Moreover, for a laminar boundary layer flow the ratio of the concentration boundary layer thickness, denoted as δ_C, to δ_M is expected to vary as $Sc^{-1/3}$ [82]. On these theoretical grounds, we should expect the behaviour:

$$\frac{\delta_C}{L} \propto Ra^{-1/4} Pr^{1/2} Sc^{-1/3} = Ra^{-1/4} Pr^{1/2} (LePr)^{-1/3} = Ra^{-1/4} Pr^{1/6} Le^{-1/3} \tag{4.30}$$

Dynamical Analysis

Figure 4.17 shows Poincaré maps calculated at the four horizontal planes $Z = 0$, $Z = -0.1$, $Z = -0.25$ and $Z = -0.4$ for the B_3 flow pattern at $Ra = 10^5$. Each point in these plots denotes the crossing of the reference plane by one particle at some time. The overall patterns in the Poincaré maps are useful to identify some relevant features and trends of the flow pattern. The characteristic diagonal symmetries of the solutions are clearly evident in Fig. 4.17 where red and blue dots have been respectively used for the crossing in ascending and descending directions, respectively. Note that the corresponding maps for a given Z could be obtained from those at $-Z$ by simply rotating the plot by $\pi/2$ and exchanging red and blue colors. The existence of regions where the flow is not transversal to the section, i.e., no particle is crossing it because velocity is tangent to the plane, is also shown in Fig. 4.17. In addition, these figures reveal the existence of sixteen regions with regular particle motion which are surrounded by regions of chaotic particle motion. The elliptic points at the center of each regular region correspond to time–periodic particle trajectories and are surrounded by regular KAM–tori [83] which act as barriers to transport. The practical interpretation is that particles located inside (outside) a regular region would never leave (enter) such region

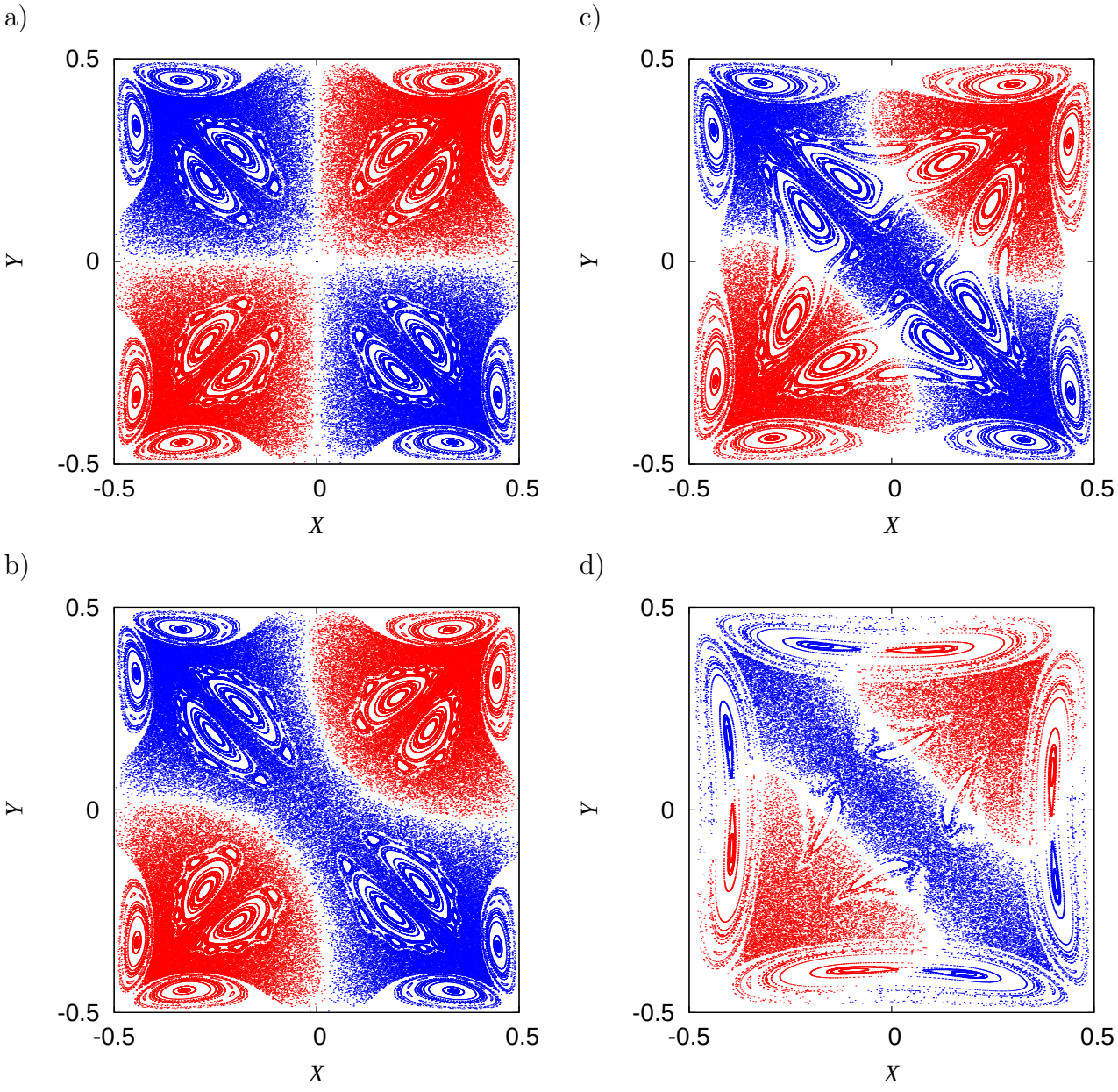

Figure 4.17: Poincaré maps for $Ra = 10^5$ at different heights of the cubical cavity (a) $Z = 0$, (b) $Z = -0.1$, (c) $Z = -0.25$ and (d) $Z = -0.4$. Red and blue dots respectively represent ascending and descending orbits.

if convection was the only transport mechanism. Thus, Poincaré maps in Fig. 4.17 give us a qualitative picture of mixing in conditions of very low molecular diffusivity, i.e., large values of the Schmidt number.

Figure 4.18 shows the dependence on Ra of the volumetric percentage of chaotic region and the maximal Lyapunov's exponent. According to the notion that *chaoticity* favours mix-

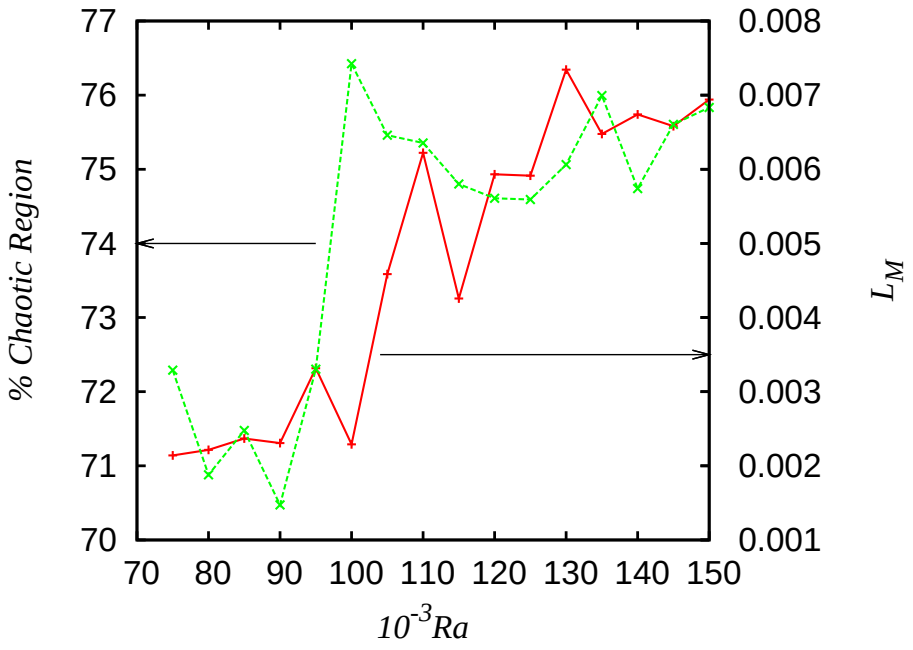

Figure 4.18: Variation with Ra of the maximal Lyapunov exponent, L_M (solid line), and of the percentage of chaotic region (dashed line). The values of L_M have to be read on the right y-axis.

ing, the fact that the percentage of chaotic region is relatively high in all cases ($70 - 77\%$) foretells good mixing properties for the B_3 flow pattern. Figure 4.18 shows that the percentage of chaotic region undergoes a rapid increase between $Ra = 9 \times 10^4$ and $Ra = 10^5$. The maximal Lyapunov's exponent also presents a similar sudden increase but it takes place at slightly larger Rayleigh numbers ($10^5 \leq Ra \leq 1.1 \times 10^5$).

As it is discussed below, dynamical analysis offers a relatively fast (and cheap) qualitative characterization of the mixing capabilities of a given flow pattern but to obtain quantitative descriptors we must turn to classical transport phenomena tools.

4.3.2 Concentration field

The ODE system (3.29) was numerically integrated for $Pr = 6$ and four different values of the Rayleigh number, namely $Ra \times 10^{-3} = 75$, 100, 125 and 150. Four different values of the Schmidt number which lead to four Lewis numbers ($Le = Sc/Pr$) were considered in each case, namely $Le = 1$ ($Sc = 6$), $Le = 10$ ($Sc = 60$), $Le = 100$ ($Sc = 600$) and $Le = 1000/3$ ($Sc = 2000$). In addition, three different values of the Damköhler number, namely 1, 10 and 100 (representing cases of comparatively slow, average and fast reactions, respectively), were used for each (Ra, Le) pair. Thus a total amount of 48 time-integrations of (3.29) were performed. The reactant conversion χ, may be used as a first indicator of the reactor efficiency. Figure (4.19) shows that $\chi(\tau)$ depends strongly on both Le and ϕ. Let us define τ_{90} as the time at which 90% of the initial amount of solute has reacted, that is τ_{90} satisfies

$\chi(\tau_{90}) = 0.9$. Figure 4.19 shows that, for a given value of Ra, the larger ϕ and Le are, the smaller τ_{90} is. These trends agree with the evolutions with time of the efficiency factor $\eta(\tau)$, plotted in Fig. 4.20 for $Ra = 75 \times 10^3$.

The increase of $\eta(\tau)$ as ϕ is decreased in Fig. 4.19 is due to the fact that an increase in the reaction speed leads to a decrease of the overall mass transfer resistance (see Eq. (4.11)). Figure 4.20 also shows that, for a given ϕ, the efficiency $\eta(\tau)$ grows when Le is increased, that is, when molecular diffusion is slower, a behavior that might seem contradictory at first sight. This behavior, along with the dependence of the present results on the Rayleigh number, will be analyzed and discussed in the next subsection.

In all of the cases investigated, $\eta(\tau)$ reaches a plateau–like value after a short transient, as shown in Fig. 4.20. Note that the time τ_∞ needed to achieve a plateau–like value is always less than 0.1 and much smaller than the corresponding τ_{90} value in Fig.4.19. Let η_∞ denote the asymptotic value of η at the plateau–like region, $\tau \geq \tau_\infty$. This remarkable behavior of $\eta(\tau)$ is consistent with the fact that the spatial distributions of the normalized concentration Σ, defined in (4.20), become *frozen*, i.e., nearly independent of time, as soon as $\tau = \tau_\infty$ ($\eta(\tau) = \eta_\infty, \forall \tau \geq \tau_\infty$), as illustrated in Fig 4.21. This figure shows isocontours of Σ at the horizontal midplane $Z = 0$ for $Ra = 1.5 \times 10^5$, $Le = 10$ and $\phi = 10$ at two different times. The isocontours of Σ at $Z = 0$ plotted in Fig 4.22 for $Ra = 10^5$, $\phi = 100$ and $\tau = \tau_{90}$ at the four studied Lewis numbers, show that the distributions of Σ depend strongly on the Lewis number. Figure 4.22 also shows that the lowest concentrations are achieved near the two diagonally opposite edges with strong downflow whereas the largest concentration values are found in the bulk region. The normalized concentration distribution plotted in Fig. 4.22 (a) for $Le = 1$ ($Sc = Pr$) resembles the distribution of the vertical velocity component plotted in Fig. 4.15 (a). As Le increases, the concentration gradients are confined to the vicinity of the lateral walls and increasingly smaller scales are visible in the plots. The development of small scales in the concentration distributions is the way in which *chaoticity*, evident in the Poincaré maps, manifests itself in the continuous model at large values of Le. Actually, in the cases with lower molecular diffusivity, $Le = 100$ and 333.33, the horizontal concentration distribution does not resemble the velocity distribution but it looks rather familiar to the Poincaré maps in Fig. 4.17 (a). In particular, regularity regions far from the walls in Fig. 4.17 are associated with regions of largest Σ levels in Fig. 4.22 (d).

The overall picture that we can extract from Fig. 4.22 is that two types of regions may also be distinguished in regard to their mass transfer characteristics. Such a distinction becomes especially relevant as Le increases, that is, as molecular diffusion becomes slower. On one hand, there are near-wall regions where fluid motion is strong and therefore convection is efficient in carrying solute down to the vicinity of the catalytic surface. For reasons that are discussed below, we refer to such regions as boundary layer regions. On the other hand, there is a bulk region comprising most of the space away from the cavity walls. At high Le values the bulk region is characterized by the presence of regularity domains in the Lagrangian analyses. Since mass transfer between regions of regular and chaotic advection is largely due to molecular diffusion, it is not surprising that larger values of concentration are observed in the bulk, regular regions.

4.3.3 Scaling Analysis

Since the level of efficiency of the current reaction system can be characterized by means of the asymptotic quantity η_∞ it would be desirable to correlate η_∞ as a function of the problem parameters, Ra, Sc and ϕ. However, we found that a direct fit of the form $\eta_\infty \propto Ra^a Le^b \phi^c$

a)

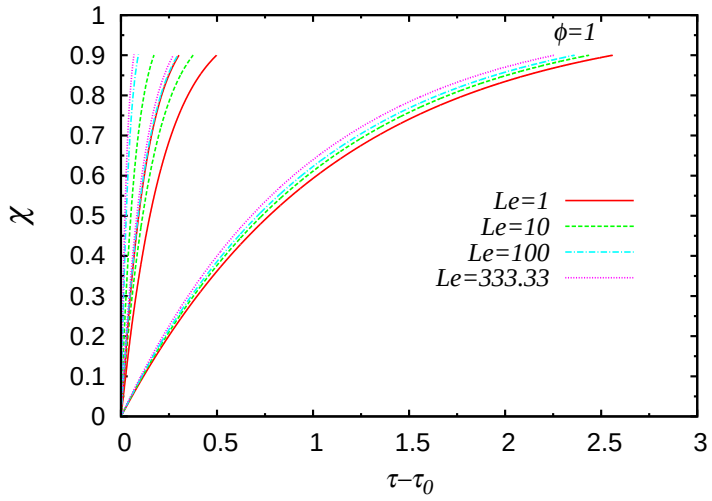

b)

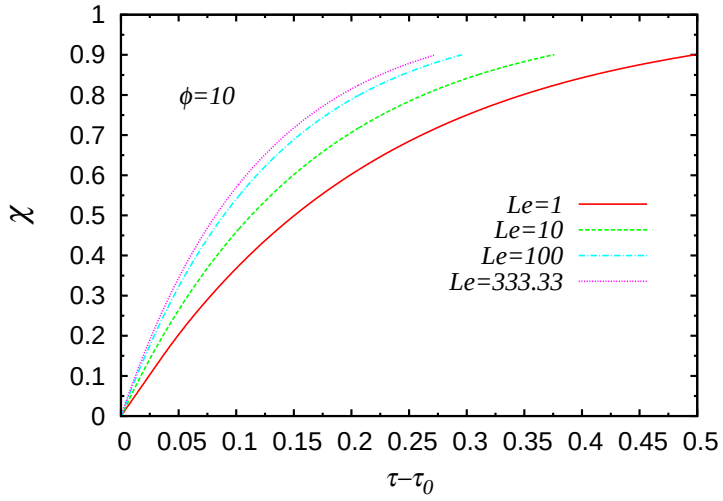

c)

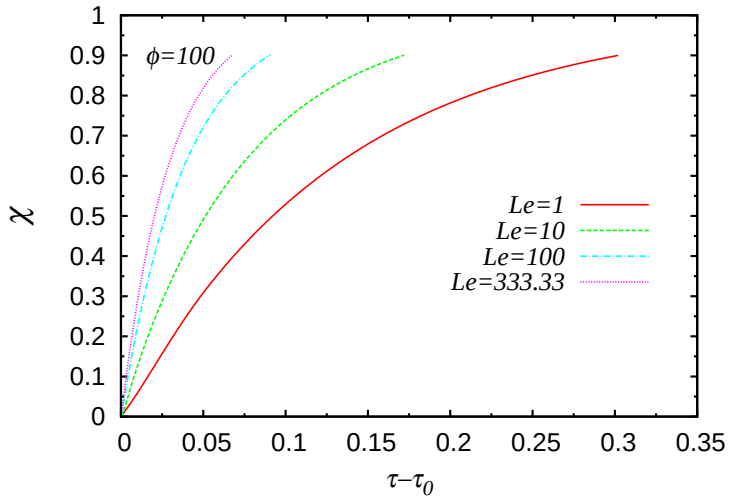

Figure 4.19: Evolution in time of the reactant conversion, χ, for $Ra = 75 \times 10^3$ and different values of ϕ and Le. (a) Conversion curves for all the (Le, ϕ) pairs. (b) Zoom with the curves for $\phi = 10$ alone. (c) Zoom with the curves for $\phi = 100$ alone.

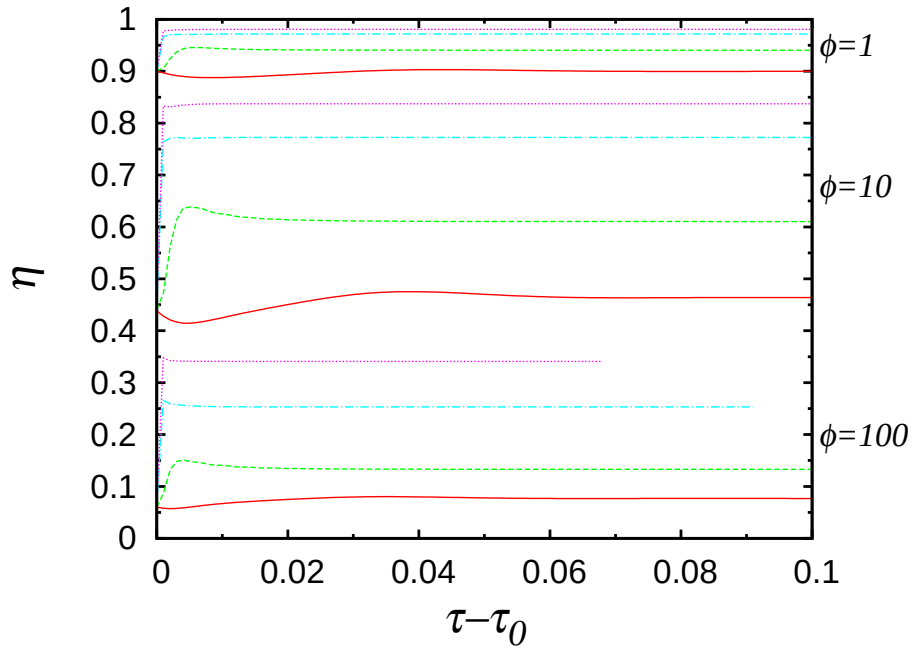

Figure 4.20: Evolution in time of the reactor efficiency, η, for $Ra = 75 \times 10^3$ and different values of ϕ and Le. The values of ϕ are pointed out at the right side; from bottom to top, the first four curves stand for $\phi = 100$, the next four for $\phi = 10$ and the last four for $\phi = 1$. The value of the Lewis number in each case is denoted by its line style: solid lines ($Le = 1$), dashed lines ($Le = 10$), dashed-dotted lines ($Le = 100$) and dotted lines ($Le = 333.33$).

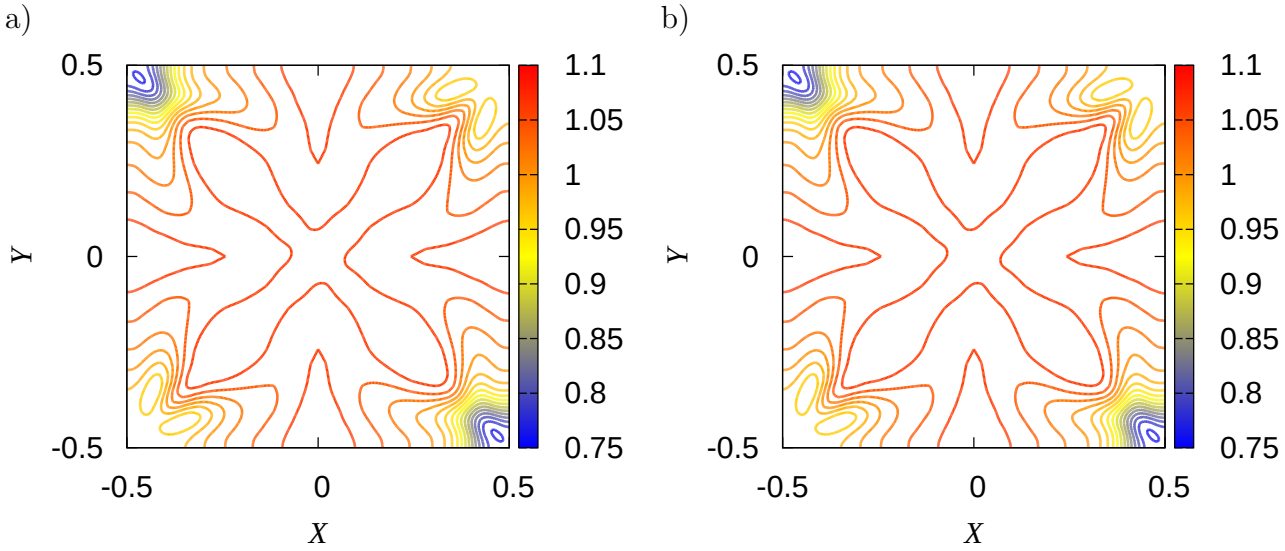

Figure 4.21: Horizontal midplane ($Z = 0$) distributions of the normalized solute concentration Σ for the case with $Le = 10$, $Ra = 1.5 \times 10^5$ and $\phi = 10$ and two different times, namely (a) $\tau - \tau_0 = 5 \times 10^{-2}$ and (b) $\tau = \tau_{90}$, the time at which the reactant conversion has reached its target value $\chi(\tau_{90}) = 0.90$.

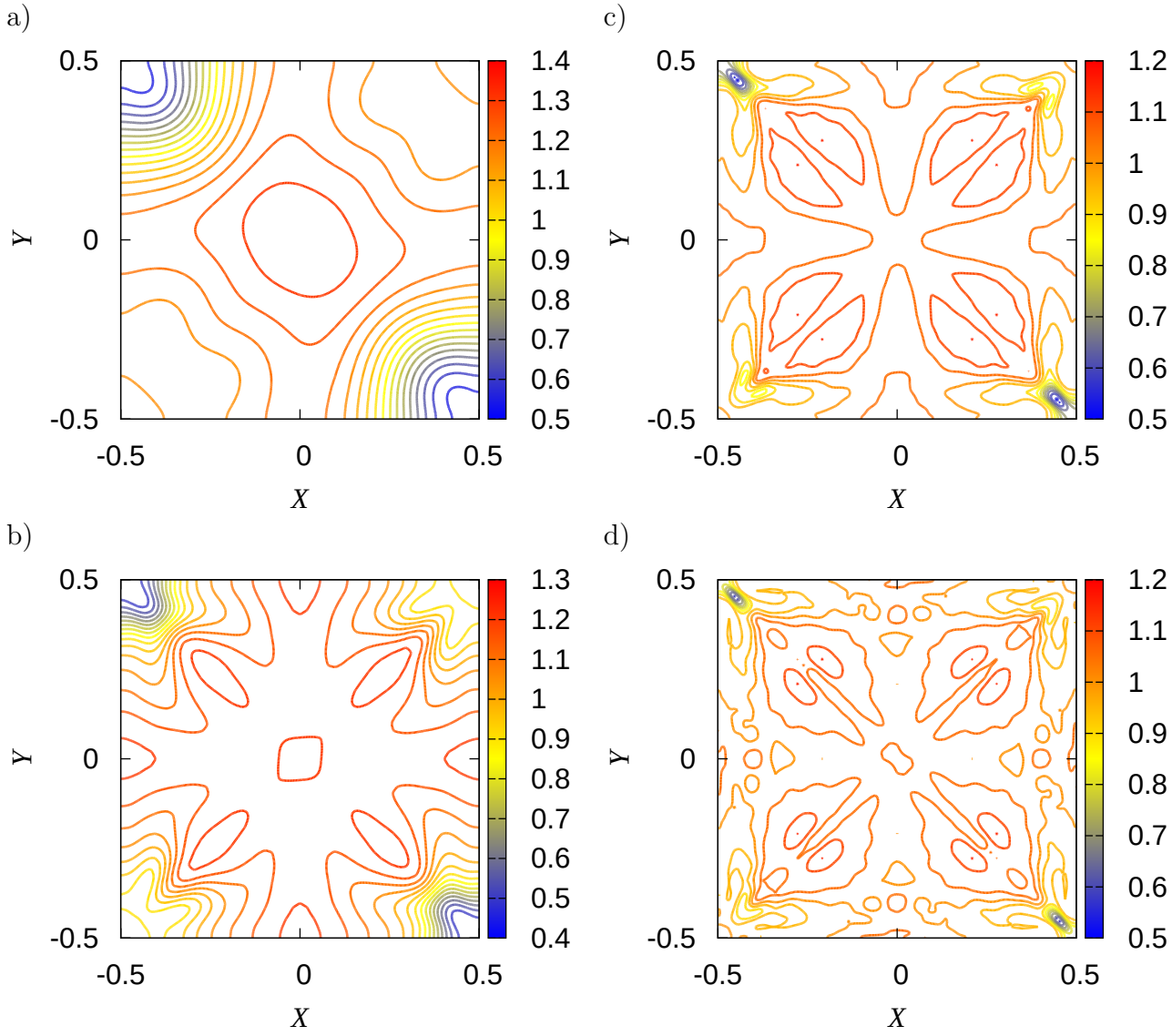

Figure 4.22: Horizontal midplane ($Z = 0$) distributions of the normalized solute concentration Σ at times such that $\tau = \tau_{90}$ for $Ra = 1.0 \times 10^5$, $\phi = 100$ and four different values of the Lewis number, namely a) $Le = 1$, b) $Le = 10$ c) $Le = 100$ d) $Le = 333.33$.

was useless. Our goal at that point was to figure out the reason why η_∞ increases with increasing Le. Let us understand the role of the natural convection flow as being responsible to carry solute, distributed throughout the cavity, into the bottom wall boundary layer. Let us also assume that the notion of a concentration boundary layer makes sense for the present problem. Then it follows that solute nearby the bottom wall would diffuse down to the catalytic surface through a concentration boundary layer of an average thickness δ_C/L. A side–effect of the above assumptions is that the characteristic time for diffusion in the present problem would not be $\tau_{diff} = L^2/D$ but rather δ_C^2/D. Concerning the concentration boundary layer, the following questions must be addressed: can we somehow identify it? If so, how can we measure its thickness, δ_C/L? And, can δ_C/L be correlated to the problem parameters, Ra, Sc and ϕ?

Figure 4.23 shows the variation with the vertical coordinate Z of the normalized horizontally averaged concentration Λ, at a time that verifies $\tau \geq \tau_\infty$ for three different sets of values of the parameters Le, ϕ and Ra. Like the quantity Σ in (4.20), $\Lambda(\tau, Z)$ becomes nearly independent of time as soon as $\tau \geq \tau_\infty$. In all the cases investigated the quantity $\Lambda(\tau, Z)$ drops from a roughly constant bulk value to zero within a narrow region of the Z domain. This fact corroborates the hypothesis of the existence of a concentration boundary layer region, near the bottom surface of the cavity, at which large vertical concentration gradients are reached. Figure 4.23 (a) shows that the concentration boundary layer at $Le = 1$ is relatively thick. The small drop near the top wall in the concentration profiles plotted in Fig. 4.23 may also be interpreted in terms of boundary layer transport. Since fluid motion is strongest in the momentum boundary layer regions solute in the vicinity of the top wall is transported downwards much more easily than is solute in the bulk region. In other words, molecular diffusion of solute in the bulk region seems to be the limiting mechanism for mass transfer but, fortunately, diffusion does not only occur towards the bottom surface but also towards the top and lateral walls.

The qualitative tendency described by Eq. (4.30) predicts that the width of the concentration boundary layer δ_C/L decreases whenever either Le or Ra are increased. Notwithstanding, in order to obtain a quantitative relation between δ_C/L, Le and Ra we must find out a method to estimate δ_C/L. One option is to define $-1/2+\delta_C/L$ as the vertical position fulfilling the following identity for any τ such that $\tau \geq \tau_\infty$:

$$\frac{\widehat{C}(\tau, Z)}{\overline{C}(\tau)} - \eta(\tau) = 0.90 \left(\frac{\widehat{C}(\tau, Z_\infty)}{\overline{C}(\tau)} - \eta(\tau) \right) \tag{4.31}$$

In (4.31) Z_∞ is defined so that the horizontal plane $Z = Z_\infty$ verifies the following conditions: the plane is far from the bottom surface ($Z_\infty + 1/2 \gg 0$), the plane is outside the momentum boundary layer ($-1/2 + \delta_M/L < Z_\infty < 1/2 - \delta_M/L$) and the quantity $\widehat{C}(\tau, Z_\infty)/\overline{C}(\tau)$ has reached a practically constant value, that is $\widehat{C}(\tau, Z)/\overline{C}(\tau)$ is nearly constant for any $\tau \geq \tau_\infty$ and for any Z in an interval $(Z_\infty - d, Z_\infty + d)$, with $d > 0$ being far from zero. Nevertheless, the concentration profiles plotted in Fig. 4.23 suggest that this method may produce inaccurate values. In particular, the predicted δ_C/L in Fig.4.23 (a) might be too large and the irregularity of the concentration profile in Fig.4.23 (c) introduces some arbitrariness in the choice of Z_∞.

We propose here a different method to characterize the variation of the concentration boundary layer as a function of the problem parameters Ra, Le and ϕ. It is based on the use of both the normalized concentration profile, $\Lambda(\tau, Z)$, and a normalized horizontally averaged

a)

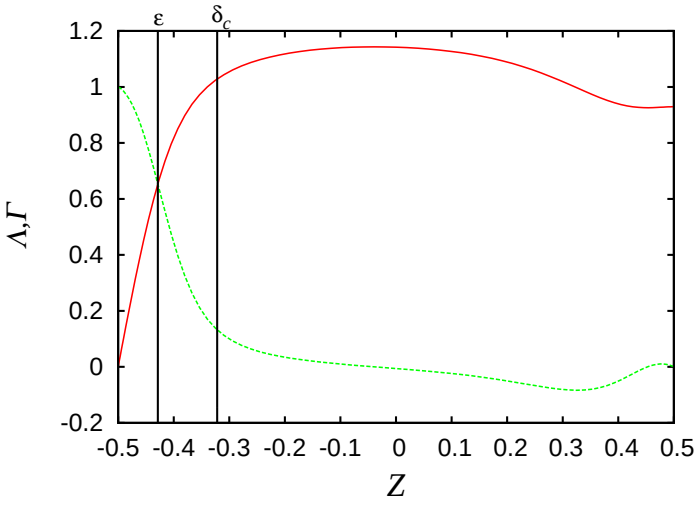

b)

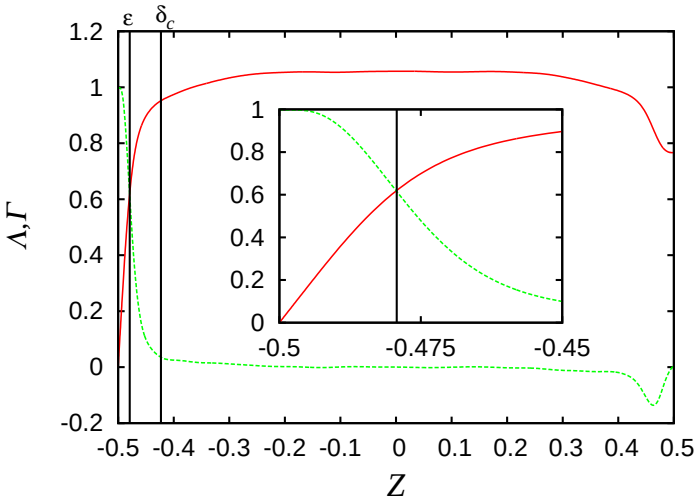

c)

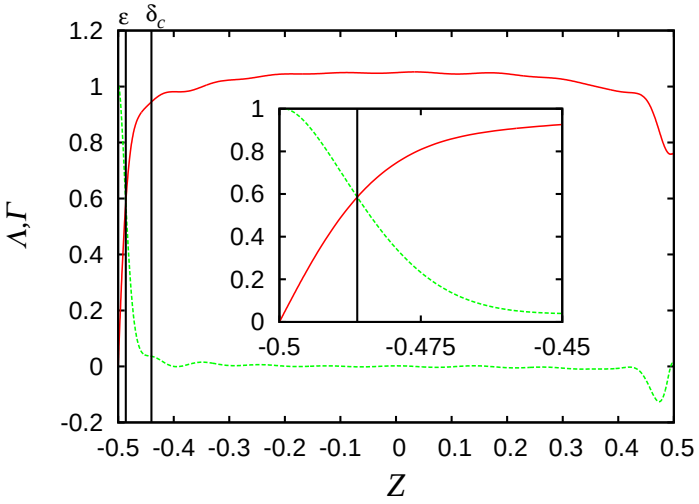

Figure 4.23: Vertical profiles of the normalized horizontally averaged solute concentration, Λ, and molecular diffusion flux, Γ for the cases with (a) $Ra = 1.5 \times 10^5$, $Le = 1$ and $\phi = 1$, (b) $Ra = 7.5 \times 10^4$, $Le = 100$ and $\phi = 100$ and (c) $Ra = 7.5 \times 10^4$, $Le = 333.33$ and $\phi = 1$. On top of each plot the symbol δ_C points the location for the average concentration boundary layer thickness as defined by Eq. (4.31) whereas ε points to the location defined by Eq. (4.32).

vertical diffusion flux defined in (4.22). Note that we can also safely assume $\Gamma(\tau, Z) = \Gamma(\tau_\infty, Z)$ for $\tau \geq \tau_\infty$. The vertical profiles of Γ, also included in Fig. 4.23, decay rapidly from its maximum value, $\Gamma(\tau, -1/2) = 1$, as Z increases and are basically zero in the bulk region. Looking at different profiles of Γ we observed that the point at which the rate of decay of Γ, i.e., $\partial_z\Gamma$, reaches its maximum was always very close to the point at which Γ and Λ intersect. Since the intersection point was always quite close to the bottom plate we propose the quantity ε that verifies

$$\Gamma(\tau, \varepsilon/L) = \Lambda(\tau, \varepsilon/L) \quad \forall\tau \ \text{ such that } \ \tau \geq \tau_\infty \tag{4.32}$$

as an indicator of the thickness of the concentration boundary layer. One reason for using ε instead of δ_C in the current analysis is that the former of these two quantities correlates better with the problem parameters (a second, more important reason for the choice of ε is explained below). The values of ε/L were computed through Eq. (4.32) for 48 sets of parameters and then fitted to an equation of the form:

$$\frac{\tilde{\varepsilon}}{L} + \frac{1}{2} = A\, Ra^a Le^b \phi^c \tag{4.33}$$

The following values of the fitting parameters A, a, b and c were obtained

$$A = 2.95, \ a = -0.309, \ b = -0.329 \ \text{ and } c = 7.76 \times 10^{-3} \tag{4.34}$$

Figure 4.24 shows that the fitted values, denoted as $(\widetilde{\varepsilon}/L + 1/2)$, obtained from substitution of Ra, Le and ϕ into Eq. (4.33) with the values of A, a, b and c given in (4.34) are in all cases in good agreement with the $(\varepsilon/L{+}1/2)$ values computed through Eq. (4.32). Note that the

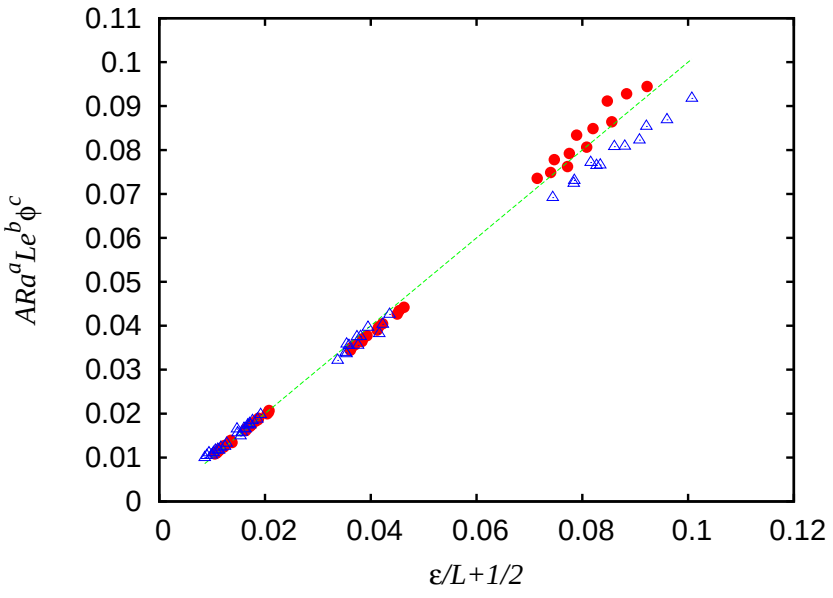

Figure 4.24: Two different fittings for ε as a function of Ra, Le and ϕ according to Eq. (4.33). The abscissa correspond to the ε values calculated with Eq. (4.32) for all of the 48 cases investigated. Hollow triangles ($\triangle$) denote the fit predictions for ε when the exponents a and b are fixed to $-1/4$ and $-1/3$, respectively; in this case $c = 2.36 \times 10^{-2}$ and $A = 2.23$ with a residual sum of squares equal to 0.228. Filled circles ($\bullet$) represent the fit prediction for ε when none of the exponents are fixed; in this case $a = -0.309$, $b = -0.329$, $c = 7.76 \times 10^{-3}$ and $A = 2.95$ with a residual sum of squares equal to 4.94×10^{-2}.

fitting values obtained for the exponents a and b are similar to the theoretical exponents $-1/4$ and $-1/3$ proposed for δ_C/L in Eq. (4.30). This similarity suggests that Eq. (4.32)

provides a suitable method to characterize the width of the concentration boundary layer in terms of $(\varepsilon/L+1/2)$. Nonetheless, Fig. 4.24 also shows that the fit obtained when the exponents a and b in (4.33) are fixed to their theoretical values, i.e. $a=-1/4$ and $b=-1/3$, is worse than the optimal one. Note that the exponent of ϕ in (4.33) is very close to zero. Although it has been found that the value of the exponent, $c=7.76\times10^{-3}$, is statistically significant (the hypothesis $c=0$ is rejected with a 99.8% confidence) its closeness to zero indicates that the dependence of ε on ϕ should be accepted with caution.

We are finally in a position to analyze the dependence of the asymptotic reactor efficiency, η_∞, on ε/L. Let us first define the quantity

$$\gamma=\frac{\widehat{C}(\tau,\varepsilon/L)-\tilde{C}(\tau,-1/2)}{\widehat{C}(\tau,\varepsilon/L)-\widehat{C}(\tau,-1/2)} \tag{4.35}$$

where $\tilde{C}(\tau,-1/2)$ is the extrapolated value of $\widehat{C}$ at $Z=-1/2$ obtained from the first order approximation

$$\tilde{C}(\tau,-1/2)=\widehat{C}(\tau,\varepsilon/L)-\left(\frac{\varepsilon}{L}+\frac{1}{2}\right)\frac{\partial\widehat{C}}{\partial Z}(\tau,\varepsilon/L) \tag{4.36}$$

Combining (4.35) and (4.36) we obtain:

$$\frac{\partial\widehat{C}}{\partial Z}(\tau,\varepsilon/L)=\frac{\gamma\left(\widehat{C}(\tau,\varepsilon/L)-\widehat{C}(\tau,-1/2)\right)}{\varepsilon/L+1/2} \tag{4.37}$$

Introducing the definition of Γ, Eq. (4.22), into the left hand side of (4.37) and then combining the result with Eqs. (4.32) and (4.21) yields:

$$\gamma\left[\overline{C}(\tau)-\widehat{C}(\tau,-1/2)\right]=\phi\widehat{C}(\tau,-1/2)(\varepsilon/L+1/2) \tag{4.38}$$

Dividing both sides in equality (4.38) by $\overline{C}(\tau)$ and using the definition (4.2) for η_∞ the following relation between η_∞ and ε/L is obtained:

$$\eta_\infty=\frac{1}{1+\gamma\phi(\varepsilon/L+1/2)} \tag{4.39}$$

All of the values of γ, calculated using Eqs. (4.35) and (4.36) for all of the sets of parameters investigated, were close to 1.4. In particular the values of γ ranged within $1.40\leq\gamma\leq1.42$ for $Le>1$ and within $1.30\leq\gamma\leq1.33$ for $Le=1$. Hence, we propose the following general expression to determine the dependence of η_∞ on $\varepsilon/L+1/2$:

$$\eta_\infty\approx\frac{1}{1+1.4\phi(\varepsilon/L+1/2)} \tag{4.40}$$

Figure 4.25 shows that Eq. (4.40) provides good predictions for η_∞. Note that Eq. (4.40) makes clear that since ε/L decreases with increasing values of the Lewis and Rayleigh numbers the asymptotic reactor efficiency η_∞ can only increase with Le and/or Ra for a given value of ϕ.

Figure 4.26 shows that the values of τ_{90} obtained from the time integration of the governing equations are in good agreement with the predicted $\tilde{\tau_{90}}$ values estimated by (4.18). This agreement indicates that the short transients observed in Fig. 4.20 have no significant effect on the overall efficiency. Figure 4.26 also shows that good predictions for τ_{90} can be obtained

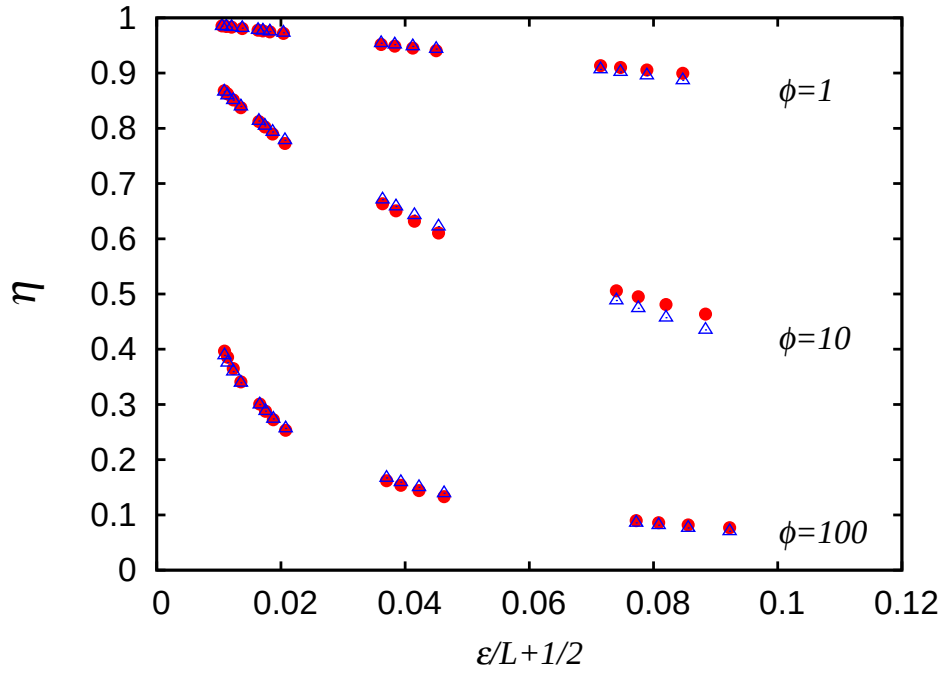

Figure 4.25: Asymptotic reactor efficiency, η_∞, as predicted by Eq. (4.40) as a function of $\varepsilon + 1/2$. Filled circles (•) denote the values obtained when $\varepsilon + 1/2$ values obtained numerically, using Eqs. (4.21), (4.22) and (4.32), are introduced into Eq. (4.40). Hollow triangles (△) denote the values given by Eq. (4.40) when $\varepsilon + 1/2$ is obtained from the fit (4.33-4.34) instead.

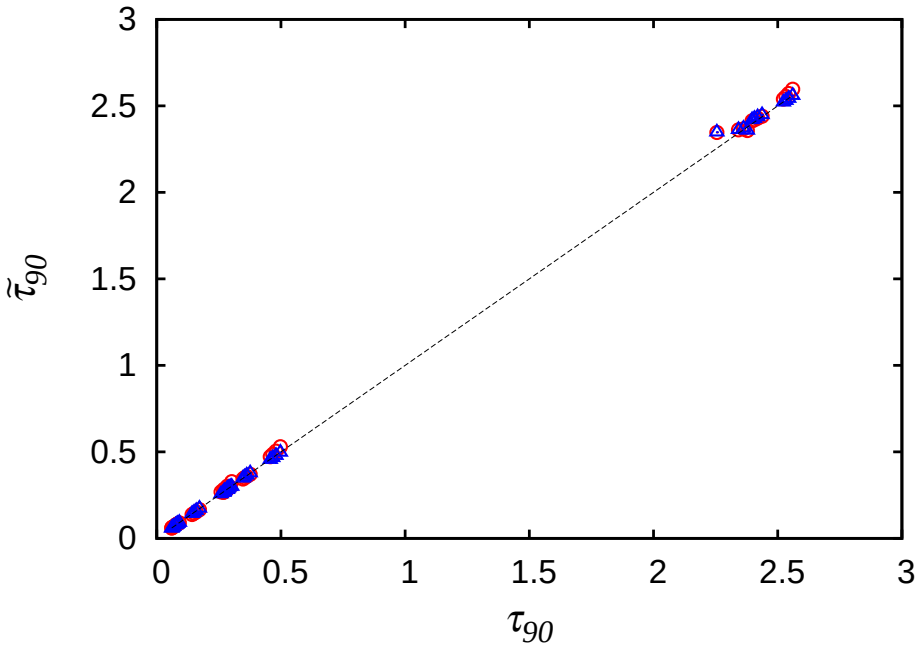

Figure 4.26: Time needed to reach a 90% of solute conversion, $\chi(\tau_{90}) = 0.90$, as predicted by Eq.(4.18). The abscissa correspond to the $\tilde{\tau}_{90}$ values obtained directly from the numerical integrations of Eq. (3.29) for all of the 48 cases investigated. Triangles (△) denote the values obtained when the values of η_∞ used in Eq. (4.18) are obtained directly from the numerical integrations of Eq. (3.29). Circles (○) denote the values given by Eq. (4.18) when the values of η_∞ predicted by Eqs. (4.33), (4.34) and (4.40) are used instead.

by first using Eqs. (4.33) and (4.40) to estimate η_∞ and then introducing its predicted value in Eq. (4.18).

On the other hand, note that Eq. (4.18) provides the interpretation for η_∞ as being the inverse of the ratio of the time needed to reach a target conversion to the corresponding time that would be needed in the ideal limit of a perfect mixing ($\eta = 1$). The value of η_∞ is therefore a good indicator on the level of mixing intensification achieved by natural convection if we compare it with the corresponding value that is obtained for the reaction-diffusion 1D problem. If, for example, $Ra = 75 \times 10^3$ and $Sc = 2000$ we have $\eta_\infty = 0.981$ for $\phi = 1$ but the 1D solution (3.36) yields $\eta_{\infty,1D} = 0.742$. That is, we have $\eta_\infty/\eta_{\infty,1D} = 1.32$ so that the contribution of natural convection to solute mixing is a modest one. If, on the contrary, the chemical reaction is a relatively fast one ($\phi = 100$) then we have (for the same Ra, Sc values) $\eta_\infty/\eta_{\infty,1D} = 0.341/0.0252 = 13.5$, i.e., natural convection plays a key role in mixing enhancement.

Chapter 5

Conclusions

We proposed two new alternatives of catalytic reactor where mixing is promoted by a forced and natural convection flow.

The forced convection driven reactor consisted of a stack of corotating disks in a cylindrical cavity with catalyst implanted at the opposing surfaces of each particular pair of disks. The idea was to take advantage of the secondary motion generated by the disk rotation, which takes the form of a pair of counter–rotating vortices that bring fluid closer to the disk surface where the presence of a boundary layer region should highly enhance mass transfer into/from the disk surface. Two different operation modes were considered. First, a discontinuous mode with reactant being initially spread through the whole reactor volume. In the second, semicontinuous mode, reactant is continuously being fed through the external enclosure wall.

One interesting and not initially expected feature was that the relative concentration distributions in the reactor and, as a consequence, the efficiency indicator $\eta(\tau)$ become roughly independent of time after a short transient. We exploited this fact to show that the time needed to reach a target conversion of the reactant is well predicted by the proposed methodology.

In principle, one would expect that mass transfer efficiency, in terms of Sherwood number, should not depend, for given values of the ϕ, Re, Sc and S problem parameters, on the operation mode. However, present results show quite the opposite trend. The discontinuous reactor was not very efficient, especially in conditions of slow molecular diffusion, i.e., high Schmidt numbers. In particular, for $Sc = 10$ the semicontinuous reactor yielded values of Sh several times higher than the corresponding ones for the discontinuous reactor. Indeed, the calculated Sh values for the discontinuous reactor are below the corresponding values given by the boundary layer analysis of the flow over a free–rotating disk. Although mass transfer within the disk boundary layer is quite efficient, there is a high mass transfer resistance associated to the transport of reactant from the bulk region into the vicinity of the disks. If we invoke the heat/mass transfer analogy it is worth noting that the study by Herrero et al. [30] showed that the corotating disk pair was also relatively inefficient in transferring heat between a bottom hot disk and a cold top disk. In particular, the Nusselt numbers calculated in [30] were about one half the theoretical boundary layer prediction. Let us consider, for example, the case with $S = 0.25$, $Re = 10^5$ and $Sc(Pr) = 10$. The heat transfer correlation proposed in [30] yields a Nusselt number based on R_2, $Nu = 179$, whereas present results for the discontinuous reactor range between $Sh = 182$ ($\phi = 2000$) and 235 ($\phi = 2$) and the theoretical dependence (4.26) gives $Sh = 422$. In the semicontinuous operation mode, however, we obtain (for the same $S = 0.25$, $Re = 10^5$ and $Sc = 10$) values of the Sherwood number in the range $439 \leq Sh \leq 721$, that is above the theoretical boundary–layer value,

for all the ϕ values investigated. The big difference between the discontinuous and the semicontinuous mode is that in the latter, reactant is fed near the external enclosure wall so that it is easily incorporated into the secondary flow main stream. Thus, the key point for efficient operation of the corotating reactor is in avoiding reactant to become trapped in the bulk region.

Comparing our results of the semicontinuous reactor with Meeuwse et al.'s [25], we see that these authors reported that for $Re \approx 10^5$ the Sherwood number achieved is practically the same obtained by the configuration of the free rotating disk. For the present semicontinuous reactor at the same Re number, the value of Sh exceeds the one of the free rotating disk for all the combinations of Sc and ϕ studied except for the one of $Sc = 1$ and $\phi = 2$. This suggests that for higher Sc it will be much more efficient and hence it will be much more competitive than the Meeuwse et al.'s reactor. To select the best value obtained for the convective mass transfer coefficient $\widehat{K}$ we multiply the highest Sh obtained by the diffusive coefficient D and divide by the radius R_2 (we take the same that Meeuwse et al. uses, $R_2 = 0.066$ m). For an aqueous phase, $D \approx 10^{-9}$ m^2/s, the mass transfer coefficient is approximately $\widehat{K} \approx 10^{-5}$ m/s. Meeuwse et al. reported similar values for low rotational speeds. For a gaseous phase, $D \approx 10^{-5}$ m^2/s, the mass transfer coefficient is around $\widehat{K} \approx 0.11$ m/s. This surpasses Meeuwse et al.'s result of 7.9×10^{-4} m/s for $\Omega = 157$ rad/s, however is still below Meeuwse et al.'s best result of 0.22 m/s. Nonetheless we must keep in mind that Meeuwse et al. studied much higher Reynolds values (turbulent regime), furthermore the parameters used may not be exactly the same. In any case, the semicontinuous reactor seems like a propitious election rather than conventional models and should be explored more. We think that the current model of the corotating disk reactor, despite some limiting assumptions, correctly captures the main physics of the system including the dependence of the mass transfer efficiency on the problem parameters. This makes it a promising alternative, so more realistic configurations can be studied and implemented experimentally.

The natural convection driven reactor was studied in a cubical cavity, taking advantage of the previous knowledge of the flow within such a cavity. In terms of particle advection, the selected flow patterns did not provide a completely chaotic system because of the presence of regularity regions which may act as barriers to transport in conditions of very low molecular diffusivity. Notwithstanding, it was found that the reactor efficiency is basically determined by flow and mass transfer within the boundary layer regions.

As well as in the forced convection driven reactor, the relative concentration distributions and the efficiency $\eta(\tau)$, became nearly independent of time after a short transient, which accordingly led to predict the time to achieve a given conversion. We took advantage of this to address for a new method to characterize the dependence of the concentration boundary layer thickness on the parameters of the problem Ra, Le and ϕ. Furthermore, a relation that gives a good forecast of η_∞ for any values of Ra, Le and ϕ within the ranges investigated was produced.

Provided that the chemical reaction is not a fast one, the natural convection-mixed reactor that is proposed in the present study should be competitive when compared to usual reactor designs that incorporate moving mechanisms. For example, for a value of $\tau_{conv} \approx 2$ s with $L = 10^{-2}$ m the condition $\tau_{conv} \ll L/k$ (the characteristic time for convection much smaller than the characteristic time for chemical reaction) is fulfilled whenever $k \ll 5 \times 10^{-3}$ m/s (or $\phi \ll 330\, Sc$ for a value of the thermal diffusivity equal to $\alpha = 1.5 \times 10^{-7}$ m^2/s). Moreover, in terms of mass transfer efficiency the proposed reactor system compares well with other systems where mass transfer is promoted by means of a forced convection flow. For $Ra = 10^5$, a rough estimate of a Reynolds number in the current reactor is $Re \approx 0.5 Ra^{1/2} Pr^{-1} = 26.4$ (see Eq. (4.29) and Fig. 4.15, where $0.5U_0$ is suggested as an estimate of the largest

velocities found in the present problem). From Eqs. (4.10), (4.33) and (4.40) we have $\widehat{Sh} \approx (1/1.4)[1/(\varepsilon/L + 1/2)] = 0.242 Ra^{0.309} Le^{0.329} \phi^{-0.00776}$, which yields a value of the Sherwood number equal to $\widehat{Sh} = 55.4$ for $Ra = 10^5$, $Le = 333.33$ and $\phi = 100$. This value of $\widehat{Sh}$ is, for example, higher than the value $\widehat{Sh} = 40.1$ that is obtained for laminar mass transfer on a rotating disk surface at $Re = 26.4$ and $Sc = 2000$ ($\widehat{Sh} = 0.620 Re^{1/2} Sc^{1/3}$ [82]) but lower than the value $\widehat{Sh} = 67.7$ that would be obtained in a commercial hollow-fibre blood oxygenator ($\widehat{Sh} = 0.8 Re^{0.59} Sc^{0.33}$ [84]; these authors also reported the correlation $\widehat{Sh} = 0.8 Re^{0.47} Sc^{0.33}$ for a hand made hollow-fibre module, which yields $\widehat{Sh} = 46.9$ for $Re = 26.4$ and $Sc = 2000$).

Given that the geometries of the two kind of reactors, forced and natural convection driven, are different, and the range of parameters studied are different too, making a comparison between both of them or even with other kind of reactors, as we have seen, can be done only in a qualitatively way. We can use however, the Sherwood number to compare the semicontinuous forced convection and natural convection reactors. As previously detailed, for the corotating disk reactor, $Sh = Sh_{fc}$, depends on the characteristic length R_2, whereas in the cubical reactor, $Sh = Sh_{nc}$, depends on the cavity side length, L. To establish a comparison between these two geometries, we may use instead, a common characteristic length such as the reactor volume per unit catalyst area, which is L for the cubical reactor and $H/2 = S/(2R_2)$ for the corotating disk reactor. Based on these lengths, we have $Sh_{nc} = 10.55$ for $Ra = 1.5 \times 10^5$, $Sc = 6$ and $\phi = 1$. For the semicontinuous reactor ($S = 0.125$) we have, for the case with $Sc = 10$ and $Re = 10^5$ (for an equivalent value of $\phi = 2$), $Sh_{fc} = 90.23$. From the relation $Re \approx 0.5 Ra^{1/2} Pr^{-1}$, previously mentioned, we see the corresponding Re to the above $Ra = 1.5 \times 10^5$ is $Re \approx 32$. Since in both cases we deal with laminar boundary layer flow, we might expect a dependence of the type $Sh \propto Re^{1/2} Sc^{1/3}$, so that the present $Sh_{nc} = 10.55$ value can be extrapolated, for $Re = 10^5$ and $Sc = 10$, to $Sh_{nc}^{ex} \approx 702$, that is, a value 8 times larger than the actual $Sh_{fc} = 90.23$ that is obtained in the corotating disk reactor, which led us to think that the natural convection driven reactor may have much better performance than the forced convection one for the same set of parameters.

Comparison with results of Al-Shannag et al. [12, 13], is also difficult since the systems investigated are not completely the same. In [12] they studied a Michaelis-Menten kinetics, i.e, $J = \phi C/(1 + \beta C)$. In the limit $\beta \to 0$ the kinetics would be of first order like ours. Hereafter, we compared the efficiency they obtained for $\beta \leqslant 0.01$ and $\phi = 1$ with the efficiency we obtained for our reactors. In the forced convection case we compare for the case $Pe = 10^3$, which corresponds to $Re = 1000$ and $Sc = 1$. Al-Shannag et al. obtained $\eta \approx 0.84$ and we obtained $\eta = 0.89$ for the semicontinuous reactor configuration, which are very similar. In the natural convection case the range of Peclet number are between 130 and 200, for the range of Rayleigh studied and $Sc = 6$. For these range of Peclet numbers, Al-Shannag et al. obtained an efficiency of $\eta \approx 0.55$, while we obtained $\eta = 0.9$ in the worst of the cases. In [13] a first order reaction was studied and the result of efficiency were pretty similar to those of [12] for the conditions commented. Henceforth we see the high potential the natural convection driven reactor has.

We present our model of reactors as a very good alternative to traditional ones, however it must be taken into account what application is going to be given to them. Thus, we can say for example, that the semicontinuous reactor we proposed is better than the cubical one in the sense that it is efficient for fast reactions and different phases. Nevertheless, in the case of slow reactions we could say the cubical reactor shows a better mixing since all the transport is being driven by the boundary layer on the contrary to the co-rotating disks

reactor in which a big resistance is still prone by the bulk region.

Future research, based on more intensive calculations and/or experiments, might consider higher Rayleigh numbers (turbulent flow in the natural convection case) as well as higher Reynolds numbers ($3D$–unsteady or even turbulent flow for the forced convection case) and high concentrations of reactant/products. It would be very interesting to study a mixed convection case. For example, the corotating disks reactor considering non–isothermal effects and, especially, operation in continuous mode by feeding a stream through the gap between the disks tip and the enclosure wall (similarly to the setup in the rotor–stator system reported in [25]).

Despite our work is considered for basic type of reactions it results very promising to consider these configurations in experimental work with different kind of reaction and several reactor sizes. Therefore, the cubical reactor and the corotating disk reactor (especially if operated in semicontinuous or continuous mode) that are proposed in the present work may be a good alternative to more classical reactor designs.

Appendix A

Discretization procedure of the forced convection problem

The aim of this appendix is to give some details of the tau–Galerkin method used to discretize the governing equations. We start with the mass transfer conservation equations (2.16)-(2.19). Note that these equations can be written in a compact form as

$$\frac{\partial C}{\partial \tau} - \nabla^2 C + ReSc\nabla \cdot (C\mathbf{V}) = 0 \tag{A.1}$$

$$\frac{\partial C}{\partial Z}(R, \pm 1/2) \pm \phi C(R, \pm 1/2) = 0 \tag{A.2}$$

$$\frac{\partial C}{\partial R}(\gamma, Z) = 0 \tag{A.3}$$

$$\frac{\partial C}{\partial R}(1, Z) - J_R(Z) = 0 \tag{A.4}$$

where

$$\nabla = \left(\frac{\partial}{\partial R}, \frac{1}{S}\frac{\partial}{\partial Z}\right)$$
$$\nabla^2 = \left(\frac{1}{R}\frac{\partial}{\partial R}\left(R\frac{\partial}{\partial R}\right) + \frac{1}{S^2}\frac{\partial^2}{\partial Z^2}\right)$$
$$\mathbf{V} = (U, W)$$

Let us first recall that, as it was discussed in Section 4.2.1 only solutions with velocity fields symmetric with respect the plane $Z = 0$ were obtained in the current work. As a consequence, only even functions in Z are considered when the concentration is expanded in terms of the basis function. Thus, the concentration expansion is written as

$$C(\tau, R, Z) = \sum_{i=0}^{N_R} \sum_{j=0}^{N_Z/2} c_{i2j}(\tau) T_i(R^*) T_{2j}(Z^*) \tag{A.5}$$

where $R^* = 2[(R-\gamma)/(1+\epsilon-\gamma) - 1/2]$, $Z* = 2Z$ and T_i are the Chebyshev polynomials. In addition, by substituting Eq. (3.8) in (2.9)-(2.10) and replacing the basis functions f_i by the corresponding linear combination of Chebyshev polynomials (see Section 3.1.1), the velocity vector $\mathbf{V}$ takes the form

$$\mathbf{V}(\tau, R, Z) = \begin{pmatrix} U(\tau, R, Z) \\ W(\tau, R, Z) \end{pmatrix} = \sum_{i=0}^{N_{R,\Psi}} \sum_{j=0}^{N_{Z,\Psi}} \varphi_{ij}(\tau) \begin{pmatrix} T_i(R^*) T_j'(Z^*) \\ T_i'(R^*) T_j(Z^*) \end{pmatrix} \tag{A.6}$$

The tau–Galerkin method consists in projecting Eq. (A.1) into the subspace generated by all the basis functions in the concentration expansion except for those $T_{N_R-1}(R^*)$, $T_{N-R}(R^*)$, T_{N-Z-2} or $T_{N-Z}(Z^*)$. The basis function that are not used to project Eq. (A.1) are used to project boundary conditions (A.2)-(A.4). Therefore, application of the tau–Galerkin method converts equations (A.1)-(A.4) into the following equations:

$$\left\langle \frac{\partial C}{\partial Z}, T_i T_{2j} \right\rangle - \left\langle \nabla^2 C, T_i T_{2j} \right\rangle + ReSc \left\langle \nabla \cdot (C\mathbf{V}), T_i T_{2j} \right\rangle = 0 \quad \text{with} \quad i = 0, \cdots, N_R - 2 \quad \text{and} \quad j = 0, \cdots, N_Z/2 - 2 \tag{A.7}$$

$$\left\langle \frac{\partial C}{\partial Z}(R, 1/2), T_i T_{2j}(1/2) \right\rangle + \langle \phi C(R, 1/2), T_i T_{2j}(1/2) \rangle = 0 \quad \text{with} \quad i = 0, \cdots, N_R - 2 \quad \text{and} \quad j = N_Z/2 \tag{A.8}$$

$$\left\langle \frac{\partial C}{\partial Z}(R, -1/2), T_i T_{2j}(-1/2) \right\rangle - \langle \phi C(R, -1/2), T_i T_{2j}(-1/2) \rangle = 0 \quad \text{with} \quad i = 0, \cdots, N_R - 2 \quad \text{and} \quad j = N_Z/2 - 1 \tag{A.9}$$

$$\left\langle \frac{\partial C}{\partial R}(\gamma, Z), T_i(\gamma) T_{2j} \right\rangle = 0 \quad \text{with} \quad i = N_R \quad \text{and} \quad j = 0, \cdots, N_Z/2 \tag{A.10}$$

$$\left\langle \frac{\partial C}{\partial R}(1+\epsilon, Z), T_i(1+\epsilon) T_{2j} \right\rangle - \langle J(Z), T_i(1+\epsilon) T_{2j} \rangle = 0 \quad \text{with} \quad i = N_R - 1 \quad \text{and} \quad j = 0, \cdots, N_Z/2 \tag{A.11}$$

where $\langle\rangle$ represents the inner product. Note that due to the symmetries of the problem Eq. (A.8) is equivalent to Eq. (A.9).

Integrals involved in the calculation of the inner products in Eq. (A.7)-(A.11) are of the type:

$$\begin{array}{lll} \int_{-1}^{1} R^* T_i T_j \omega(R^*) dR^*, & \int_{-1}^{1} T_i T_j \omega(Z^*) dZ^*, & \int_{-1}^{1} T_i' T_j \omega(R^*) dR^*, \\ \int_{-1}^{1} R^* T_i'' T_j \omega(R^*) dR^*, & \int_{-1}^{1} T_i'' T_j \omega(Z^*) dZ^*, & \int_{-1}^{1} T_i' T_j T_k d\omega(R^*) R^*, \\ \int_{-1}^{1} T_i T_j' T_k \omega(Z^*) dZ^*, & \int_{-1}^{1} T_i T_j' T_k \omega(R^*) dR^*, & \int_{-1}^{1} T_i' T_j T_k \omega(Z^*) dZ^*, \\ A \int_{-1}^{1} e^{-\frac{Z^{*2}}{\sigma^2}} T_i \omega(Z^*) dZ^* & & \end{array} \tag{A.12}$$

where ω is the Chebyshev weight function, $\omega(x) = (1 - x^2)^{-1/2}$. Once the inner products in Eq.(A.7)-(A.11) are calculated these equations can be written in the matricial form as:

$$\begin{pmatrix} \mathbf{B} & \mathbf{B_b} \end{pmatrix} \begin{pmatrix} \dot{\mathbf{c}} \\ \dot{\mathbf{c_b}} \end{pmatrix} = \begin{pmatrix} \mathbf{L} & \mathbf{L_b} \end{pmatrix} \begin{pmatrix} \mathbf{c} \\ \mathbf{c_b} \end{pmatrix} \tag{A.13}$$

$$\begin{pmatrix} \mathbf{D} & \mathbf{D_b} \end{pmatrix} \begin{pmatrix} \mathbf{c} \\ \mathbf{c_b} \end{pmatrix} = \mathbf{J_b} \tag{A.14}$$

Let us define $DS = (N_R - 1)(N_Z/2 - 1)$ and $DB = N_Z + 2N_R$. Then, $\mathbf{B}$ and $\mathbf{L}$ are square matrices of dimension DS, $\mathbf{B_b}$ and $\mathbf{L_b}$ are matrices of dimension $(DS \times DB)$, $\mathbf{D}$ is a matrix of dimension $(DB \times DS)$ and $\mathbf{D_b}$ is a square matrix of dimension DB. The flux

entering the reactor is represented by the vector $\mathbf{J_b}$ whose dimension is (DB). Note that in the discontinuous mode $\mathbf{J_b} = 0$. Whereas the coefficients c_{i2j} in the concentration expansion (3.11) with $i = 0, \cdots, N_R - 2$ and $j = 0, \cdots, N_Z/2 - 2$ are contained in the vector $\mathbf{c}$ of dimension DS, the vector $\mathbf{c_b}$, whose dimension is DB, contains those coefficients with either $i = 0, \cdots, N_R - 2$ and $j = N_Z/2 - 1, N_Z/2$ or $i = N_R - 1, N_R$ and $j = 0, \cdots, N_Z/2$.

Isolating $\mathbf{c_b}$ from Eq. (A.14) and inserting the result into Eq. (A.13) leads to the ordinary differential equation

$$\hat{\mathbf{B}}\dot{\mathbf{c}} = \hat{\mathbf{L}}\mathbf{c} + \hat{\mathbf{A}} \tag{A.15}$$

where

$$\hat{\mathbf{B}} = \mathbf{B} - \mathbf{B_b}{\mathbf{D_b}}^{-1}\mathbf{D} \tag{A.16}$$

$$\hat{\mathbf{L}} = \mathbf{L} - \mathbf{L_b}{\mathbf{D_b}}^{-1}\mathbf{D} \tag{A.17}$$

$$\hat{\mathbf{A}} = \mathbf{L_b}{\mathbf{D_b}}^{-1}\mathbf{J_b} \tag{A.18}$$

Equation (A.15) is advanced in time by means of a second order implicit backward–differencing scheme (BDF2). Note that once the value of $\mathbf{c}(\mathbf{t})$ is obtained, $\mathbf{c_b}(\mathbf{t})$ can easily be obtained from Eq. (A.14).

The steady state version of the momentum conservation equations (2.1)–(2.4) are also discretized by means of a tau–Galerkin method. The discretization procedure reduces these equations to a nonlinear system of algebraic equations that, adopting the summation convention indices, can be written as

$$L_{ji}d_i + Q_{jin}d_id_n = 0 \tag{A.19}$$

In Eq. A.19 the elements of the vector $\mathbf{d} = (d_1, \cdots, d_K)$ are the unknowns, that is the coefficients in expansion (3.8). The matrices with components L_{ji} and Q_{jin} contain respectively the coefficients of the linear and nonlinear terms resulting from the projection of the velocity governing equations into the space generated by the basis functions. It should be noted that the projection of the pressure gradient onto the basis is analytically zero which means that pressure gradient is not present in the discretized equations. This is so because of two reasons: the formulation of the velocity in terms of a scalar potential function (see Eqs. (2.9)–(2.10)) and the choice of basis functions in the expansion of the potential function in (3.8) that make boundary conditions (2.7) and (2.8) for U and W be automatically fulfilled. The nonlinear discretized equations (A.19) was solved by means of an iterative Newton method.

Appendix B

Discretization procedure of the natural convection problem

The aim of this appendix is to show the structure of the **B** and **Q** matrices in Eq. (3.29) and how we arrived to such an equation. Let us recall the expansion of the concentration,

$$C(\tau, X, Y, Z) = \sum_{i=2}^{N}\sum_{j=2}^{N}\sum_{k=1}^{N} c_{ijk}F_{ijk}(X, Y, Z) \tag{B.1}$$

with $F_{ijk}(X, Y, Z) = h_i(X)h_j(Y)h_k(Z)$ and the expansion of the velocity,

$$V = \begin{pmatrix} \mathrm{u} \\ \mathrm{v} \\ \mathrm{w} \end{pmatrix} = \sum_{p=0}^{M}\sum_{q=0}^{M}\sum_{r=0}^{M} \begin{pmatrix} u_{pqr}G_{pqr}(X, Y, Z) \\ v_{pqr}G_{pqr}(X, Y, Z) \\ w_{pqr}G_{pqr}(X, Y, Z) \end{pmatrix} \tag{B.2}$$

with $G_{pqr}(X, Y, Z) = T_p(2X)T_q(2Y)T_r(2Z)$. For the sake of clarity the three subscripts are collapsed into a single one and the basis functions in the subset $\{F_{ijk}\}_{ijk}$, $i, j = 2, ..., N$, $k = 1, ..., N$ are sorted so that those with subscript $k = 1$ are in the last positions. Thus, we have

$$C = \sum_{l=1}^{N_1} \widehat{c}_l(\tau)\widehat{F}_l(X, Y, Z) + \sum_{l=N_1+1}^{N_1+N_2} \widehat{c}_l(\tau)\widehat{F}_l(X, Y, Z) \tag{B.3}$$

and

$$V = \sum_{l=1}^{M_3} \begin{pmatrix} \widehat{u}_l\widehat{G}_l(X, Y, Z) \\ \widehat{v}_l\widehat{G}_l(X, Y, Z) \\ \widehat{w}_l\widehat{G}_l(X, Y, Z) \end{pmatrix} \tag{B.4}$$

In (B.3) $N_1 = (N-1)^3$, $N_2 = (N-1)^2$, $\widehat{F}_l$ and $\widehat{c}_l$ with $1 \leqslant l \leqslant N_1$ represent respectively functions F_{ijk} and coefficients c_{ijk} for values $2 \leqslant i, j, k \leqslant N$ and $\widehat{F}_l$ and $\widehat{c}_l$ with $N_1 + 1 \leqslant l \leqslant N_1 + N_2$ represent respectively functions F_{ij1} and coefficients a_{ij1} for values $2 \leqslant i, j \leqslant N$. In (B.4) $M_3 = (M+1)^3$ and $\widehat{u}_l$, $\widehat{v}_l$, $\widehat{w}_l$ and $\widehat{G}_l$ represent respectively u_{pqr}, v_{pqr}, w_{pqr} and G_{pqr} for values $0 \leqslant p, q, r \leqslant M$.

For the sake of simplicity the hats over the variables will be suppressed from now on. Let be $N_3 = N_1 + N_2$. Substitution of expressions (B.3) and (B.4) into Eq.(2.27) and boundary

condition (2.29) yields

$$\sum_{l=1}^{N_3}\dot{c}_l F_l = -\sum_{l=1}^{N_3} c_l\left[\frac{Sc}{Pr}Ra^{1/2}\left(\frac{\partial}{\partial X}F_l\sum_{m=0}^{M_3}u_m G_m+\frac{\partial}{\partial Y}F_l\sum_{m=0}^{M_3}v_m G_m+\frac{\partial}{\partial Z}F_l\sum_{m=0}^{M_3}w_m G_m\right)\right.$$
$$\left.-\left(\frac{\partial^2}{\partial X^2}F_l+\frac{\partial^2}{\partial Y^2}F_l+\frac{\partial^2}{\partial Z^2}F_l+\right)\right] \tag{B.5}$$

and

$$\sum_{l=1}^{N_3} c_l\left(\frac{\partial}{\partial Z}F_l(X,Y,-1/2)-\phi F_l(X,Y,-1/2)\right)=0 \tag{B.6}$$

Once (B.5) is projected onto the space generated by the subset $\{F_l\}_{l=1,...,N_1}$ and boundary condition (B.6) is projected onto the space generated by the subset $\{F_l\}_{l=N_1+1,...,N_3}$ we obtain:

$$\sum_{l=1}^{N_3}\dot{c}_l\left\langle F_l,F_n\right\rangle =$$
$$-\sum_{l=1}^{N_3} c_l\left[\frac{Sc}{Pr}Ra^{1/2}\sum_{m=0}^{M_3}\left(u_m\left\langle G_m\frac{\partial}{\partial X}F_l,F_n\right\rangle+v_m\left\langle G_m\frac{\partial}{\partial Y}F_l,F_n\right\rangle+w_m\left\langle G_m\frac{\partial}{\partial Z}F_l,F_n\right\rangle\right)\right.$$
$$\left.-\left(\left\langle\frac{\partial^2}{\partial X^2}\widehat{F}_l,\widehat{F}_n\right\rangle+\left\langle\frac{\partial^2}{\partial Y^2}F_l,F_n\right\rangle+\left\langle\frac{\partial^2}{\partial Z^2}F_l,F_n\right\rangle\right)\right] \qquad n = 1,...,N_1 \tag{B.7}$$

and

$$\sum_{l=1}^{N_3} c_l\left(\left\langle\frac{\partial}{\partial Z}F_l(X,Y,-1/2),F_n\right\rangle-\phi\left\langle F_l(X,Y,-1/2),F_n\right\rangle\right)=0 \qquad n=N_1+1,...,N_3 \tag{B.8}$$

In order to compute the inner products in Eqs. (B.7-B.8) we need to calculate integrals of the type

$$\int_{-0.5}^{0.5} h_l(Z)h_n(Z)\frac{1}{\sqrt{1-Z^2}}dZ \tag{B.9}$$

$$\int_{-0.5}^{0.5} T_m(2Z)h_l'(Z)h_n(Z)\frac{1}{\sqrt{1-Z^2}}dZ \tag{B.10}$$

$$\int_{-0.5}^{0.5} T_m(2Z)h_i(Z)h_n(Z)\frac{1}{\sqrt{1-Z^2}}dZ \tag{B.11}$$

$$\int_{-0.5}^{0.5} h_l''(Z)h_n(Z)\frac{1}{\sqrt{1-Z^2}}dZ \tag{B.12}$$

The following recurrence formulae for the derivatives of the Chebyshev polynomials were used to compute these integrals

$$T_k'(\xi)=2k\sum_{n=0}^{K'}\left(\frac{1}{\zeta_{k-1-2n}}\right)T_{k-1-2n}(\xi) \tag{B.13}$$

$$T_k''(\xi)=4k\sum_{n=0}^{K''}\left(\frac{(n+1)[k-(n+1)]}{\zeta_{k-2(n+1)}}\right)T_{k-2(n+1)}(\xi) \tag{B.14}$$

where K' and K'' are the integer part of $(k-1)/2$ and $(k-2)/2$, respectively, $\zeta_k = 1$ for $k > 0$ and $\zeta_0 = 2$. Once the inner products are calculated, (B.7) and (B.8) can be written in the matricial form

$$(\mathbf{B_1}, \mathbf{B_2}) \begin{pmatrix} \dot{\mathbf{c_1}} \\ \dot{\mathbf{c_2}} \end{pmatrix} = (\mathbf{Q_1}, \mathbf{Q_2}) \begin{pmatrix} \mathbf{c_1} \\ \mathbf{c_2} \end{pmatrix} \tag{B.15}$$

and

$$(\mathbf{R_1}, \mathbf{R_2}) \begin{pmatrix} \mathbf{c_1} \\ \mathbf{c_2} \end{pmatrix} = 0 \tag{B.16}$$

where $\mathbf{B_1}$ and $\mathbf{Q_1}$ are square matrices of dimension $N_1 \times N_1$, $\mathbf{B_2}$ and $\mathbf{Q_2}$ are rectangular matrices of dimension $N_1 \times N_2$, $\mathbf{R_1}$ is a rectangular matrix of dimension $N_2 \times N_1$, $\mathbf{R_2}$ is a square matrix of dimension $N_2 \times N_2$, $\mathbf{c_1}$ is a vector of dimension N_1 and $\mathbf{c_2}$ is a vector of dimension N_2. From Eq. (B.16) we have

$$\begin{aligned} \mathbf{c_2} &= -\mathbf{R_2}^{-1}\mathbf{R_1}\mathbf{c_1} \\ \dot{\mathbf{c_2}} &= -\mathbf{R_1}^{-1}\mathbf{R_1}\dot{\mathbf{c_1}} \end{aligned} \tag{B.17}$$

which replaced in Eq.(B.15) gives,

$$(\mathbf{B_1} - \mathbf{B_2}\mathbf{R_2}^{-1}\mathbf{R_1})\dot{\mathbf{c_1}} = (\mathbf{Q_1} - \mathbf{Q_2}\mathbf{R_2}^{-1}\mathbf{R_1})\mathbf{c_1} \tag{B.18}$$

which can be rewritten as

$$\mathbf{B}\dot{\mathbf{c_1}} = \mathbf{Q}\mathbf{c_1} \tag{B.19}$$

where $\mathbf{B}$ and $\mathbf{Q}$ are $N_1 \times N_1$ square matrices. Once the ordinary differential equations (B.19) are numerically solved $\mathbf{c_2}$ is obtained from Eq. (B.17).

Bibliography

[1] F. Camacho-Rubio, E. J. Alameda, P. González-Tello, and G. L. González, "A comparative study of the activity of freen and immobilized enzymes and its application to glucose isomerase," *Chem. Eng. Sci.*, vol. 51, no. 17, pp. 4159–4165, 1996.

[2] A. Al-Muftah and M. Abu-Reesh, "Effects of simultaneous internal and external mass transfer and product inhibition on immobilized enzyme-catalyzed reactor," *Biochem. Eng. J.*, vol. 27, pp. 167–178, 2005.

[3] M. Hornung, M. Ludwig, A. M. Gerrard, and H. P. Schmauder, "Optimizing the production of bacterial cellulose in surface culture: Evaluation of substrate mass transfer influences on the bioreaction (part 1)," *Eng. Life Sci.*, vol. 6, pp. 537–545, 2006.

[4] D. I. Enache, W. Thiam, D. Dumas, S. Ellwood, G. J. Hutchings, S. H. Taylor, S. Hawker, and E. H. Stitt, "Intensification of the solvent–free catalytic hydroformylation of cyclododecatriene: Comparison of a stirred batch reactor and a heat–exchange reactor," *Catal. Today*, vol. 128, pp. 18–25, 2007.

[5] J. Bailey and D. E. Ollis, *Biochemical engineering fundamentals*. New York: McGraw-Hill, second ed., 1986.

[6] M. Shuler and F. Kargi, *Bioprocess engineering:Basic Concepts*. Englewood Cliffs, New Jersey: Prentice Hall, second ed., 1991.

[7] P. Jüsten, G. Paul, A. Nienow, and C. Thomas, "Dependence of *Penicillium chrysogenum* growth, morphology, vacuolation, and productivity in fed-batch fermentations on impeller type and agitation intensity," *Biothechnol. Bioeng*, vol. 59, pp. 762–775, 1998.

[8] J. S. Perez, E. R. Porcel, J. C. Lopez, J. F. Sevilla, and Y. Chisti, "Shear rate in stirred tank and bubble column bioreactors," *Chem. Eng. J.*, vol. 124, pp. 1–5, 2006.

[9] Y. Han, J.-J. Wang, X.-P. Gu, and L.-F. Feng, "Numerical simulation on micromixing of viscous fluids in a stirred-tank reactor," *Chem. Eng. Sci.*, vol. 74, pp. 9–17, 2012.

[10] P. Yu, T. Lee, Y. Zeng, and H. Low, "Effect of vortex breakdown on mass transfer in a cell culture bioreactor," *Mod. Phys. Lett. B*, vol. 19, pp. 1543–1546, 2005.

[11] Y. Zeng, T. Lee, P. Yu, and H. Low, "Numerical study of mass transfer coefficient in a 3d flat-plate rectangular microchannel bioreactor," *Int. Commun. Heat Mass*, vol. 34, pp. 217–224, 2007.

[12] M. Al-Shannag, A. Al-Qodah, J. Herrero, J. Humphrey, and F. Giralt, "Using a wall-driven flow to reduce the external mass-transfer resistance of a bio-reaction system," *Biochem. Eng. J.*, vol. 39, pp. 554–565, 2008.

[13] M. Al-Shannag, "Mass transport enhancement in annular–shaped lid–driven bioreactor," *Bioproc. Biosyst. Eng.*, vol. 35, no. 6, pp. 875–884, 2012.

[14] J. A. C. Humphrey, J. Cushner, M. Al-Shannag, J. Herrero, and F. Giralt, "Shear–driven flow in a toroid of square cross section," *J. Fluid Eng-T ASME*, vol. 125, pp. 130–137, 2003.

[15] Y. D. Spasov, J. Herrero, F. X. Grau, and F. Giralt, "Linear stability analysis and numerical calculations of the lid–driven flow in a toroidally shaped cavity," *Phys. Fluids*, vol. 15, pp. 134–146, 2003.

[16] H.-H. Cheng and C.-S. Tan, "Carbon dioxide capture by blended alkanolamines in rotating packed bed," *Energy Procedia*, vol. 1, pp. 925–932, 2009.

[17] W.-D. Sung and Y.-S. Chen, "Characteristics fo a rotating packed bed equipped with blade packings and baffles," *Sep. Purif. Technol.*, vol. 93, pp. 52–28, 2012.

[18] L.-J. Hsu and C.-C. Lin, "Removal of methanol and 1-butanol from binary mixtures by absorption in rotating packed beds with blade packings," *Chem. Eng. J.*, vol. 168, pp. 190–200, 2011.

[19] G. Peev, A. Nikolova, and D. Peshev, "Solid dissolution in a thin liquid film on a horizontal rotating disk," *Heat Mass transfer*, vol. 43, pp. 397–403, 2007.

[20] D. Peshev, G. Peev, and A. Nikolova, "Dissolution in film flow of shear thinnging liquid on a horizontal rotating disk," *Chem. Eng. Process.*, vol. 49, pp. 616–621, 2010.

[21] I. Tsibranska, D. Peshev, G. Peev, and A. Nikolova, "Modelling of mass transfer in film flow of shear thinning liquid on a horizontal rotating disk," *Chem. Eng. Process*, vol. 48, pp. 823–827, 2009.

[22] C. Torras, J. Pallares, R. Garcia-Valls, and M. Jaffrin, "Numerical simulation of the flow in a rotating disk filtration module," *Desalination*, vol. 235, pp. 122–138, 2009.

[23] C. Hardacre, E. A. Mullan, D. W. Rooney, J. M. Thompson, and G. S. Yablonsky, "Comparison of mass transfer effects in the heterogeneously catalysed hydrogenation of phenyl acetylene in heptane and an ionic liquid," *Chem. Eng. Sci.*, vol. 61, pp. 6995–7006, 2006.

[24] L. A. Belfiore, "Dynamic shear in continuous–flow rotating–disk catalytic reactors with stress-sensitive kinetics based on curie's theorem in non–equilibrium thermodynamics," *Chem. Eng. Sci.*, vol. 65, pp. 680–691, 2010.

[25] M. Meeuwse, S. Lempers, J. van Schaaf, and J. Schouten, "Liquid–solid mass transfer and reaction in a rotor–stator spinning disc reactor," *Ind. Eng. Chem. Res.*, vol. 49, pp. 10751–10757, 2010.

[26] S. Abrahamson, J. Eaton, and D. Koga, "The flow between shrouded corotating disks," *Phys. Fluids A-Fluid*, vol. 1, no. 2, pp. 241–251, 1989.

[27] J. Humphrey, C. Schuler, and I. Iglesias, "Analysis of viscous dissipation in disk storage-systems and similar flow configurations," *Phys. Fluids A-Fluid*, vol. 4, no. 7, pp. 1415–1427, 1992.

[28] V. Radel and A. Szeri, "Symmetry breaking bifurcation in finite disk flow," *Phys. Fluids*, vol. 9, no. 6, pp. 1650–1656, 1997.

[29] I. Iglesias and J. Humphrey, "Two- and three-dimensional laminar flows between disks co-rotating in a fixed cylindrical enclosure," *Int J Numer Meth Eng*, vol. 26, pp. 581–603, MAR 15 1998.

[30] J. Herrero, F. Giralt, and J. A. C. Humphrey, "Influence of the geometry on the structure of the flow between a pair of corotating disks," *Phys. Fluids*, vol. 11, pp. 88–96, 1999.

[31] J. Herrero, F. Giralt, and J. A. C. Humphrey, "Non-isothermal laminar flow and heat transfer between disks corotating in a fixed enclosure," *Int. J. Heat Mass Tran*, vol. 42, pp. 3291–3306, 1999.

[32] A. Randriamampianina, R. Schieste, and M. Wilson, "Spatio-temporal behaviour in an enclosed corotating disk pair," *J. Fluid Mech.*, vol. 434, pp. 39–64, 2001.

[33] R. Fukaya, S. Obi, S. Masuda, and M. Tokuyama, "Flow instability and elastic vibration of shrouded corotating disk systems," *Experiments in Fluids*, vol. 33, pp. 369–373, SEP 2002.

[34] M. Al-Shannag, J. Herrero, J. Humphrey, and F. Giralt, "Effect of radial clearance on the flow between corotating disks in fixed cylindrical enclosures," *Journal of Fluids Engineering-Transactions of the Asme*, vol. 124, pp. 719–727, SEP 2002.

[35] J. Humphrey, M. Kazemi, and J. Herrero, "Method for calculating the velocity of air flowing past a pair of suspensions in a disk drive," *Microsystem Technologies-Micro-and Nanosystems-Information Storage and Processing Systems*, vol. 9, pp. 534–540, OCT 2003.

[36] H. Cho, C. Won, G. Ryu, and D. Rhee, "Local heat transfer characteristics in a single rotating disk and co-rotating disks," *Microsyst Technol*, vol. 9, pp. 399–408, SEP 2003.

[37] A. Randriamampianina, R. Schiestel, and M. Wilson, "The turbulent flow in an enclosed corotating disk pair: axisymmetric numerical simulation and reynolds stress modelling," *International Journal of Heat and Fluid Flow*, vol. 25, no. 6, pp. 897–914, 2004.

[38] T. Miura and J. Mizushima, "Transitions of axisymmetric flow between two corotating disks in an enclosure," *Fluid Dyn. Res.*, vol. 39, pp. 193–208, JAN 2007.

[39] S. Kanagai, J. Suzuki, S. Obi, and S. Masuda, "Flow instability and disk vibration of shrouded corotating disk system," *Journal of Fluids Engineering-Transactions of the Asme*, vol. 129, no. 10, pp. 1306–1313, 2007.

[40] J. Mizushima, G. Sugihara, and T. Miura, "Two modes of oscillatory instability in the flow between a pair of corotating disks," *Phys. Fluids*, vol. 21, pp. 014101–1–15, 2009.

[41] T. Engin, M. Özdemir, and S. Cesmeci, "Design, testing and two-dimensional flow modeling of a multiple-disk fan," *Exp. Therm. Fluid. Sci.*, vol. 33, pp. 1180–1187, 2009.

[42] S. Sarkar, D. Roy, and J. Mukherjee, "Production of a potentially novel antimicrobial compound by a biofilm–forming marine *Streptomyces* sp. in a niche-mimic rotating disk bioreactor," *Bioprocess Biosyst Eng.*, vol. 33, pp. 207–217, 2010.

[43] C. Drumm, S. Tiwari, J. Kuhnert, and H.-J. Bart, "Finite pointset method for simulation of the liquid–liquid flow field in an extractor," *Comput. Chem. Eng.*, vol. 32, pp. 2946–2957, 2008.

[44] C. Drumm, M. M. Attarakih, and H.-J. Bart, "Coupling of cfd with dpbm for an rdc extractor," *Chem. Eng. Sci.*, vol. 64, pp. 721–732, 2009.

[45] C. T. Gonzalez-Hidalgo, J. Herrero, and D. Puigjaner, "Enhancement of mixing in a catalytic chemical reactor consisting of a stack of corotating disks in a cylindrical enclosure," *Submitted*.

[46] C. T. Gonzalez-Hidalgo, J. Herrero, and D. Puigjaner, "Mixing intensification by natural convection with application to a chemical reactor design," *Chem. Eng. J.*, vol. 200, pp. 506–520, 2012.

[47] E. Bodenschatz, W. Pesch, and G. Ahlers, "Recent developments in Rayleigh–Bénard convection," *Annu. Rev. Fluid Mech.*, vol. 32, pp. 709–778, 2000.

[48] A. V. Getling, *Rayleigh–Bénard convection: structures and dynamics*, vol. 11 of *Advanced Series in Nonlinear Dynamics*. World Scientific Publishing, 1998.

[49] L. de la Cruz and E. Ramos, "Mixing with time dependent natural convection," *Int. Commun. Heat Mass*, vol. 33, pp. 191–198, 2006.

[50] A. Gelfgat, A. Yarin, and P. Bar-Yoseph, "Convection-induced enhancement of mass transfer through an interface separating two immiscible liquids in a two-layer horizontal annulus," *Phys. Fluids*, vol. 15, pp. 790–800, 2003.

[51] D. Ma, D. Henry, and H. B. Hadid, "Three–dimensional numerical study of natural convection in vertical cylinders partially heated from the side," *Phys. Fluids*, vol. 17, p. 124101, 2005.

[52] A. N. Campbell, S. S. S. Cardoso, and A. N. Hayhurst, "A scaling analysis of the effects of natural convection, when sal'nikov's reaction: $p- > a- > b$ occurs, together with diffusion and heat transfer in a batch reactor," *Chem. Eng. Res. Des.*, vol. 84, pp. 553–561, 2006.

[53] A. N. Campbell, S. S. S. Cardoso, and A. N. Hayhurst, "A comparison of measured temperatures with those calculated numerically and analytically for an exothermic chemical reaction inside a spherical batch reactor with natural convection," *Chem. Eng. Sci.*, vol. 62, pp. 3068–3082, 2007.

[54] D. Puigjaner, J. Herrero, F. Giralt, and C. Simó, "Stability analysis of the flow in a cubical cavity heated from below," *Phys. Fluids*, vol. 16, pp. 3639–3655, 2004.

[55] D. Puigjaner, J. Herrero, F. Giralt, and C. Simó, "Bifurcation analysis of multiple steady flow patterns for Rayleigh–Bénard convection in a cubical cavity at $Pr = 130$," *Phys. Rev. E*, vol. 73, p. 046304, 2006.

[56] D. Puigjaner, J. Herrero, C. Simó, and F. Giralt, "Bifurcation analysis of steady Rayleigh–Bénard convection in a cubical cavity with conducting sidewalls," *J. Fluid Mech.*, vol. 598, pp. 393–427, 2008.

[57] C. Simó, D. Puigjaner, J. Herrero, and F. Giralt, "Dynamics of particle trajectories in a rayleigh–bénard problem," *Commun. Nonlinear Sci.*, vol. 15, pp. 25–39, 2010.

[58] C. Canuto, M. Y. Hussaini, A. Quarteroni, and T. A. Zang, *Spectral Methods. Fundamentals in Single Domains*. Scientific Computation, Berlin: Springer–Verlag, 2006.

[59] P. R, *Spectral Methods for Incompressible Viscous Flow*. New York: Springer, 2002.

[60] G. Karniadakis and S. J. Sherwin, *Spectral/hp Element Methods for CFD*. New York: Oxford University Press, second ed., 1999.

[61] J. P. Boyd, *Chebyshev and Fourier Spectral Methods*. Mineola, New York: Dover Publications, 2001.

[62] J. C. Butcher, *Numerical methods for ordinary differential equations*. New York: John Wiley & Sons, 2003.

[63] D. Kincaid and W. Cheney, *Numerical Analysis*. Pacific Grove, California: Brooks/Cole Publishing Company, 1991.

[64] J. M. Lopez and J. Shen, "An efficient spectral–projection method for the Navier–Stokes equations in cylindrical geometries. I. Axisymmetric cases," *J. Comput. Phys.*, vol. 139, pp. 308–326, 1998.

[65] J. M. Lopez, F. Marques, and J. Shen, "Complex dynamics in a short annular container with rotating bottom and inner cylinder," *J. Fluid Mech.*, vol. 501, pp. 327–354, 2004.

[66] J. Dongarra, J. D. Croz, S. Hammarling, and R. J. Hanson, "An extended set of FORTRAN Basic Linear Algebra Subroutines," *ACM T. Math. Software*, vol. 14, pp. 1–17, 1988.

[67] J. Dongarra, J. D. Croz, I. Duff, and S. Hammarling, "A set of Level 3 Basic Linear Algebra Subprograms," *ACM T. Math. Software*, vol. 16, pp. 1–17, 1990.

[68] C. A. J. Fletcher, *Computational Techniques for Fluid Dynamics, vols 1 and 2*. Berlin: Springer, 1988.

[69] C. Canuto, M. Y. Hussaini, and A. Quarteroni, *Spectral Methods in Fluid Dynamics*. Springer Series in Computational Physics, New York: Springer Verlag, 1987.

[70] J. Mizushima and T. Nakamura, "Onset of three–dimensional thermal convection in a rectangular parallelepiped cavity," *J. Phys. Soc. Jpn*, vol. 72, pp. 197–200, 2003.

[71] C. Simó, D. Puigjaner, J. Herrero, and F. Giralt, "Dynamics of particle trajectories in a Rayleigh–Bénard problem," *Commun. Nonlinear Sci. Numer. Simulat.*, vol. 15, pp. 24–39, 2010.

[72] J. M. Ottino, *The kinematics of mixing: stretching, chaos and transport*. Cambridge: Cambridge University Press, 1989.

[73] J. M. Ottino, "Mixing, chaotic advection and turbulence," *Annu. Rev. Fluid Mech.*, vol. 22, pp. 207–253, 1990.

[74] R. Seydel, *Practical Bifurcations and Stabilty Analysis: from Equilibrium to Chaos*. New York: Springer–Verlag, second ed., 1994.

[75] M. Mikhailov and M. Özisik, *Unified Analysis and Solutions of Heat and Mass Diffusion*. Mineola: Dover Publications, Inc., 1994.

[76] C. A. Schuler, W. Usry, B. Weber, J. A. C. Humphrey, and R. Greif, "On the flow in the unobstructed space between shrouded corotating disks," *Phys. Fluids A-Fluid*, vol. 2, pp. 3291–3306, 1990.

[77] R. B. Bird, W. E. Stewart, and E. N. Lightfoot, *Transport Phenomena*. New York: John Wiley & Sons, second ed., 2002.

[78] D. Puigjaner, J. Herrero, C. Simó, and F. Giralt, "From steady solutions to chaotic flows in a Rayleigh–Bénard problem at moderate Rayleigh numbers," *Physica D*, vol. 240, pp. 920–934, 2011.

[79] J. Jeong and F. Hussain, "On the identification of a vortex," *J. Fluid Mech.*, vol. 285, pp. 69–94, 1995.

[80] S. Grossmann and D. Lohse, "Thermal convection for large Prandtl numbers," *Phys. Rev. Lett.*, vol. 86, pp. 3316–3319, 2001.

[81] S. Grossmann and D. Lohse, "Prandtl and Rayleigh number dependence of the Reynolds number in turbulent thermal convection," *Phys. Rev. E*, vol. 66, p. 016305, 2002.

[82] R. B. Bird, W. E. Stewart, and E. N. Lightfoot, *Transport Phenomena*. New York: John Wiley & Sons, second ed., 2002.

[83] M. Tabor, *Chaos and Integrability in Nonlinear Dynamics: An Introduction*. New York: Wiley–Interscience, 1989.

[84] S. R. Wickramasinghe, J. D. Garcia, and B. Han, "Mass and momentum transfer in hollow fibre blood oxygenators," *J. Membr. Sci.*, vol. 208, pp. 246–256, 2002.